INSTITUTO DE FÍSICA
Universidade Federal Fluminense

Gabriel Soares Rocha

Monte Carlo Simulations of Center Vortex Effective Models

Niterói

10 de junho de 2019

Gabriel Soares Rocha

Monte Carlo Simulations of Center Vortex Effective Models

Universidade Federal Fluminense – UFF

Programa de Pós-Graduação em Física

Supervisor: Luis Esteban Oxman

Niterói

10 de junho de 2019

Ficha catalográfica automática - SDC/BIF
Gerada com informações fornecidas pelo autor

R672m Rocha, Gabriel Soares
Monte Carlo Simulations of Center Vortex Effective Models / Gabriel Soares Rocha ; Luis Esteban Oxman, orientador. Niterói, 2019.
122 p. : il.

Dissertação (mestrado)-Universidade Federal Fluminense, Niterói, 2019.

DOI: http://dx.doi.org/10.22409/PPGF.2019.m.16480289773

1. Confinamento (Física). 2. Simulação Numérica. 3. Produção intelectual. I. Oxman, Luis Esteban, orientador. II. Universidade Federal Fluminense. Instituto de Física. III. Título.

CDD -

Bibliotecário responsável: Mario Henrique de Oliveira Castro - CRB7/6155

Gabriel Soares Rocha

Monte Carlo Simulations of Center Vortex Effective Models

Trabalho aprovado. Niterói, 10 de junho de 2019:

Dr. Luis Esteban Oxman
Orientador

Dr. Daniel Gustavo Barci
Convidado 1

Dr. Rodrigo Ferreira Sobreiro
Convidado 2

Niterói
10 de junho de 2019

Este trabalho é dedicado às mães como a minha, que aturam filhos avoados que passam seus dias enfurnados na frente do computador, lendo ou escrevendo textos estranhos.

Acknowledgements

Como esperado, primeiramente agradeço à minha mãe, Maria José, e ao meu pai, Luiz, pelo apoio incondicional bem como aos familiares que me apoiam neste início de jornada acadêmica. Foram essenciais à esse trabalho o prof. Oxman, que sempre foi paciente e solícito, mesmo com minhas dúvidas tardias e minha impaciência além de Gustavo Simões e David Rosa que prestaram muitas 'consultorias' nos meus programas.

Agradeço aos meus amigos Douglas Montes, Hadassa Moraes, Filipe Melo, Lucas Lima, Marcos Benício, que também me ajudou como 'consultor', Miguel Gallo, Maron Anka, Arthur Vieira e Bernardo França cujas presenças tornaram minha trajetória até aqui mais agradável e aos amigos de mais longa data, Marllon Valentim, Cristiano Vaz, Beatriz Malheiros, Arthur Duarte, Adso Rangel, Miguel Ribeiro e Kayalla Pontes, que confiam mais em mim do que eu mesmo.

A Nelson Lachini, Beatriz Malheiros e aos Profs. Gabriel Denicol, Rodrigo Sobreiro e Marco Moriconi devo agradecimentos pela ajuda com oportunidades de doutorado e aos três últimos por cartas de recomendação. "A universidade funciona para os alunos", dita pelo último, é uma frase que levarei comigo. Agradeço ao prof. Marcelo Sarandy que foi essencial à minha transição para a pós-graduação, indo além do seu papel de coordenador da pós-graduação, assim como à profa. Beatriz Ponciano, que teve papel muitíssimo importante na minha graduação e que, por alguma desatenção minha ficou fora dos agradecimentos da monografia, me desculpe; e ao prof. Nuno Crokidakis que também atuou como 'consultor'.

Sou grato também à Coordenação de Aperfeiçoamento de Pessoal de Nível Superior (CAPES) pelo financiamento durante o mestrado e à Sociedade Brasileira de Física (SBF) por ter reconhecido meu trabalho no XXXIX Encontro Nacional de Física de Partículas e Campos. Por fim, agradeço a todos os foristas de internet que me ajudaram em etapas de debugagem dos programas e na elaboração do presente texto e a todos que trabalham para a universalização de conteúdo verdadeiramente científico numa internet assombrada pelos demônios do culto à ignorância e à intolerância.

[...] in the very middle of the room, an enormous glass tank of deep green liquid, big enough for all of them to swim in; a number of pearly-white objects were drifting around lazily in it.[...] 'They're brains.' 'Brains?' 'Yes . . . I wonder what they're doing with them?' - J. K. Rowling in *Harry Potter and the Order of the Phoenix*

L'$|\Psi\rangle$ *c'est moi* - Louis XIV

Abstract

In this work we analyze the effective model obtained in ref. [58] via Monte Carlo techniques. In that reference, the authors consider an ensemble of closed line-like objects that obey an action that has length, curvature and contact interaction terms. After a number of controlled approximations and putting the model on a lattice, they translated averages of this confinement order parameter into the ratio between the partition function of a frustrated XY-model and its unfrustrated counterpart. Here, we shall numerically analyze different possibilities for the frustration distribution: one localized at the links that pierce the Wilson loop minimal area and one that relies on the solid angle picture, that explores the multivaluedness of this quantity as one goes around the Wilson loop. In particular, we perform averages near the critical temperature as the continuum limit is reproduced when the system is near that point. Two results of ref. [58] were reproduced numerically: the area law near the critical temperature and the expected dependence of the string tension on the representation of the gauge group. It is also found that the N-ality 1 representations obey the constant ratio $\sigma_A^N(1)/\sin^2\frac{\pi}{N} \approx 2.038\ 10^{-4}$ for a 11^3 lattice and evidence that an area law arises from the solid angle picture.

Keywords: XY-model, numerical simulation, confinement(physics).

List of Figures

List of Tables

Contents

Introduction

One of the most important and still unsolved [43] problems in contemporary Physics is to sistematically understand the inner workings of the confinement of quarks and gluons from Quantum Chromodynamics [60, 74], the proposed theory to model the internal structure of hadrons. In the last decades, many theoretical efforts have been made in this sense, ranging from analytical [13, 23, 50] to numerical ones [9, 20, 36], hence building a certain image of how these interactions might look like. One hopes that in the next few years, experiments like the GlueX collaboration [1] at the Jefferson Lab, give a nature's veredict about them.

An illustrative way to introduce this theme is to consider how a massive static quark-antiquark pair interact. When these sources are close to each other, the chromoelectric field lines are squeezed, in such a way that the energy stored in this field grows linearly with the interquark separation, thus generating the so-called *flux tube*. This occurs in contrast to the usual electromagnetism, in which the field would spread further into space.

This idea is indeed confirmed by lattice QCD [15, 70], a formalism onto which the properties of this theory are analyzed in a discretized spacetime with Monte Carlo techniques. In this context it is possible to obtain information about the low energy sector of QCD, which is until now prohibitively difficult in the continuum. Further accounts on the theme are discussed in Appendix A. In fig. 1 one may see a recent numerical result from ref. [7].

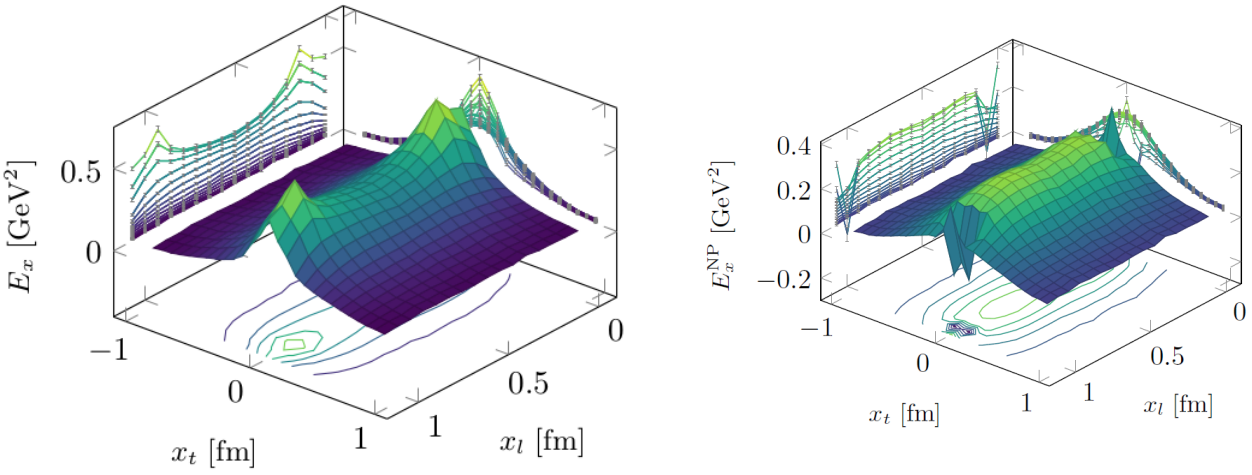

Figure 1 – Chromoelectric field configuration of a massive quark-antiquark pair as a function of the longitudinal and transversal with respect to the line that separates the two particles. The right plot can be obtained from the left one by removing the Coulomb potential contribution. Taken from ref. [7].

[1] http://www.gluex.org/GlueX/Home.html

One hence sees that, by removing the Coulomb contribution to the potential, there is a region along the line between the pair at which the chromoelectric field is constant, which is equivalent to the squeezing of field lines. However, as the charges are further separated, and the effect of dynamical quarks are considered (they were not in ref. [7]) it becomes energetically favorable that these dynamical particles appear from vacuum to screen the original pair, *breaking the string* and yielding two colorless states.

One way to give a more physical picture to these structures is to consider an ingenious analogy with the usual electromagnetism: *dual superconductivity*. This is based on what would occur with a magnetic monopole-antimonopole pair if these are put in a type II superconductor. These superconductors have the property that, with suficiently large magnetic fields, it is possible to produce Abrikosov vortices [2]. These are filaments where the magnetic field penetrates the material. Thus a flux tube is formed, something that does not happen in a type I superconductor due to the London currents that appear in its surface [6].

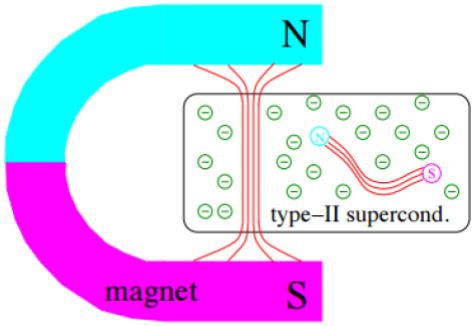

Figure 2 – Pictorial representation of a Abrikosov vortex and the hypothetical monopole confinement in a type II superconductor. Taken from ref. [63].

Therefore, if monopoles existed, they were put in a type II superconductor, and had the right magnetic charge, a magnetic monopole-antimonopole pair would produce a flux tube between them. Thus a linearly growing potential would be generated, hence confining the pair. In this QCD vacuum picture, originally proposed by Nambu [56], the role of the magnetic field is made by the chromoelectric field, thus characterizing the *duality*.

However, the linearly growing potential is not the whole story. By taking into account the quantum fluctuations in this string-like structure, a Coulomb-like term arises. According to the pioneering work of ref. [51], one gets to the fact that the effective potential between the sources is

$$V(r) = \sigma r + \frac{\gamma}{r} + O\left(\frac{1}{r^2}\right), \qquad \gamma = -\frac{\pi}{24}(d-2) \tag{1}$$

where d is the spacetime dimension; σ is the so-called string tension and r is the pair separation. The term proportional to $1/r$ is called the Lüscher term. This result is also

confirmed by lattice simulations [7, 9].

Complementing the dual superconductor picture, the mechanism that engenders the regular superconductivity is the condensation of pairs of highly correlated electric charge pairs (electrons forming Cooper pairs), hence one is lead to think, taking duality into account, that some chromomagnetic degrees of freedom condense.

Indeed, in the context of compact QED [2] in $(2+1)D$ confinement is yielded by monopoles [39, 61]. As QCD has a more complicated, non-abelian gauge symmetry, one might be lead to postulate that analogous degrees of freedom contribute to quark confinement. Nevertheless, due to the rich structure brought by this non-abelianicity, it would be reductionist to think that this analogy suffices.

In this way, a confinement picture involving what is called *center vortex* is put forward in the 70's. These configurations have an intricate definition, which depends on its effect on the gauge-invariant observable known as the Wilson loop. The latter is defined by

$$\mathcal{W} = \frac{1}{N}\mathrm{tr}P\exp\left(ig\oint_{\mathcal{C}} dx_\mu A_\mu(x)\right), \tag{2}$$

where $\mathcal{C}$ is a closed path in four dimensions.

Briefly, the Wilson loop is a confinement order parameter, exhibiting thence different behaviors according to the phase of the theory. When taking averages in field configurations, the behavior of $\langle\mathcal{W}(\mathcal{C})\rangle$ is [37]

$$\langle\mathcal{W}(\mathcal{C})\rangle \sim \begin{cases} \exp\left[-\sigma A(\mathcal{S}(\mathcal{C}))\right], & \text{in the confined phase} \\ \exp\left[-\kappa\mathcal{P}(\mathcal{C})\right], & \text{in the deconfined phase} \end{cases} \tag{3}$$

where $A(\mathcal{S}(\mathcal{C}))$ is the area of the minimal surface whose boundary is $\mathcal{C}$ and $\mathcal{P}(\mathcal{C})$ is the perimeter of $\mathcal{C}$. With this, one refers to the behavior of Wilson loop averages as having an *area law* and *perimeter law*, respectively. This quantity will have a section to itself later.

Now, it will be defined what is meant by the *center* of a group G. This is the set of elements that comute with all other group members, namely,

$$Z := \{z \in G \mid zg = gz, \forall g \in G\}. \tag{4}$$

In the case of $SU(N)$, its center consists of the N-th roots of unity,

$$Z(N) = e^{i\frac{2\pi}{N}k}\mathbb{1} \quad k = 0, ..., N-1. \tag{5}$$

Accordingly, a configuration A_μ, localized on a curve ℓ is called a *center vortex* if the Wilson loop computed over $\mathcal{C}$ receives a contribution of a non-trivial center element

[2] It consists of a discretized, but still gauge invariant, version of QED. The gauge invariance imposition leads to a formalism where the fields belong conventionally to the interval $[-\pi, \pi]$, whose compacity names the formalism. In the confined phase, monopoles form a plasma, but, in the deconfined one, they form a dilute gas of magnetic monopoles [39, 61].

when $\mathcal{C}$ is linked by ℓ, thus,

$$\mathcal{W}(\mathcal{C},\ell) = z^{L(\mathcal{C},\ell)} \text{ with } z \in Z(N) \text{ and} \tag{6}$$

$$L(\mathcal{W},\ell) = \frac{1}{4\pi}\oint_{\mathcal{C}}\oint_{\ell} d\vec{l}_{\mathcal{C}}\cdot\left(d\vec{l}_{\ell}\wedge\frac{\vec{x}_{\mathcal{C}}-\vec{x}_{\ell}}{|\vec{x}_{\mathcal{C}}-\vec{x}_{\ell}|^3}\right), \tag{7}$$

the latter being the topological invariant called *linking number* [3].

A possible way to motivate this definition is to follow the lines of ref. [13], where the quantum phenomenon of gluon mass generation is discussed using an $SU(N)$ infrared-effective gauge invariant massive lagrangian. In $d = 3$ Euclidean spacetime dimensions an explicit center-vortex soliton solution to the equations of motion is

$$A_i(x;j) = 2\pi Q_j \epsilon_{iab}\partial_a \oint_{\ell} dy_b[\Delta_0(x-y) - \Delta_m(x-y)]. \tag{8}$$

Here, $\Delta_m(x-y)$ is the mass m free propagator and the Q matrices are in Cartan subalgebra [14]. Assuming further that the typical lengths of both $\mathcal{C}$ and ℓ are large compaired to $1/m$, one obtains from (2) that the behavior of the Wilson loop is

$$\mathcal{W}(\mathcal{C}) = \exp\left(\frac{2\pi}{N} i \oint_{\mathcal{C}} dx_a \oint_{\ell} dy_b\ \epsilon_{abc}\partial_c \Delta_0(x-y)\right) \tag{9}$$

where the integral in the exponent is equivalent to the Gauss linking number up to a constant factor, because $\Delta_0(x-y) = 1/|x-y|$. Although this idea was developed in a specific dimension, this principle can be extended to higher dimensions [63]. In D dimensions, center vortices are $D-2$ hypersurfaces.

Outline of the Dissertation

The division of present work is so that, in the first chapter, a more concrete physical discussion about the Wilson loop is made, and it is shown that it probes the potential between static quarks [32]. Then, a few remarks are made about how one can get an area law from Wilson Loop averages in the strong coupling limit. After that, it is discussed that center symmetry is the one that is broken in the deconfined phase of a gauge theory [37]. Then, some lattice QCD results are presented to evidence that center vortices are indeed relevant when considering confinement properties [63]. The maximal center gauge and the center projection procedure, used to detect center vortices in lattice simulations, are briefly discussed and some numerical results are shown.

In chapter 2, the confining force and center vortex properties are further analyzed. First, the main results regarding the representation dependence of the string tension are outlined [37]. Later, it is argued that center vortices can be accounted for in QCD vacuum

[3] The fact that center vortices are localized in closed surfaces is originated from the fact that the field configurations must obey the Bianchi identity $\epsilon_{\mu\nu\lambda\rho}\partial_\nu F_{\lambda\rho} = 0$, unless there are monopoles which change the direction of the chromomagnetic flux.

if one considers an effective action that has tension and stiffness terms [28], and that a picture of confinement/deconfinement phases can be made in terms of the percolation transition of such objects. Then, Vortices are found to interact by the analysis of their correlations [25]. Closing the chapter, the branching property of these magnetic degrees of freedom is described [27].

In chapter 3, we review the steps of ref. [58] to obtain a frustrated XY model from an ensemble of closed line-like objects that have some of the properties outlined for center vortices. That is done by using a path integral identities and polymer techniques.With that they obtain a complex field theory with $U(1)$ symmetry breaking.

Analyzing the soft modes of this theory and putting the model on a lattice, they derive a frustrated XY-model. The frustration is localized in those links that pierce the Wilson loop minimal area. Averages of this confinement order parameter are translated into the ratio between the partition function of the frustrated model and its unfrustrated counterpart. Afterwards, the continuum limit and its relation with the critical coupling are discussed. Later, the Wilson loop behavior is obtained in the small and near-critical coupling regimes. They also derive a representation dependence of the string tension. After that, the solid angle picture is introduced and it is explained how its multivaluedness is exploited to capture the essential features of the near-critical region of the XY model, and how it "dilutes" the frustration.

In chapter 4 the Monte Carlo techniques used are outlined. Starting with the traditional Metropolis algorithm, that enables one to perform thermal averages with Bolzmann distribution. Then, a definition of equilibrium is presented in terms of a relaxation time and the problem of critical slowing down is briefly discussed. Following that, a method to obtain the critical coupling, the Fourth Order Cumulant Method, is described succintly. Then the Overlap Method. used to estimate the partition function ratios (henceforth interchangeably called "Wilson loop") is shown. The main source to this chapter is ref. [11].

The chapter 5 shows the numerical results obtained. One starts with a preliminary analysis of the relaxation time and of the similarity between the frustrated and the unfrustrated XY models near the critical temperature. Then one proceeds with the Wilson loop computations in the "concentrated" frustration picture, also starting with a relaxation time analysis. Then the area law and its temperature behavior are analyzed. Afterwards the representation dependence of the string tension derived in chapter two is put to scrutiny. Then, the solid angle picture simulations are outlined. Then some remarks are made about the issues present in the simulations. After that, the concluding chapter adds a few more remarks about the work and the main text ends.

There are three appendices to the present dissertation. Appendix A, based on ref. [32], arises because of the importance of lattice QCD to the current knowledge about

confinement and, in particular, about Center Vortices. There, the most famous lattice action, the Wilson one, is described. Then, the Euclidean correlators, that are of utmost importance to lattice QCD studies are described. After that, the invariant integral measure in $SU(3)$ is defined in a not-so-mathematically rigorous manner, followed by some examples.

Appendix B gives a brief account about the two main (pseudo)random number generators used in the present work. Namely, the Linear Congruential Generator, a well distributed, but short period generator, and the Mersenne Twister that has been widely used because of its ultra-astronomical period and its good "pseudo-randomness". But that comes by the cost of a cumbersome implementation, and a even more intricate motivation [53]. The main sources to this Appendix are refs. [45, 46].

Finally, in Appendix C, the precise meaning of the solid angle subtended by a square is outlined, following closely the lines of ref. [52]. First, the observer-centered solid angle is obtained, then the general case is derived by using reflexion properties and the problem is divided in four classes of points, depending on the localization of such point relative to the square.

1 Wilson loops, center vortices and confinement

In this chapter, the physical content of the Wilson loop and of center vortices are put under scrutiny. For the former, some arguments regarding its physical interpretation as a probe to the massive quark potential will be shown, as well as the appearance of an area law in the strong coupling limit. On the other hand, the relation of center symmetry breaking to the deconfinement phase transition and some lattice QCD results show the importance of the latter. Afterwards, a contemporary picture of pure gauge QCD vacuum is shown.

1.1 The Wilson loop and its physical interpretation

As it was previously stated, there is an order parameter that probes the confinement status of QCD. However, gauge invariance prohibits the existence of something akin to a magnetization, i.e. a simple sum of the degrees of freedom, given that averages of non-gauge-invariant local quantities are necessarily zero [24].

A solution to this problem is the introduction of the *Wilson loop* [70] defined in (2) in the introduction for the continuum. This is gauge invariant because group holonomies (the Wilson loop before taking the trace) in a line $\mathcal{C}$ from x to y transform as $G(x,y) \mapsto G'(x,y) = \Omega(x)G(x,y)\Omega^{\dagger}(y)$, by the continuum gauge transformations (A.6). So, if x and y coincide and one takes the trace, the resulting quantity is gauge invariant.

One way to grasp the physical significance of this quantity and to see how it probes confinement is to refer to again to the Lattice QCD formalism, outlined in Appendix A. In this context, it becomes

$$\mathcal{W}(\mathcal{C}) = \mathrm{tr}P \prod_{x,\mu\in\mathcal{C}} U_{\mu}(x). \tag{1.1}$$

where $U_{\mu}(x)$ denotes a link variable from site x to $x+\hat{\mu}$. To assist interpretation, it is necessary to take a standard form to the spacetime curve $\mathcal{C}$. It is built by four parts, two of them are called Wilson lines, $S(\mathbf{m},\mathbf{n},0)$ and $S(\mathbf{m},\mathbf{n},n_t)$, and the other two are called the temporal transporters $T(\mathbf{n},n_t)$ e $T(\mathbf{m},n_t)$.

The Wilson line $S(\mathbf{m},\mathbf{n},n_t)$ goes from $\mathbf{m}$ to $\mathbf{n}$ at fixed time n_t along some curve. Then the first temporal transporter takes from time n_t to 0, at a fixed space point $\mathbf{n}$. Now the second Wilson line goes from $\mathbf{n}$ back to $\mathbf{m}$ with a fixed time 0. Finally the second transporter $T(\mathbf{m},n_t)$ brings to the initial spacetime point $(\mathbf{m},n_t)$ in a fixed space point

m. In short,

$$(\mathbf{m}, n_t) \longmapsto (\mathbf{n}, n_t) \longmapsto (\mathbf{n}, 0) \longmapsto (\mathbf{m}, 0) \longmapsto (\mathbf{m}, n_t). \tag{1.2}$$

Hence, the Wilson loop is the trace of the product of the link variables that join the abovementioned points, which is similar to (1.1) but the arbitrarity is found only in the Wilson lines, namely,

$$\mathcal{W}(\mathcal{C}) = \mathrm{tr}[S(\mathbf{m}, \mathbf{n}, n_t)T^{\dagger}(\mathbf{n}, n_t)S^{\dagger}(\mathbf{m}, \mathbf{n}, 0)T(\mathbf{m}, n_t)], \tag{1.3}$$

sometimes, as in the next paragraphs, one may choose the Wilson lines to be straight, such that $\mathcal{C}$ is planar.

Another prescription before the physical interpretation itself is discussed, is to take the temporal gauge $A_0(x) = 0$ [1]. In such case, the temporal transporters are trivial, $U_0(x) = \mathbb{1}$. Thence

$$\langle \mathcal{W}(\mathcal{C}) \rangle = \langle \mathrm{tr}[S(\mathbf{m}, \mathbf{n}, n_t)S^{\dagger}(\mathbf{m}, \mathbf{n}, 0)] \rangle. \tag{1.4}$$

One then sees that the Wilson loop average reduces to the correlation function between $S(\mathbf{m}, \mathbf{n}, n_t)$ and $S^{\dagger}(\mathbf{m}, \mathbf{n}, 0)$. Then,

$$\lim_{t\to\infty} \langle \mathcal{W}(\mathcal{C}) \rangle = \lim_{t\to\infty} \langle S_{ab}(\mathbf{m}, \mathbf{n}, n_t) S^{\dagger}_{ba}(\mathbf{m}, \mathbf{n}, 0) \rangle = \sum_q \langle 0|S_{ab}(\mathbf{m}, \mathbf{n})|q\rangle\langle q|S^{\dagger}_{ba}(\mathbf{m}, \mathbf{n})|0\rangle e^{-E_q t} \,. \tag{1.5}$$

where it was used the result (A.34) for correlators in very large Euclidean time t. Another important and highly non-trivial result is that $S(\mathbf{m}, \mathbf{n})$ is the quark propagator in the large mass limit [32]. Thus the sum in (1.5) is over the states that describe quark-antiquark pairs, both very massive and located in **m** and **n**. In such a way, the lowest energy terms which are dominant in large euclidean times give us information about the energy of this pair, this energy can then be identified with the interquark potential $V(r)$. On that account,

$$\langle \mathcal{W}(\mathcal{C}) \rangle \sim e^{-n_t a V(r)}. \tag{1.6}$$

There are still other ways to look at the Wilson loop. Namely, it is a probe to vacuum fluctuations, when it is placed in a space-only plane [37], one might also observe from (2) that the Wilson loop reduces to the Aharonov-Bohm phase when one considers the usual electromagnetism. In such context, it is possible to introduce center vortices as singular gauge transformations from the $A_\mu = 0$ configuration [36]. In ref. [69] the author gives a differential geometry approach to the Wilson loop as being the operator

[1] It is important to emphasize that the Wilson loop is a gauge invariant, thus the gauge fixing serves merely as computational tool.

that implements the change in the color vector as one travels in closed loops in a manifold that has the gauge field A_μ as its connection.

This quantity will also of utmost importance in the present work, as it will become clear in chapter 3, where the effective model will be presented. This is highly motivated by the definition of center vortices in eq. (6).

1.2 The Strong Coupling Limit and the Area Law

One way to show the existence of the linear term in the interquark potential, as antecipated in (1), and the Area-law is to take the strong coupling limit $g \to \infty$ ou $\beta = 6/g^2 \to 0$. In such context, making use of the Wilson action (A.22), originally proposed in ref. [70], the average of Wilson loop,

$$\langle \mathcal{W}(\mathcal{C}) \rangle = \frac{1}{Z} \int [\mathcal{D}U] \exp\left[-\frac{\beta}{3} \sum_{\square} \text{Re tr}(\mathbb{1} - \mathbb{U}_{\mu\nu}) \right] \text{tr}\left[\prod_{n \in \mathcal{C}} U_\mu(n) \right], \tag{1.7}$$

can be expanded in β. For the purposes of the present text, (1.7) will be truncated in the first non vanishing term. In this equation, $U_\mu(n)$ denotes a link variable, $\mathbb{U}_{\mu\nu}$ a *plaquette* and $[\mathcal{D}U]$ the group-invariant measure. Thus, ignoring a constant term in the exponential above,

$$\begin{aligned} \langle \mathcal{W}(\mathcal{C}) \rangle &= \frac{1}{\tilde{Z}} \int [\mathcal{D}U] \exp\left[\frac{\beta}{6} \sum_{\mu\nu} \text{tr}(\mathbb{U}_{\mu\nu} + \mathbb{U}^\dagger_{\mu\nu}) \right] \text{tr}\left[\prod_{n \in \mathcal{C}} U(n) \right] \\ &= \frac{1}{\tilde{Z}} \int [\mathcal{D}U] \ \text{tr}\left[\prod_{n \in \mathcal{C}} U(n) \right] \sum_{j,k=0}^{\infty} \left(\frac{\beta}{6} \right)^k \frac{1}{j!k!} \left(\sum_{\mu\nu} \text{tr}\mathbb{U}_{\mu\nu} \right)^j \left(\sum_{\mu\nu} \text{tr}\mathbb{U}^\dagger_{\mu\nu} \right)^k . \end{aligned} \tag{1.8}$$

Where it was also used that Re tr $(\mathbb{U}_{\mu\nu}) = 1/2$ tr $(\mathbb{U}_{\mu\nu} + \mathbb{U}^\dagger_{\mu\nu})$. The exponential and the sum of traces were both expanded. As for the partition function $\tilde{Z}$, the first nonzero term is, using the fact that the group measure is normalized,

$$\tilde{Z} = \int [\mathcal{D}U] \ 1 + \mathcal{O}(\beta^2) \approx 1. \tag{1.9}$$

For the numerator, it is necessary to refer to the results shown in appendix A. From (A.56), one sees that the first term in the expansion (1.8), $\int [\mathcal{D}U] \text{tr}\left[\prod_{n\in\mathcal{C}} U(n)\right]$, vanishes. Hence from (A.58), one may see that the nonzero term with the smallest number of products of link variables must contain paired $U(n)$ and $U^\dagger(n)$. At this point it is important to stress that taking the hermitian conjugate of a plaquette amounts to change its orientation, as one can see from (A.21). From (A.58) it follows that

$$\int dU \ \text{tr}[VU] \ \text{tr}[U^\dagger W] = \frac{1}{3} \text{tr}[VW] \tag{1.10}$$

thus it is possible to deduce that, when integrating over a link variable that is common to two adjacent plaquettes, what is left over is a trace over the loop obtained by joining the plaquettes. This procedure is pictorially summarized in fig. 3.

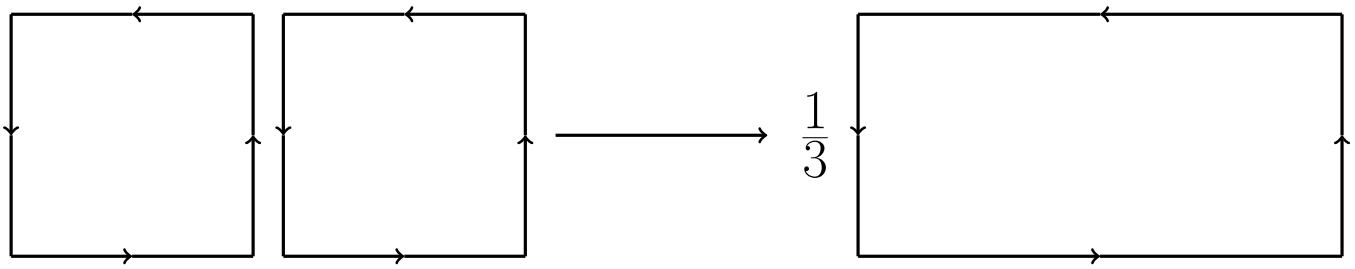

Figure 3 – The group integrals from appendix A.3 imply that the integral of products of traces over adjacent plaquettes reduces to the trace over the loop formed by the union of these plaquettes. Adapted from ref. [32].

For the sake of simplicity, let us take the Wilson loop to be a rectangle with n_t links in temporal direction and n_r links in a particular space direction. Along these lines, one can conclude that the lowest order contribution in β will come from a term such that the plaquettes "fit in" to form the Wilson loop, but with the orientation reversed (the internal links vanish with the group integral). This can be seen in fig. 4.

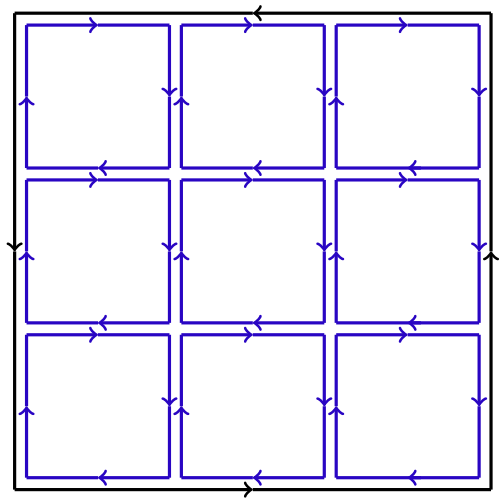

Figure 4 – Pictorial representation of the first non-vanishing term contributing to the strong coupling expansion. In blue, the plaquettes, in black the Wilson loop. Adapted from ref. [37].

In this case $n_r n_t$ plaquettes are needed, and as only those terms with $\mathbb{U}^\dagger_{\mu\nu}$ in (1.8) contribute, the Wilson loop average reduces to

$$\langle \mathcal{W}(\mathcal{C}) \rangle \approx \int [\mathcal{D}U] \frac{1}{(n_r n_t)!} \left(\frac{\beta}{6}\right)^{n_r n_t} \operatorname{tr}\left[\prod_{n\in\mathcal{C}} U(n)\right] \left(\sum_{\mu\nu} \operatorname{tr}\mathbb{U}^\dagger_{\mu\nu}\right)^{n_r n_t} + O(\beta) \tag{1.11}$$

and then, expanding the sum over plaquettes and leaving only those that "fit in" the inverse-oriented Wilson loop (there are $(n_r n_t)!$ such terms),

$$\langle \mathcal{W}(\mathcal{C}) \rangle \approx \left(\frac{\beta}{6}\right)^{n_r n_t} \int [\mathcal{D}U] \operatorname{tr}\left[\prod_{n\in\mathcal{C}} U(n)\right] \prod_{\mu\nu\subset\mathcal{S}(\mathcal{W})} \operatorname{tr}\mathbb{U}^\dagger_{\mu\nu}, \tag{1.12}$$

where $\mathcal{S}(\mathcal{W})$ is the minimal surface whose boundary is $\mathcal{C}$. Hence,

$$\langle \mathcal{W}(\mathcal{C}) \rangle \approx \mathrm{tr}[\mathbb{1}] \left(\frac{\beta}{6}\right)^{n_r n_t} \left(\frac{1}{3}\right)^{n_r n_t} = 3 \exp\left(n_r n_t \ln\left(\frac{\beta}{18}\right)\right). \tag{1.13}$$

Now, it is worth noting that $A(\mathcal{S}(\mathcal{W})) = n_r n_t a^2$, thus characterizing the Area Law. Furthermore, comparing (1.13) with (1.6),

$$e^{-n_t a V(r)} = 3 \exp\left(\frac{r}{a} n_t \ln\left(\frac{\beta}{18}\right)\right) \Rightarrow V(r) = \sigma r, \tag{1.14}$$

with

$$\sigma = -\frac{1}{a^2} \ln\left(\frac{\beta}{18}\right) \tag{1.15}$$

Where in (1.14) it was used that $r = n_r a$. As expected, this is not the final word, it is possible to calculate the expansion further and find higher order corrections to the string tension σ [16], but these are not in the scope of the present work. In any case, terms such as (A.59) start to contribute as well.

1.3 The Center Symmetry

As it was already mentioned, the term confinement can be viewed as a way to describe a phase of a gauge theory. In statistical physics models, phases are in general characterized by the existence of some order parameter and the breaking of some symmetry, as it happens in a Ising magnet below Curie temperature, where the spin sign inversion symmetry of the interaction is spontaneously broken by a finite magnetization. To specify the symmetry in the present case, first one might consider again the lattice Wilson action for lattice QCD

$$S_C[U] = \frac{2}{g^2} \sum_{n,\mu<\nu} \mathrm{Re} \;\; \mathrm{tr}\left(\mathbb{1} - \mathbb{U}_{\mu\nu}\right) \;, \tag{1.16}$$

that has the following symmetry

$$U_0(\mathbf{x}, t_0) \mapsto C U_0(\mathbf{x}, t_0) \;\; \forall \mathbf{x},\, t_0 \text{ fixed and } C \in Z(N), \tag{1.17}$$

because the temporal plaquettes, the only one that would possibly be affected, are invariant, namely,

$$\mathbb{U}'_{\mu 0} = U_\mu(n) C U_0(n+\hat{\mu}) U_{-\mu}(n+\hat{\mu}+\hat{0}) U_{-0}(n+\hat{0}) C^\dagger = U_\mu(n) U_0(n+\hat{\mu}) U^\dagger_\mu(n+\hat{0}) U^\dagger_0(n) = \mathbb{U}_{\mu 0}. \tag{1.18}$$

The symmetry (1.17) is broken either spontaneously at high temperatures [37], or explictly by the addition of matter. In both cases, the static quark potential is *not* asymptotically linear. The first case is probed with a Polyakov loop, a Wilson loop that winds around the periodical euclidean time. Its physical interpretation is that it is

proportional to $e^{-\beta F_q}$, where β is the inverse temperature and F_q is the free energy of a isolated quark.

Thus, an infinite quark free energy, i.e. confinement, is a necessary and sufficient condition to have a vanishing Polyakov loop average. This quantity is *not* invariant under (1.17), so that a vanishing value of its average indicates that the underlying symmetry is unbroken. Hence one identifies the unbroken center symmetry phase with the confined phase and the broken one with the deconfined phase. In this sense, the Polyakov loop is an order parameter for confinement at finite temperatures. Numerical evidence that support these claims can be found in refs. [31, 33].

In the case with dynamical matter fields, the Center Symmetry is broken by the matter-gauge coupling, depending on the group representation used. To see this, a few remarks about representation theory are needed. As it can be seen in (5), the center of $SU(N)$ is a discrete group, thus there is a finite number of representations to it. To $Z(N)$, there are exactly N of them. Thus, each $SU(N)$ representations can be separated in subsets that are labeled by a center element, the name of this label is the so-called *N-ality* [2]. If a representation ρ has N-ality $0 \leq k \leq N-1$, then $\rho(zM) = z^k \rho(M)$.

Thus if a matter term, for instance $\phi^\dagger U_\mu \phi + c.c.$, for a scalar field ϕ, is added to the pure gauge lattice lagrangian, and the N-ality of this representation is non-zero, then the Center Symmetry is broken. Otherwise, as in the case of gluons, which are in adjoint representation, which has zero N-ality, it is not.

If the matter fields are to screen the static quarks, produce colorless states and break the string, these must be in a representation such that the tensor product between the two representations produces a color singlet. This information is contained in the N-ality: $k = 0$ fields can not alter the N-ality of the source, so gluons can not screen sources that have $k \neq 0$, whereas fundamental quarks, that have $k = 1$ can always do do so. Then, the matter fields which are expected to break the string also break the Center Symmetry.

1.4 The Maximal Center Gauge, Center Projection and the contribution of Center Vortices to the confining force

Due to their effect in a gauge invariant quantity (6), the center vortex content must also be gauge invariant. Nonetheless, the only gauge where there seems to be a well defined continuum limit to vortex properties is the Maximal Center Gauge [63]. The procedure that defines the fixing of this gauge involves bringing all link variables as close as possible

[2] More information about the N-ality will be given in section 2.1

to center elements. This is done by first maximizing the functional

$$\mathcal{M}[U] = \sum_{\mathbf{x},\mu} |\mathrm{tr} U_\mu(\mathbf{x})|^2. \tag{1.19}$$

In the case where the $U_\mu \in SU(2)$, as the link variables can be parametrized as $U_\mu = \alpha_0 \mathbb{1} + i\alpha \cdot \sigma$, where σ_i are the Pauli matrices and $\alpha_0^2 + \alpha^2 = 1$. As tr $\sigma_i = 0$, maximizing each term of (1.19) is equivalent to maximizing α_0^2.

Afterwards the *center projection* is done, in this procedure, each link variable is substituted by the closest corresponding center element. The only non-trivial configurations that remain are Center Vortices (in purple in fig. 5). Thus taking a configuration such that there are surfaces with non-trivial link variables, the only non-trivial contribution to Wilson loop averages come if the loop and the former surfaces link each other. The boundary of these surfaces is where one localizes center vortices [63].

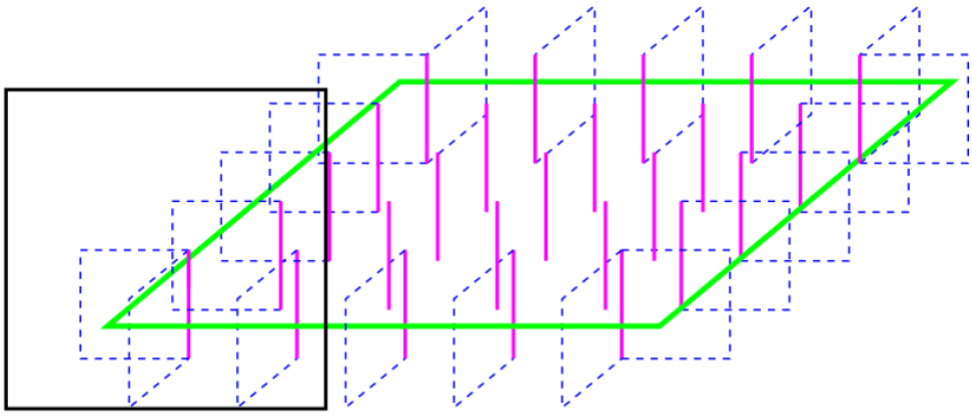

Figure 5 – Non-trivial link configuration after center projection (in purple) and the center vortex configuration associated with it. In black, a Wilson loop that links with the vortex, giving a non-trivial contribution. Taken from ref. [63].

Lattice computations like in ref. [47] give evidence that center vortices are indeed the configurations responsible for the confinement phenomenon in QCD vacuum. The way one may imply this is to contemplate the effect of withdrawing the vortex contribution to the interquark potential. This is done by multiplying each link variable by its (hermitian-conjugated) center-projected "component". Specifically, $U_\mu(x) \mapsto U_\mu(x) C_\mu^\dagger(x)$. This prescription implements the contribuition of a opposite-oriented vortex above the previous one, anihilating its contribution to Wilson loop averages. In fig. 6 one may see a result of this procedure for two gauge groups.

So, in the complete theory, at small distances the potential is mostly the Coulomb one, and at bigger distances, pratically linear. With center-projected lattices, the potential rises linearly. In the case of $SU(2)$, the line slope is almost completely recovered by center projection, a property that is called *center dominance*. With vortex removal, the potential saturates in a constant and confinement properties are thus lost.

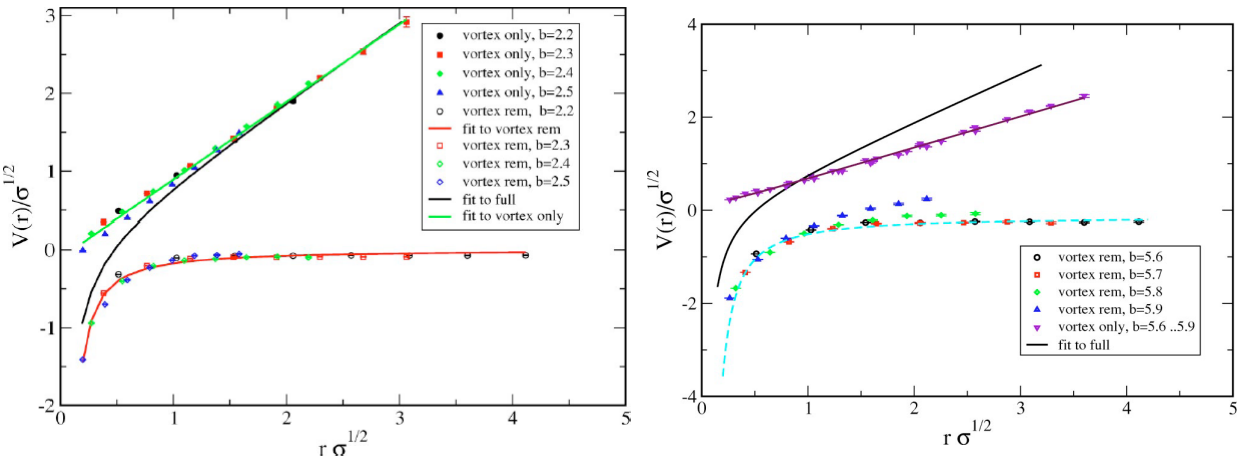

Figure 6 – To the left (right): interquark potential versus their separation in a SU(2)(SU(3)) Yang-Mills theory, the full potential is in black, the center-projected potential is in green (purple) and the center-excluded potential is in red (light blue). Taken from ref. [47].

One also perceives that for $SU(3)$ the linear part slope is not at all completely recovered. This indicates that other configurations might contribute to the full potential. Thus, the aforementioned monopoles may play this role. If this is to be true, a joint picture of confinement is needed. In fact, one may see evidence [4] that in fact monopoles become "glued" to center vortices worldlines, as pictorially represented in fig. 7. More recently [59], there have been efforts to define gauges in the continuum that detect such topological defects in gauge field configurations.

Although this picture will not be used in the effective model to be discussed, it is an important contemporary vision of pure gauge QCD vacuum, and it might even motivate future developments of the effective models.

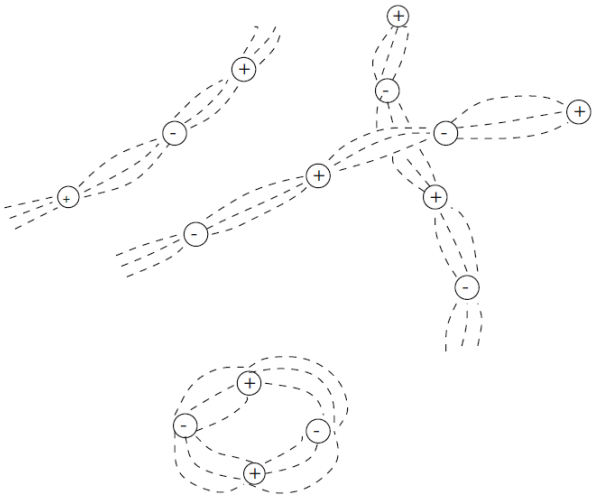

Figure 7 – Monopole-antimonopole flux colimation in center vortices' worldlines. Taken from ref. [4].

2 Further properties of the confining force and of Center Vortices

Besides the properties mentioned in the previous chapter, there are many other aspects of the confining force that can be deduced from LQCD simulations and/or holography studies. The results presented in this chapter form the basis for the effective model that will be developed in the next chapter. Moreover, the ones in section 2.1 will be used as a consistency check for the effective model, as not all the properties described here will be taken into account there.

2.1 Representation dependence of the String Tension

One important point to adress is how the string tension behaves as one changes the representation of the gauge group. Results in this direction state that $\sigma_R \propto \sigma_F$, where R denotes a arbitrary representation of the gauge group and F its fundamental representation. The first kind of these studies [5] reveal that, at weak couplings and $D = 2$, where analytic Wilson loop calculations are more feasible, the inclination of the interquark potential at intermediate distances obeys

$$\sigma_R = \frac{C_R}{C_F}\sigma_F \tag{2.1}$$

where C_r is the quadratic Casimir of the representation $r = R, F$, that is defined by

$$\sum_a R(T_a)R(T_a) = C_R \mathbb{1}, \tag{2.2}$$

where $R(T_a)$ is the a-th Lie algebra generator in representation R [41]. Thus eq. (2.1) is called *Casimir scaling*. For $SU(2)$, $C_r = j(j+1)$, which correspond to the eigenvalues of total angular momentum squared in units of $\hbar^2$.

It is possible to argue that the above mentioned $D = 2$ calculation somehow reflects the $D = 4$ case through a *dimensional reduction* [5], the idea that somehow the calculations in the former dimension yield calculations the latter. That holds true for the leading term of strong coupling expansion, and might also surprisingly work for weak couplings [35, 57]. There is indeed compeling lattice QCD evidence that this is true from ref. [8], whose main result is displayed in fig. 8 for $SU(3)$ in $D = 4$.

For larger separations, it is energetically favorable for gluons to screen the static charges and form two separated bound states formed by one static quark and the gluons. This is somewhat similar to the mechanism discussed in the previous chapter, now not only this mechanism is enabled by gluons instead of dynamical quarks (as only the effects of

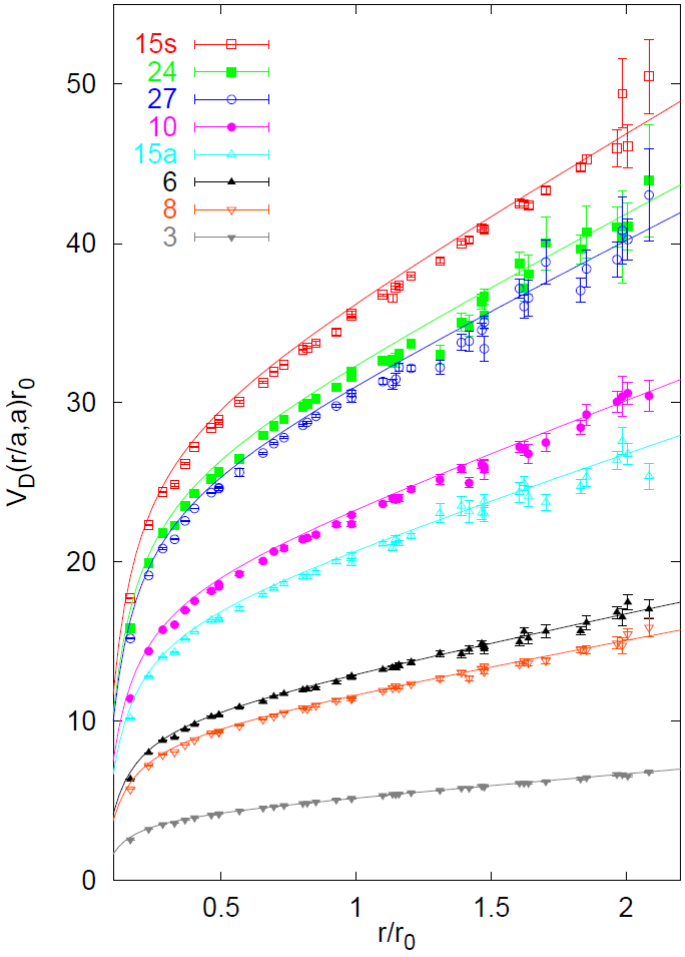

Figure 8 – Lattice QCD evidence for Casimir Scaling for $SU(3)$. Each continuous line for higher representations is obtained from the fit of the fundamental one by multiplying the quadratic Casimir factor. Taken from ref. [8].

the former are considered), but also the string might not break. This is because gluons are in the adjoint representation, and they might form states that are not colorless depending on the representation of the static source.

One might also ask how this residual string tension (called k-string) depends on the representations of the gauge group. In this context, two main results arise, the first one is called *Casimir Law* and it reads [20, 21]

$$\sigma_R = \sigma_N(k_R) = \frac{k_R(N - k_R)}{N - 1}\sigma_F \tag{2.3}$$

which stems from the fact that the factor that multiplies σ_F can be shown to be quadratic Casimir of the anti-symmetric representation with *N-ality* k_R normalized by the Casimir of the fundamental representation. Another possibility for the representation dependence

stems from supersymmetry studies [23, 42] suggest that

$$\sigma_R = \sigma_N(k_R) = \frac{\sin\left(\frac{\pi k}{N}\right)}{\sin\left(\frac{\pi}{N}\right)}\sigma_F \tag{2.4}$$

which is called a *Sine Law*.

In both of the previous equations k_R is the N-ality of representation R, that is also the number of squares in a Young Tableau of the representation mod N. For instance, when and $r = F$, $k_F = 1 \bmod N = 1$; if $r = A$ (adjoint representation), $k_A = N \bmod N = 0$. This quantity remains unaltered when one takes tensor products of some representation by the adjoint, so gluons in the latter representaion can not break strings with a nonzero N-ality, as stated earlier. It is also worth noticing that for $N >> 1$, both string tension dependences yield $\sigma(k_R) \approx k\sigma_F$, hence it is increasingly difficult to distinguish between the two laws.

It can be readily seen that $\sigma_A = 0$, thus implying in another string breaking mechanism when one has gluons and static quarks in the adjoint representation. The final state after the "k-string breaking" is called a *gluelump*. Numerical evidence to this string breaking can be found in ref. [19].

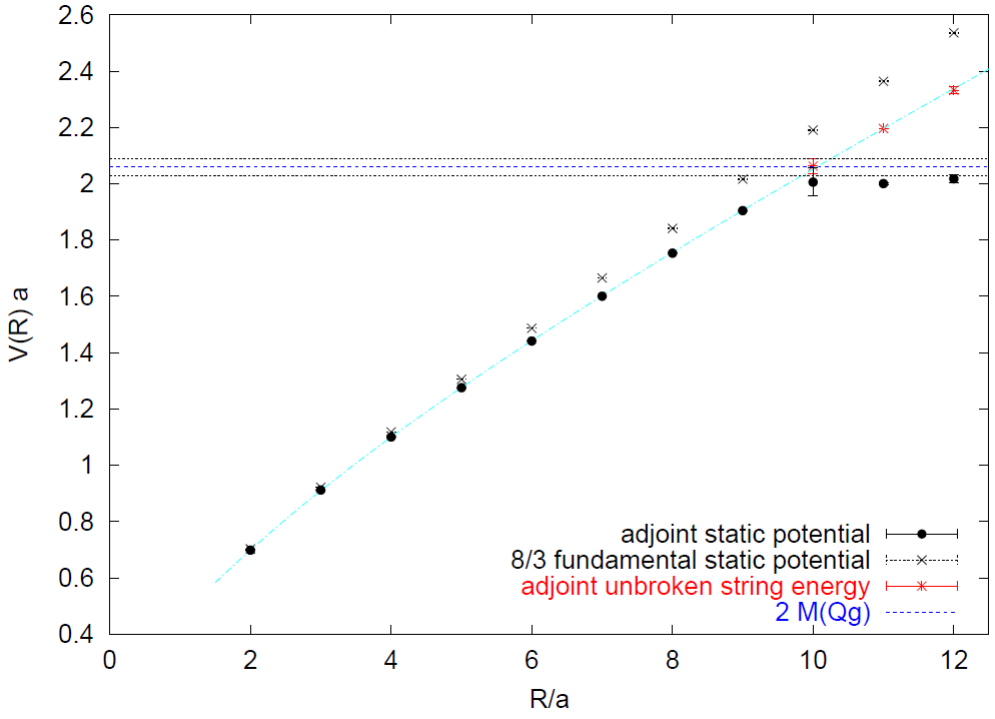

Figure 9 – Lattice QCD evidence for k-string breaking with gluons. Taken from ref. [19]

2.2 Tension, Stiffness and Percolation of Center Vortices

Inspired by the Center Dominance property, one is naturally lead to think, formally, that one can grasp all the confinement information in Yang-Mills vacuum if one takes averages of observables such as the Wilson loop, with a effective model where all the $SU(N)/Z(N)$ degrees of freedom are integrated out. With this in mind, and endowed with a continuum analogue of the maximal center gauge, the authors of ref. [28] performed a gradient expansion of the Yang-Mills action and arrived at a effective model in D dimensions, which reads

$$S = \int_{\partial\Sigma} d^2\sigma\sqrt{g}\ (\epsilon + c\ K^A_{ai}K^A_{bj}g^{ab}g^{ij}) \tag{2.5}$$

$$g = \det g_{ab}, \qquad g_{ab} = \partial_a x^\mu \partial_b x^\mu. \tag{2.6}$$

where g_{ab} and K^A_{ij} denote respectively metric and the extrinsic curvature of the center vortex hyper-surface $\partial\Sigma$. The equation above can be related to the leading and sub-leading Nambu-Goto action in D dimensions.

In further studies, a lattice version of (2.5) is analyzed for $SU(2)$ [29, 30] and $SU(3)$ [27, 62], and $D = 4$, where vortices are 2-surfaces. In the latter case the center consists of the set $Z(3) = \{1, e^{\pm i\frac{2\pi}{3}}\}$, and the elementary variables to this discussion are the plaquettes $\mathbb{U}_{\mu\nu}$, but as far as the center projection procedure is concerned, these can be completely determined by the *triality* $k_{\mu\nu} \in \{0, \pm 1\}$, so that $\mathbb{U}_{\mu\nu} = e^{i\frac{2\pi}{3}k_{\mu\nu}}$. Hence non-zero $k_{\mu\nu}$ means that the plaquette in question belongs to the the center vortex world surface. Then,

$$\begin{aligned} S = \ \epsilon \sum_x \sum_{\substack{\mu,\nu \\ \mu<\nu}} |k_{\mu\nu}(x)| + c \sum_{x,\mu} \Bigg(& \sum_{\substack{\nu<\lambda \\ \nu\neq\mu,\lambda\neq\mu}} |k_{\mu\nu}(x)k_{\mu\lambda}(x)| + |k_{\mu\nu}(x)k_{\mu\lambda}(x-\hat{\lambda})| \\ & + |k_{\mu\nu}(x-\hat{\nu})k_{\mu\lambda}(x)| + |k_{\mu\nu}(x-\hat{\nu})k_{\mu\lambda}(x-\hat{\lambda})| \Bigg). \end{aligned} \tag{2.7}$$

One can see that a ϵ penalty arises whenever the non-zero $k_{\mu\nu}$ are located at a surface area, and that a c penalty arises whenever plaquettes which share the same link, but are in different planes have non-zero $k_{\mu\nu}$.

Taking Wilson loop averages, which is defined by counting how many vortices pierce its minimal area, one can perform a survey in the coupling constant space and find that there is a confined (nonzero string tension) and a deconfined (zero string tension) phase as seen in fig. 10.

They extracted the physical meaning from the coupling constants ϵ and c by requiring that they reproduce the ratio $T_c/\sqrt{\sigma_0} \approx 0.63$, where T_c is the critical temperature for the deconfinement transition and σ_0 is the string tension at zero temperature [1]. This

[1] Zero temperature simulations are those in which all four euclidean coordinates have equal and big

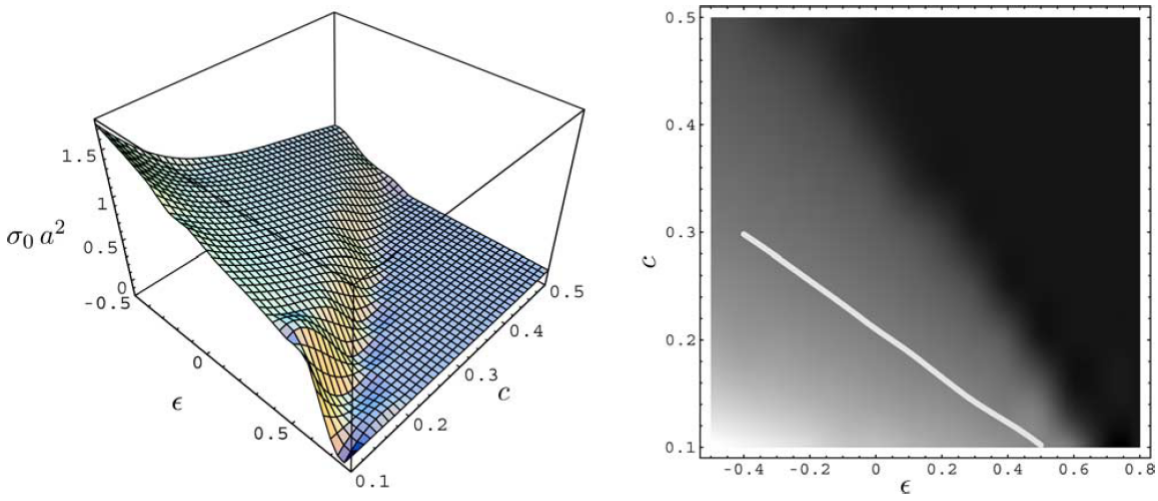

Figure 10 – (Left) Zero temperature string tension $\sigma_0 a^2$ dependence on the coupling constants (ϵ, c). (Right) A density plot version of the $\sigma_0 a^2$ dependnce on the coupling contants. The white line represents that points such that $T_c/\sqrt{\sigma_0} \approx 0.63$. Taken from ref. [27].

ratio was originally obtained in full $SU(3)$ lattice simulations in ref. [12]. This property was shown to be satisfied at a approximately constant physics line in the (ϵ, c) space that is contained in the confining region.

Afterwards, choosing the point $(\epsilon, c) = (0, 0.21)$ in this line, thus fixing all physical parameters, the string tension dependence on the temperature is predicted. It was found that a spatial string tension persists even at temperatures above the deconfinement transition, whereas the usual string tension, that has both time and spatial extension, drops to zero. Furthermore, they found that the deconfining phase transition is weakly of first order, that agrees with results found previously in ref. [3].

The authors also concluded that percolation and confinement properties are intimately related for both $SU(2)$ and $SU(3)$ cases. They first considered space slices of the lattice, where one of the space coordinates is fixed. In these slices, the vortices forms closed loops. Looking at histograms for the number of vortex clusters for the various lengths as they changed the temperature of the system, they found that below T_c, most of the vortices have the maximal lattice length, whereas above it, small, disconected ones prevailed. The data can be seen in fig. 11. Considering time slices, however, the picture changes. And in this case vortices percolate in both phases.

To gain intuition on percolation one can analyze a random vortex model [26, 30] (in $SU(2)$, for the following). Postulating that vortices do not percolate implies that there is a maximum characteristic length $l_{v,max}$ possible. Because vortices are closed, if one of

extensions, a lattice of 16^4 is an example. For finite temperatures, one of the extensions is different and it is identified with the Euclidean time, and the bigger the time extension, the smaller the temperature, a lattice of $16^3 \times 2$ is an example of high temperature simulation.

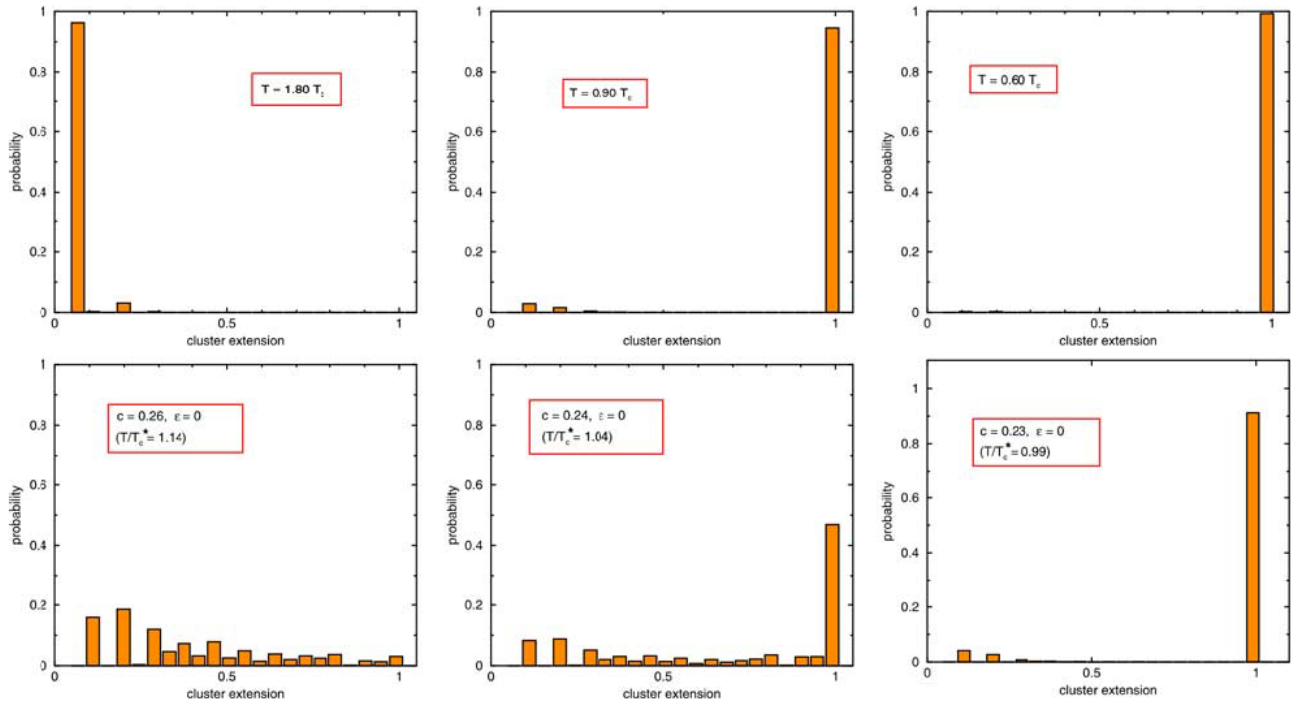

Figure 11 – Vortex cluster extension histograms. The top line was obtained at couplings $(\epsilon, c) = (0, 0.21)$. The bottom line shows histograms for coupling constants slightly out of the physical line. Taken from ref. [27].

them pierces a surface at a given point, another piercing point will be found at most $l_{v,max}$ away, if the Wilson loop is sufficiently large.

Distributing these pairs randomly, one can analyze Wilson loop averages in a lattice with Euclidean time length (inverse temperature) $L_t = L$ and one of the space extentions being $L_x = L$, so that this loop is in xt plane. If the probability that the contribution from one such pair to be -1 is p_c, the probability that this contribution is actually realized is $(p_c) \cdot A/(L^2)$ where $A = Pl_{v,max}$ is the area of a ribbon centered on the Wilson loop trajectory, $L^2 = L_x L_t$ is the total xt-plane area, and P is the perimeter of the Wilson loop.

Putting N_p pairs in the xt-plane, the probability that N_c of them will contribute is

$$P_{N_p}(N_c) = \binom{N_p}{N_c} \left(\frac{p_c P l_{v,max}}{L^2}\right)^{N_c} \left(1 - \frac{p_c l_{v,max}}{L^2}\right)^{N_p - N_c} \tag{2.8}$$

so that the expectation value of the Wilson loop is

$$\begin{aligned} \langle \mathcal{W}(\mathcal{C}) \rangle &= \sum_{N_c=1}^{N_p} (-1)^{N_c} P_{N_p}(N_c) = \sum_{N_c=1}^{N_p} \binom{N_p}{N_c} \left(-\frac{p_c P l_{v,max}}{L^2}\right)^{N_c} \left(1 - \frac{p_c P l_{v,max}}{L^2}\right)^{N_p - N_c} \\ &= \left(1 - \frac{2p l_{v,max}}{L^2}\right)^{N_p} \end{aligned} \tag{2.9}$$

If one takes the limit $N_p \to \infty$ with the number piercings per unit of area points

$\rho = 2N_p/(L^2)$ being fixed, $\langle \mathcal{W}(\mathcal{C}) \rangle = e^{-p_c Pl_{v,max}\rho}$. Thus this gives a perimeter law for that quantity, which means deconfinement.

In the other hand, if vortices percolate, there is no such pair correlation and each piercing point is distributed independently. Again, if there are N_p points to be distributed in the xt plane, the probability that N_c of them pierce the Wilson loop is

$$P_{N_p}(N_c) = \binom{N_p}{N_c} \left(\frac{A}{L^2}\right)^{N_c} \left(1 - \frac{A}{L^2}\right)^{N_p - N_c}, \tag{2.10}$$

where A is the minimal area of the Wilson loop. Thus expectation value of such quantity is

$$\begin{aligned} \langle \mathcal{W}(\mathcal{C}) \rangle &= \sum_{N_c=1}^{N_p} (-1)^{N_c} P_{N_p}(N_c) = \sum_{N_c=1}^{N_p} \binom{N_p}{N_c} \left(-\frac{A}{L^2}\right)^{N_c} \left(1 - \frac{A}{L^2}\right)^{N_p - N_c} \\ &= \left(1 - \frac{2A}{L^2}\right)^{N_p}. \end{aligned} \tag{2.11}$$

If the limit $N_p \to \infty$ is taken with a density $\rho = N_p/L^2$ fixed, $\langle \mathcal{W}(\mathcal{C}) \rangle = e^{-2A\rho}$, thus giving an area law with $\sigma = 2\rho$, and hence implying confinement. The resulting intuition is that percolation is a necessary condition for confinement, and a pictorial representation of the behavior of center vortices in both phases are seen in fig. 12.

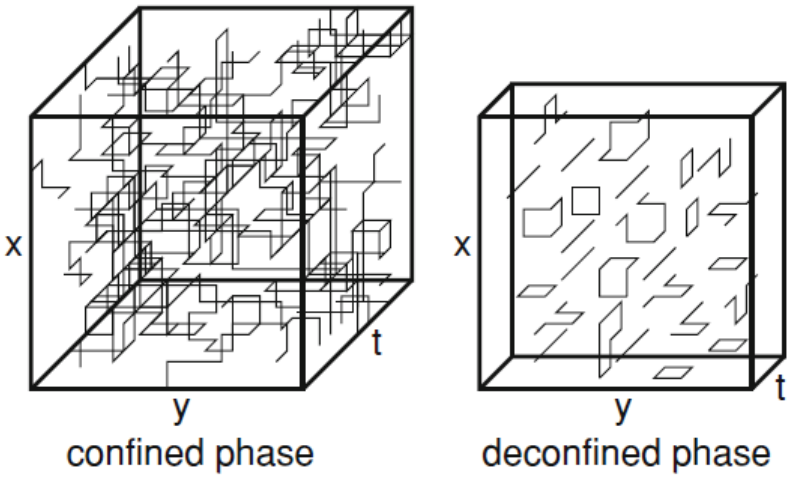

Figure 12 – (Left) Vortex worldline percolation in confined phase in YM theory. (Right) Small and sparse vortices still remain in deconfined phase. Taken from ref. [26].

Finally, the persistance of a spatial string tension that was observed can be explained in terms of percolation. First, it can be seen that a spatial Wilson loop can be inserted both in time slices and spatial slices. In the former, however, percolation does not happen after deconfinement transition, and vortices are of limited length. Vortex percolation persistance in the latter picture can thus be seen as a result of vortices winding the periodic Euclidean time, which at higher temperatures, has smaller lengths, hence enabling even limited length vortices, that dominate the deconfined phase, to percolate.

2.3 Interaction between Center Vortices

As usual with heuristic formulations, the ideal random vortex idea presented in the last section is not quite correct when considering a more profound scrutiny. In ref. [48] it is indeed shown, for $SU(2)$, that ρ, the planar vortex density, is a physical quantity because it shows the correct scaling towards continuum. However, the value of the string tension $\sigma = 2\rho$ obtained is 17 % off in comparison with the most accepted value of $\sigma_{acc} = (440 \text{ MeV})^2$ [55]. This is evidence that vortex correlation is indeed important.

In ref. [25] the authors analyze the normalized vortex correlation

$$c_{ij} = \frac{\langle s_i s_j \rangle}{\langle s_i \rangle \langle s_j \rangle} \tag{2.12}$$

where, s_i is a variable that returns 1 if the plaquette i belongs to a vortex and is 0 elsewhere. It is important to stress that $\langle s_i \rangle = \rho a^2$. Due to rotational invariance, $c_{ij} = c(r)$ where r is the distance between plaquettes. Then, the plaquettes under scrutiny are put in the same plane, l lattice spacings from each other, so that $r = la$. This quantity is also shown to have the correct renormalization group scaling, meaning that this is a physical quantity as well. This can be interpreted as evidence that vortex interaction is a physical phenomenon.

What was observed is the decay of the correlation with a characteristic length of $r_{ch}^M = 0.6$ fm. This is defined as the region where the correlator is 1 within error bars. Hence r_{ch}^M can be thought of as a upper limit for vortex interaction. A lower bound can be extracted from the data by fitting an exponential to it. The value thus found is $r_{cm}^m = 0.2$ fm. It should nevertheless be noted that interaction is not the only aspect that the correlation is sensitive to, it can also detect effects stemming from curvature of a single vortex, for instance.

2.4 Branching of Center Vortices

From the evidence available in ref. [27] one is reminded that center vortices have a *branching* property. This stems from the fact that, for $N \geq 3$, it is possible to have vortices with different N-alities k appearing in QCD's vacuum, and, one can have $k = 2$ vortices that bifurcate in two $k = 1$ vortices as it can be seen in fig. 13.

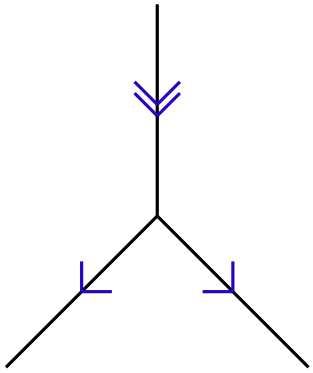

Figure 13 – The branching of a $k = 2$ link into two $k = 1$ links in a $D = 3$ slice. Adapted from ref. [27].

The physical effect associated with this property that motivates the analysis is the change in the order of the deconfinement phase transition from second order in $SU(2)$ to weakly first order in $SU(3)$. What the authors did to put branching under scrutiny was to count the number of vortex surfaces meeting at each link, ν, at spacetime slices: (i) $\nu = 0$ indicates that the link does not belong to any vortex; (ii) $\nu = 1$ is forbidden because vortices are closed; (iii) $\nu = 2$ denotes vortices that do not branch or self intersect on the refered link; (iv) $\nu = 4, 6$ mean self-intersections that are already accounted for in the $SU(2)$ case and (v) $\nu = 3, 5$ represent the new effect brought by $SU(3)$.

Then it follows an analysis for zero temperature and high temperature (i.e. confined and deconfined phases) at the aforementioned physical point $(\epsilon, c) = (0, 0.21)$, whose results show that:

- For zero temperature most of the vortices are in case (iii) above, hence non branching vortices. Nevertheless cases (iv) and (v) occur significantly often, indicating vortices form a quite fibrous structure;
- For the high temperature case, for time slices the qualitative feratures do not change, even though the probability for the occurence of cases (iv) and (v) grows, this is in consonance with the previous result that vortices percolate even at the deconfined phase at time slices;
- For space slices, the picture changes drastically, cases (i) and (iii) are privileged in detriment of cases (iv) and (v). The fibrous scenario in the confined phase is

substituted by small, unbraching vortices that usually do not touch each other and do not percolate;

- The number of links that belong to vortices drops from 85 % in the confined phase to about 50 % in the deconfined one, thus evidencing that it is not the vortex density that enables deconfinement transition, but percolation instead.

3 The effective model of Center Vortices and the three-dimensional frustrated XY model

Considering some of the properties discussed during the preceding chapter, the authors of ref. [58] developed a effective model that involves a ensemble of closed one-dimensional objects in 2+1 Euclidean dimensions. Its purpose is to reproduce the main features of a center projected Yang-Mills theory.

3.1 The Center Vortex effective model

The ensemble of these objects is distributed according to the action

$$S_n[x_\mu] = S_0^n + S_{int}^n \tag{3.1}$$

$$S_0^n = \sum_{j=1}^{n} \int_0^{L_j} ds_j \left[\mu + \frac{1}{2\kappa}\left(\dot{u}_\mu^{(j)}\right)^2\right] \qquad S_{int}^n = \frac{1}{2\zeta}\sum_{j,q}\int_0^{L_j}\int_0^{L_q} ds_j ds_q \; \delta(x^{(j)}(s_j) - x^{(q)}(s_q)), \tag{3.2}$$

where n is the vortex number. The first term in S_0^n accounts for the fact that there is a cost $\mu_j = \mu$ for the worldline length of the k-th vortex. If $\mu > 0$, then it favors small vortices, else, if it is negative, it favors percolating vortices; the second term stems from the action cost $1/2\kappa$ due to vortex curvature, there $u_\mu^{(j)}(s) = dx_\mu^{(j)}/ds$. Finally, S_{int}^n takes into account a contact interaction between the vortices.

Remembering that the contribution of Center Vortices to Wilson loop averages is a phase that depends on the linking number between the vortex worldline, ℓ (the j index will be dropped for the moment), and the Wilson loop itself, $\mathcal{C}$, they rewrite the exponent of eq. (6), specifically,

$$2\pi\frac{k}{N}L(\ell,\mathcal{C}) = \frac{k}{2N}\oint\oint \epsilon_{\mu\nu\lambda}\, dy_\mu\, dx_\nu \frac{y_\lambda(\tau) - x_\lambda(s)}{|y(\tau) - x(s)|^3}. \tag{3.3}$$

in which $x_\mu(s)$ ($y_\mu(\tau)$) parametrizes ℓ ($\mathcal{C}$), in a way that s and τ is the worldline ℓ (the loop Wilson loop $\mathcal{C}$) arc length, thus implying that the tangent vector is always normalized, $u_\mu(s) \in S^2$. Using Stokes' Theorem in the dy_μ integral,

$$2\pi\frac{k}{N}L(\ell,\mathcal{C}) = \oint_{\mathcal{C}} dy_\mu\, A_\mu^\ell(y) = \int_{\mathcal{S}(\mathcal{W})} B_\mu^\ell(y)\, dS_\mu \tag{3.4}$$

with

$$B_\mu^\ell(y) = \epsilon_{\mu\nu\lambda}\partial_\nu A_\lambda^\ell(y) = \frac{k}{2N}\oint_\ell ds\; u_\mu(s)\delta(y - x(s)), \tag{3.5}$$

$$dS_\mu = \epsilon_{\mu\nu\lambda}\frac{\partial y_\nu}{\partial\sigma_1}\frac{\partial y_\lambda}{\partial\sigma_2}\, d\sigma_1 d\sigma_2. \tag{3.6}$$

and $\mathcal{S}(\mathcal{W})$ is a surface whose boundary is $\mathcal{C}$. Then, switching the integral over $\mathcal{S}(\mathcal{W})$ in (3.4) with the one over ℓ in (3.5) and defines

$$J_\mu^{\mathcal{C}}(x) = \frac{k}{2N}\int_{\mathcal{S}(\mathcal{W})} dS_\mu \delta^{(3)}(y(\sigma_1,\sigma_2) - x), \tag{3.7}$$

that is located in $\mathcal{S}(\mathcal{W})$, with $y(\sigma_1,\sigma_2)$ being one of its parametrizations, thus

$$\mathcal{W}(\mathcal{C}) = e^{i2\pi\frac{k}{N}L(\ell,\mathcal{C})} = e^{i\oint_\ell dx_\mu J_\mu^{\mathcal{C}}} = e^{i\oint_{\mathcal{C}} dx_\mu J_\mu^{\ell}}. \tag{3.8}$$

where the last equality is valid due to the fact that the linking number does not change if one permutes ℓ and $\mathcal{C}$. (3.7) implements the idea that the linking number with a curve can also be seen as the intersection number with a surface whose boundary is that curve. Moreover from the last equality of (3.8), one is lead to the fact that A_μ^ℓ and J_μ^ℓ must be equivalent. Then the Wilson loop average becomes

$$\langle \mathcal{W}(\mathcal{C})\rangle = \frac{1}{Z[0]}\sum_n \int [\mathcal{D}l]_n \; e^{i\sum_{j=1}^n \oint_\ell dx_\mu J_\mu^{\mathcal{C}}} \; e^{-S_n[x_\mu]} = \frac{Z[J_\mu]}{Z[0]}. \tag{3.9}$$

3.2 Obtaining the frustrated 3D XY model

After some highly non-trivial steps the authors of [58] obtain the following complex field theory

$$Z[J_\mu] \approx \int [\mathcal{D}V][\mathcal{D}\bar{V}] \exp\left[-\int d^3x \frac{1}{3\kappa}\overline{D_\mu V} D_\mu V + \mu \bar{V}V + \frac{1}{2\zeta}(\bar{V}V)^2\right], \tag{3.10}$$

with $D_\mu = \partial_\mu - iJ_\mu$. the V-field significance in terms of the original ensemble is that

$$\langle \rho(x_1)...\rho(x_m)\rangle = \langle \bar{V}V(x_1)...\bar{V}V(x_m)\rangle \tag{3.11}$$

$$\langle B_\mu(x_1)...B_\mu(x_m)\rangle = \langle K_\mu(x_1)...K_\mu(x_m)\rangle, \text{ with} \tag{3.12}$$

$$K_\mu = \frac{\pi}{3N\kappa}(V\partial_\mu\bar{V} - \bar{V}\partial_\mu V) \tag{3.13}$$

Thus correlation functions involving $\bar{V}V$ are related to the vortex scalar density and B_μ correlation functions are related to the conserved current of that model by the symmetry $V \mapsto e^{i\alpha}V$, $\bar{V} \mapsto e^{-i\alpha}\bar{V}$.

Subsequently, one may analyze what happens to the center vortex picture when the sign of μ varies. If $\mu > 0$, the usual perturbative methods can be employed. On the other hand, if $\mu < 0$, the effective theory has a spontaneous $U(1)$ symmetry breaking and perturbative methods are no longer valid. In fact, the latter $\mu < 0$ case is the correct one because evidence seen in section 2.2 state that the vortex worldline percolates in the Yang-Mills vacuum. For an alternative discussion, relative to ensemble of proliferating objects, see ref. [38].

So, to correctly consider quantum fluctuations over the $\bar{V}V = -\mu\zeta \equiv v_0$ vacuum, which according to (3.11), means a constant average scalar vortex density of $\langle\rho(x)\rangle = v_0$, one ought to consider[1] $V = v_0\ e^{i\theta(x)}$.

Afterwards the lattice formulation for the θ field is obtained with the prescription

$$(\partial_\mu - iJ_\mu)V(x) \mapsto \frac{1}{a}\left(e^{i\theta(\mathbf{x}+\hat{\mu})} - U_\mu(\mathbf{x})e^{i\theta(\mathbf{x})}\right) \tag{3.14}$$

$$U_\mu(\mathbf{x}) = e^{i\int_{\mathcal{L}(n;\mu)} J^{\mathcal{C}}_\mu ds_\mu} \tag{3.15}$$

Where the lattice $\{\mathbf{x}\}$ has M sites and spacing a. Then using (3.7) one gets to

$$S_{XY}[\theta(\mathbf{x})] = \beta\sum_{\mathbf{x},\mu}\cos(\Delta_\mu\theta(\mathbf{x}) - \alpha_\mu(\mathbf{x})) \tag{3.16}$$

$$Z_{XY}[\alpha(\mathbf{x})] = \int \mathcal{D}\theta\ e^{-S_{XY}[\theta(\mathbf{x})]}. \tag{3.17}$$

which is a frustrated XY model and $\beta = \frac{2a}{3\kappa}\mu\zeta$, $\Delta_\mu\theta(\mathbf{x}) = \theta(\mathbf{x}+\hat{\mu}) - \theta(\mathbf{x})$. The frustration in question is localized in the surface whose boundary is the Wilson loop, now the minimal surface $\mathcal{S}_m(\mathcal{C})$ is chosen such that,

$$\alpha_\mu(\mathbf{x}) = \begin{cases} \frac{2\pi}{N}k & \text{If the line segment in lattice point } \mathbf{x} \text{ towards } \mathbf{x}+\hat{\mu} \\ & \text{pierces } \mathcal{S}_m(\mathcal{C}) \\ 0 & \text{otherwise} \end{cases}. \tag{3.18}$$

In this context Wilson loop averages become

$$\langle\mathcal{W}(\mathcal{C})\rangle = \frac{Z_{XY}[\alpha_\mu(\mathbf{x})]}{Z_{XY}[0]}. \tag{3.19}$$

where $Z_{XY}[\alpha_\mu(\mathbf{x})]$ is the partition function obtained from the action (3.16). One can see a pictorial representation of the frustration in fig. 14.

The unfrustrated XY model arises when one studies superfluid ^{4}He [44] and when one analyses magnetic systems with Hamiltonians that have planar interaction. It is known that this model suffers a second order phase transition at critical coupling $\beta_c \approx 0.454 \approx 1/2.203$ and was extensively studied in ref. [34], where its critical exponents are also obtained.

Another feature that characterizes this phase transition is the fact that the correlation length diverges at the critical point [34]. Thus, any other physical scale becomes negligible and hence the continuum properties of the model are recovered. A more complete argument to this will be given in the next section. As the frustration appears only near the minimal Wilson surface, it is expected that this does not change the critical

[1] They ignore density fluctuations around v_0 because vortex interactions are considered to be sufficiently weak hence these fluctuations are strongly limited by the potential, nonetheless the Goldstein θ oscilations are not at all.

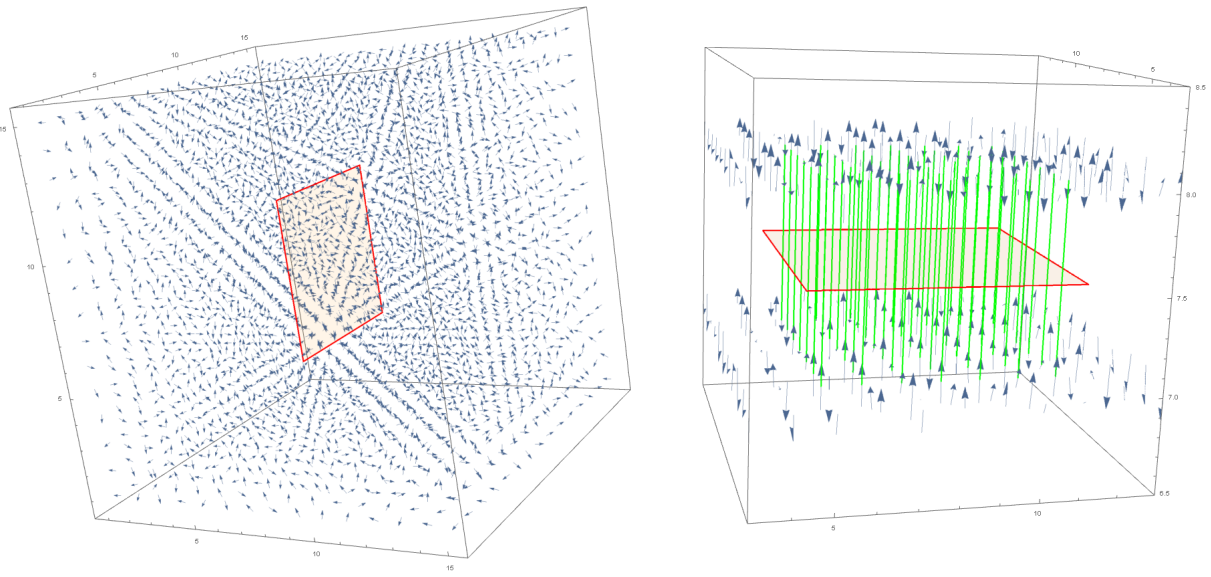

Figure 14 – (Left) A frustrated XY model configuration with $1/\beta = T = 2.5$, the red square represents the Wilson loop. (Right) Zoom in close to the loop, in green those links which are frustrated.

behavior drastically. So, the $\langle \mathcal{W}(\mathcal{C}) \rangle$ averages are to be taken near the critical point of the unfrustrated XY-model.

Before going any further, it is relevant to integrate over the θ's in (3.17). To this end one refers first to the Fourier decomposition

$$e^{\beta \cos\theta} = \sum_{f \in \mathbb{Z}} I_f(\beta) e^{if\theta}, \tag{3.20}$$

where $I_f(\beta)$ is the modified Bessel function of the first kind. This transform is to be performed to each θ of the action, thus leading to

$$Z_{XY}[\alpha_\mu(\mathbf{x})] = I_0(\beta)^{3M} \sum_{\{f_\mu(\mathbf{x})\}} \prod_{\mathbf{x},\mu} \frac{I_{f_\mu(\mathbf{x})}(\beta)}{I_0(\beta)} e^{-i f_\mu(\mathbf{x}) \alpha_\mu(\mathbf{x})}, \tag{3.21}$$

which introduces the constraint

$$\Delta_{(-\mu)} f_\mu(\mathbf{x}) = 0, \tag{3.22}$$

known as the *non-backtracking* condition, or the lattice equivalent of a divergenceless vector field. Interpreting f_μ as currents, the $f_\mu(\mathbf{x} - \mu)$ being currents that enter point $\mathbf{x}$, whereas $f_\mu(\mathbf{x})$ leave the same point, the above equation states that all lattice sites have no *liquid* incoming or outgoing currents. Thus characteristic configurations of f_μ are those that either are closed or percolating [44]. This is then how the effective XY-model encodes one of the basic original ensemble properties.

3.3 The Continuum Limit and the Critical Coupling

It was claimed in the previous section that continuum properties arise if averages of the lattice model are taken near the critical coupling of the lattice action. This is a very subtle claim, and it stems from the spontaneous breaking of the continuous $U(1)$ symmetry in the lagrangian in (3.10), that engenders huge quantum fluctuations that prohibit a perturbative analysis and a simple continuum limit.

To shed some light onto the subject, one may and consider some general arguments [64]. One may extract the spectrum of a field theory by analyzing the large Euclidean time behavior of correlation functions of the suitable operators, as discussed in the end of section A.2. The low-lying states of this spectrum are associated with the biggest correlation lengths of this theory.

If these states, say e.g., a mass gap m, are to be physical, then the lattice-unit measure of this quantity, $\hat{m} = ma$, where a is the lattice spacing, must go to zero when the continuum limit is taken. Therefore, the associated correlation function in lattice units must diverge. This implies then that the continuum limit of the quantum field theory is accomplished when the coupling of the lattice action (3.16) is critical. In the case of the XY model, the behavior of the correlation length is $\xi(\beta) \sim |\beta_c - \beta|^{-\nu}$ as one approaches β_c from values that are smaller than it, $\beta \to \beta_c^-$, ν is about 0.67 [22, 34]. That then is how the criticality should be approached.

3.4 Obtaining the Wilson loop behavior from the Effective XY-model

As discussed in the introduction, depending on the phase of the gauge theory, averages of Wilson loops must give an area or a perimeter law. A question that remains then is: how this property arises from the effective model obtained in section ?

The way chosen in ref. [58] to answer this is to first take an approximation whose validity comes from the fact that, near the critical point, models within the same universality class have practically the same behavior. Using the fact that the Villain model is within the same universality class of the unfrustrated XY-model, and that its frustrated version is to have the same critical behavior, one might take the Villain prescription [2] [44] to the

[2] This prescription implements the approximation of the exponential of the cosine by infinite gaussian functions centered in its maxima which is valid for sufficiently big β, and this is the case for the critical temperature of the XY model.

frustrated case,

$$e^{\beta\cos\alpha} \mapsto R_V(\beta)\sum_{n\in\mathbb{Z}} e^{-\frac{\beta_V}{2}(\alpha-2\pi n)^2} \text{ where} \tag{3.23}$$

$$R_V(\beta) = \sqrt{2\pi\beta_V} I_0(\beta), \text{ and } \beta_V \text{ satisfies} \tag{3.24}$$

$$-\frac{1}{2\beta_V(\beta)} = \ln\left(\frac{I_1(\beta)}{I_0(\beta)}\right), \text{ so that} \tag{3.25}$$

$$Z_{XY}[\alpha_\mu] \approx Z_V[\alpha_\mu] = (R_V(\beta))^{3M}\prod_{\mathbf{x}}\int_0^{2\pi}\frac{d\theta(\mathbf{x})}{2\pi}\sum_{\{n_\mu(\mathbf{x})\}} e^{-\frac{\beta_V}{2}(\Delta_\mu\theta(\mathbf{x})-\alpha_\mu(\mathbf{x})-2\pi n_\mu(\mathbf{x}))^2}. \tag{3.26}$$

They then used a auxiliary field f_μ to linearize the Gaussian term in (3.26) and after it the Poisson summation formula,

$$\sum_{n\in\mathbb{Z}} e^{2\pi i n f} = \sum_{n\in\mathbb{Z}} \delta(f-n), \tag{3.27}$$

so that the f's become restricted to integer values, thus if one further performs a lattice integration by parts [3], and integrating in the θ's and using both (3.24) and (3.25),

$$Z_V = I_0(\beta)^{3M}\sum_{\{f_\mu(\mathbf{x})\}}\prod_{\mathbf{x},\mu}\left(\frac{I_1(\beta)}{I_0(\beta)}\right)^{f_\mu^2(\mathbf{x})} e^{-i\sum_{\mathbf{x}} f_\mu\alpha_\mu(\mathbf{x})}, \tag{3.28}$$

where the constraint $\Delta_{(-\mu)}f_\mu = 0$ arises again. By comparing (3.21) and the equation above, that the Villain approximation in this case can also amount to the prescription

$$\frac{I_{f_\mu(\mathbf{x})}(\beta)}{I_0(\beta)} \mapsto \left(\frac{I_1(\beta)}{I_0(\beta)}\right)^{f_\mu^2(\mathbf{x})}, \tag{3.29}$$

that will be relevant in the next lines to motivate a approximation later.

[3] $\sum_{\mathbf{x},\mu} f_\mu(\mathbf{x})\Delta_\mu\theta(\mathbf{x}) = -\sum_{\mathbf{x},\mu}\theta(\mathbf{x})\Delta_{(-\mu)}f_\mu(\mathbf{x})$

3.4.1 Perimeter Law

Later, they define that the minimal surface is perpendicular to the $\hat{\mathbf{1}}$ axis, so that $\mathcal{S}_m(\mathcal{C})$ is placed between the links $\mathbf{z}$ and $\mathbf{z}+\hat{\mathbf{1}}$. A perimeter law can be obtained by considering β to be small. In this regime, surprisingly the XY and the Villain model still have a similar behavior [44], in such a way that the first contribution in this high temperature expansion come from loops of length 4 in both cases.

Now, those plaquette loops that are not linked with the minimal surface are already excluded and plaquettes that link with it twice have $\sum_{\{\mathbf{z}\}} f_\mu = 0$, where $\{\mathbf{z}\}$ denotes the links that pierce $\mathcal{S}_m(\mathcal{C})$. From that, one deduces that the only plaquettes that contribute are those that go through links on both sides of the surface, one piercing it and the other not, thus implying that they are located only along the perimeter of $\mathcal{C}$. If there are M_P links piercing $\mathcal{S}_m(\mathcal{C})$ near the perimeter,

$$Z_V[\alpha_\mu(\mathbf{x})] \approx I_0(\beta)^{3M}\left(\frac{I_1(\beta)}{I_0(\beta)}\right)^4 [(6M-2M_P)+2M_P\cos\frac{2\pi}{N}] \tag{3.30}$$

Where $(6M-2M_P)$ is the number of links that do not pierce the surface near the perimeter. This leads to

$$\langle\mathcal{W}(\mathcal{C})\rangle \approx 1-\frac{2M_P}{3M}\sin^2\left(\frac{2\pi}{N}\right), \tag{3.31}$$

so that in the large N limit,

$$\langle\mathcal{W}(\mathcal{C})\rangle \approx e^{-\kappa P}, \text{so that} \tag{3.32}$$

$$\kappa = \frac{2}{3a}\frac{1}{M}\sin^2\left(\frac{2\pi}{N}\right) \tag{3.33}$$

where $P = M_P a$ is the perimeter of $\mathcal{C}$.

3.4.2 Area Law

In the next steps, $\{0\}$ denotes configurations where all $f_\mu = 0$ and $\{F_0\}$ any other nontrivial configurations, thus $\{f_\mu(x)\} = \{0\}\bigcup\{F_0\}$. Then, the authors defined

$$G_{\{A\}}(\alpha_\mu) = \sum_{\{A\}}\prod_{\mathbf{x},\mu}\left(\frac{I_1(\beta)}{I_0(\beta)}\right)^{f_\mu^2(\mathbf{x})} e^{-i\sum_{\mathbf{x}} f_\mu\alpha_\mu(\mathbf{x})}, \tag{3.34}$$

for any set $\{A\}\subseteq\{F_0\}$. Thus from (3.19) and (3.28),

$$\langle\mathcal{W}(\mathcal{C})\rangle \approx \frac{1+G_{\{F_0\}}(\alpha_\mu)}{1+G_{\{0\}}(0)}. \tag{3.35}$$

Now, writting $\{F_0\} = \{A_0\}\bigcup\{F_1\}\bigcup\{R_0\}$, where the three sets on the right-hand side denote respectively: the set of f_μ's such that none of the loops pierce $\mathcal{S}_m(\mathcal{C})$; the set where

the $\mathcal{S}_m(\mathcal{C})$ is pierced once; and the remaining configurations, where there might be both types of loops of the other two types, hence

$$G_{\{F_0\}} = G_{\{A_0\}} + G_{\{F_1\}} + G_{\{R_0\}}. \tag{3.36}$$

One fact to be stressed now is that it is known from superfluid studies [44] that, near the critical point, small loops with big fluxes f_μ are almost irrelevant in comparison with big loops with unitary flux. In other words, configurations $\{F_0\}'$ such that $f_\mu = \pm 1$ or 0. For these small fluxes the map (3.29) is exact.

Afterwards, the authors perform the following stream of steps:

- they argue that loops that meet at a single loop give an irrelevant contribution, each term on eq. (3.36) is substituted by their primed counterparts;
- $f_\mu^2(x) \mapsto |f_\mu(\mathbf{x})|$ for $f_\mu = \pm 1$ or 0;
- the main contribution to configurations in $\{R_0\}'$ is argued to come from $\{A_0\}' \times \{F_1\}'$, so that $G_{\{R_0\}'} \approx G_{\{A_0\}'} G_{\{B_1\}'}$ and $1 + G_{\{F_0\}} \approx (1 + G_{\{A_0\}'})(1 + G_{\{F_1\}'})$;
- Then $\{F_1\}$ is partitioned as $\{F_1\} = \{A_1\}' \bigcup \{F_2\}' \bigcup \{R_1\}'$ where the latter sets represent respectively the set of loops that pierce $\mathcal{S}_m(\mathcal{C})$ once; the set where individual loops intersect $\mathcal{S}_m(\mathcal{C})$ at least twice; and the set formed by combinations with single occupation;
- After that they write $\{A_1\}' = \{\mathbf{z}_1\} \times \{\mathbf{z}_2\} \times ... \times \{\mathbf{z}_{A/a^2}\}$. Each factor in this equation represents a set of vortices that intersect $\mathcal{S}_m(\mathcal{C})$ at site $\mathbf{z}_i$ and then

$$1 + G_{\{A_1\}'}(\alpha_\mu) \approx \prod_{\{\mathbf{y}\}} (1 + G_{\{\mathbf{z}\}'}(\alpha_\mu)) \tag{3.37}$$

Remembering that for every vortex loop with one orientation there is another with an opposite one, they are able to deduce that

$$G_{\{\mathbf{y}\}'} = \gamma_{\{\mathbf{z}\}'} \cos\left(\frac{2\pi}{N} k\right) \tag{3.38}$$

$$\gamma_{\{\mathbf{z}\}'} = \sum_{\{\mathbf{z}\}'} e^{-\frac{1}{2\beta_V} \sum_{\mathbf{x},\mu} |f_\mu(\mathbf{x})|}. \tag{3.39}$$

ignoring the contribution from $G_{\{F_2\}'}$, they finally arrive at an area law,

$$\langle \mathcal{W}(\mathcal{C}) \rangle \approx e^{-\sigma A} \tag{3.40}$$

$$\sigma = -\frac{4\xi}{\beta_c^2} \ln\left(\frac{1 + \gamma \cos\left(\frac{2\pi}{N} k\right)}{1 + \gamma}\right) = -\frac{4\xi}{\beta_c^2} \ln\left(1 - \frac{2\gamma}{1 + \gamma} \sin^2\left(\frac{k\pi}{N}\right)\right) \tag{3.41}$$

where $A = M_A a^2$, M_A being the number of links that pierce $\mathcal{S}_m(\mathcal{C})$, and $\xi = (\mu\zeta/3\kappa)^2$.

One thing to be noted is that (3.40) can be cast into a form which amounts to the random vortex model [37]. So,

$$\langle \mathcal{W}(\mathcal{C}) \rangle \approx \prod_{\{\mathbf{z}\}} \left(\frac{1 + \gamma_{\{\mathbf{z}\}} \cos \frac{2\pi}{N}}{1 + \gamma_{\{\mathbf{z}\}}} \right) = \prod_{\{\mathbf{z}\}} (1 - 2p_{\{\mathbf{z}\}} + p_{\{\mathbf{z}\}} e^{i\frac{2\pi}{N}} + p_{\{\mathbf{z}\}} e^{-i\frac{2\pi}{N}}) \tag{3.42}$$

where it is identified that

$$p_{\{\mathbf{z}\}} = \frac{1}{2} \frac{\gamma_{\{\mathbf{z}\}}}{1 + \gamma_{\{\mathbf{z}\}}} \tag{3.43}$$

which reduces to (2.11) for $N = 2$ if it is identified that $p_{\{\mathbf{z}\}} \leftrightarrow \frac{1}{2} A/L^2$.

The result in eqs. (3.40) and (3.41) however, can not be the final word for $N > 2$, because then effects like branching, which will be discussed in another section, will have a significant contribution. One evidence to this statement is the fact that in the large N limit the string tension ratios for N-ality k is predicted to be

$$\frac{\sigma_k}{\sigma_1} \approx \frac{\sin^2 \frac{k\pi}{N}}{\sin^2 \frac{\pi}{N}} \tag{3.44}$$

which is not what is expected for Yang Mills, as it is not a Casimir nor a Sine-Law.

3.5 The Solid Angle Picture

Another way to notice that the main features of the partition function (3.17) can be captured without having necessarily the frustration described by (3.18), is to take again the high temperature expansion of the Boltzmann weight with a general $\alpha_\mu(\mathbf{x})$,

$$Z[\alpha_\mu(\mathbf{x})] = \int \mathcal{D}\theta \exp \left[\beta \sum_{\mathbf{x},\mu} \cos(\Delta_\mu \theta(\mathbf{x}) - \alpha_\mu(\mathbf{x})) \right] \tag{3.45}$$

$$= \int \mathcal{D}\theta \sum_n \frac{\beta^n}{n!} \left(\sum_{\mathbf{x},\mu} \cos(\Delta_\mu \theta(\mathbf{x}) - \alpha_\mu(\mathbf{x})) \right)^n . \tag{3.46}$$

if one is to perform further θ integrals above the following identities are important

$$\int_0^{2\pi} d\theta_i \ \cos(\theta_i - \theta_j) = 0 \tag{3.47}$$

$$\int_0^{2\pi} d\theta_i \ \cos(\theta_i - \theta_j) \cos(\theta_j - \theta_k) = \pi \cos(\theta_i - \theta_k) \tag{3.48}$$

$$\int_0^{2\pi} d\theta_i d\theta_j \int_0^{2\pi} \cos(\theta_i - \theta_j) \cos(\theta_i - \theta_j) = 2\pi^2 . \tag{3.49}$$

The first of these implies that if a cosine of one the θ's is left 'alone' in the integrals the whole term where it appears does not contribute. Combining this with (3.48) one may see that the there are terms that contribute to the partition function whose θ_i's are associated with closed curves, with higher order β (lower temperature) terms implying in bigger loops. This gives us a way to interpret center vortices in the effective XY model level.

The terms where eq. (3.49) is required are associated with loops with higher fluxes, but it was argued previously that they should not give a significant contribution to the partition function. Hence, (3.17) can be written as

$$Z[\alpha_\mu] \approx \sum_{n^\star} \pi^{n^\star} \frac{\beta^{n^\star}}{n^\star!} \cos\left(\sum_{\square} \alpha_\mu(\mathbf{x})\right). \tag{3.50}$$

Where $n^\star$ are the values of n for which is possible to have closed loops and $\square$ implements that fact that the sum must be so that $\mathbf{x}, \mu$ form closed loops.

Hence, the only information to which the partition function is sensitive is the circulation of the frustration, which gives us the option to 'dilute' the frustration, i.e. instead of having a frustration localized in those links that pierce $\mathcal{S}_m(\mathcal{C})$ we could put a frustration that has smaller local frustrations, but with the same sum as a result.

Thus all that is needed is a frustration function $\alpha_\mu(\mathbf{x})$ such that

$$\sum_{\square} \alpha_\mu(\mathbf{x}) = \frac{2\pi}{N} kw \tag{3.51}$$

When the loop $\square$ winds around the Wilson loop w times, which is the result when the frustration (3.18) is considered. With this picture in mind, we can formulate a Solid Angle Picture for the frustrated 3D-XY effective model. It is called this way because of the observation that

$$\oint_\ell dx_\mu \; \partial_\mu \chi_{\mathcal{C}} = 4\pi w \tag{3.52}$$

where $\chi_{\mathcal{C}}$ is solid angle subtended by the Wilson loop $\mathcal{C}$ when one is at a point of the curve ℓ. This last curve is such that it winds around $\mathcal{C}$ w times.

This result reflects the 'multi-valuedness' of the solid angle when one travels through a closed path ℓ that links $\mathcal{C}$. To make sense out of this, it is worth looking at how χ behaves as one travels through ℓ. To this end take fig. 15. There one sees a the loop from a plane perpendicular to it. ℓ is taken to be parallel to this observation plane.

As one travels from point (a) towards point (b), the solid angle varies continuously from $\chi \sim 0$, because (a) is near the plane that contains $\mathcal{C}$, to a value $\chi \leq 2\pi$, the equality being valid if (b)$\in \mathcal{S}_m(\mathcal{C}) \cap \ell$. Going from (b) to (c), the solid angle grows above 2π. And then as one gets closer (d), that is also near the plane that contains $\mathcal{C}$, but under it, $\chi \lesssim 4\pi$.

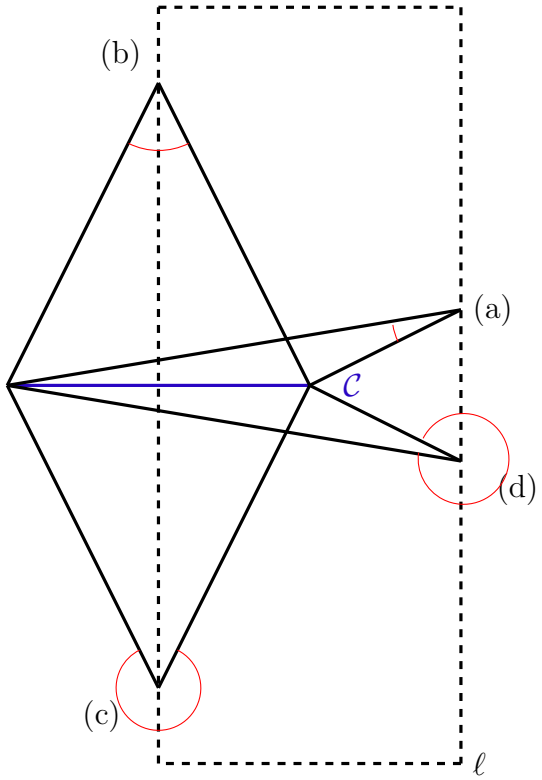

Figure 15 – Pictorial representation of the multivaluedness of the solid angle when one winds around the Wilson loop.

Then, following eq. (3.52), one is able to substitute J_μ in eq. (3.15) by

$$J_\mu^{\mathcal{C}}(x) = \frac{k}{2N}\partial_\mu \chi, \tag{3.53}$$

one is lead to the lattice frustration

$$\alpha_\mu(\mathbf{x}) = \int_{\mathcal{L}(\mathbf{x};\mu)} J_\nu^{\mathcal{C}} dx_\nu = \frac{k}{2N}[\chi(\mathbf{x}+\mu) - \chi(\mathbf{x})] = \frac{k}{2N}\Delta_\mu \chi(\mathbf{x}). \tag{3.54}$$

The main advantage of this picture is that one does not put a drastical area-related information in the model, so an Wilson loop area law arising in this context has a much more powerful significance. The 'dilution' implied in this picture is also advantageous in a numerical sense, because the method used to obtain Wilson loop averages gives more precise results if the two systems are not very different from each other (cf. section 4.4).

4 Monte Carlo methods

Given the theoretical motivation of this work, it is now time to develop the numerical methods used in the simulations to confirm them or not. It is standard to use Monte Carlo methods because they are the most suitable tool when one wants to perform multidimensional integrals, as in the evaluation of a partition function, for instance. This is because the parameter space (in the present case, $[0, 2\pi]^{L^3}$, where L^3 is the number of lattice sites) is better explored by random sampling than with a regular lattice, as the latter breaks the rotational symmetry of that space, so that some directions contain many points and others do not, whereas the former looks almost the same [45].

4.1 Importance Sampling and Metropolis Algorithm

Let $\mathcal{C}$ be a configuration of a system such as the unfrustrated XY-model, where $\mathcal{C} = \{\theta(x), \forall \mathbf{x} \in \text{Lattice}\}$, and $\mathcal{Q}$ a quantity that one wants to take equilibrium thermal averages [1] of,

$$\langle \mathcal{Q} \rangle = \frac{\int \mathcal{D}\theta \mathcal{Q}[\mathcal{C}] e^{-S[\mathcal{C}]}}{\int \mathcal{D}\theta e^{-S[\mathcal{C}]}}. \tag{4.1}$$

What the present method proposes to do is to reinterpret (4.1) as simple average,

$$\langle \mathcal{Q} \rangle \approx \frac{1}{N} \sum_{k=1}^{N} \mathcal{Q}[\mathcal{C}_k], \tag{4.2}$$

over configurations $\mathcal{C}_k$ chosen according to the equilibrium distribution

$$p_{eq}[\mathcal{C}] = \frac{e^{-S[\mathcal{C}]}}{\int \mathcal{D}\theta e^{-S[\mathcal{C}]}}. \tag{4.3}$$

in such a way that a computer can perform the task.

To such end, one starts with a arbitrary configuration, and from it build a stochastic process that takes the system to the equilibrium distribution (4.3). This process is built so that any new configuration $\mathcal{C}_{j+1}$ depends on its previous one, $\mathcal{C}_j$, characterizing then a so-called *Markov chain*.

To compute the averages (4.1) one then exploits a fundamental aspect of equilibrium configurations which is the fact that the probability of going from one configuration $\mathcal{C}_1^{eq}$ to another configuration $\mathcal{C}_2^{eq}$, when taking $\mathcal{C}_1^{eq} \mapsto \mathcal{C}_2^{eq}$ must be equal to the probability of the

[1] As in the present case the Euclidean action plays the role of the energy, the concepts of quantum and thermal fluctuations are almost the same. This enables one to call $S[\mathcal{C}]$ interchangeably an action or an energy.

inverse process to happen, namely $\mathcal{C}_2^{eq} \mapsto \mathcal{C}_1^{eq}$. This condition can be met if the so-called *detailed balance* is satisfied [11], thus

$$p_{eq}(\mathcal{C}_1^{eq})T(\mathcal{C}_1^{eq}|\mathcal{C}_2^{eq}) = p_{eq}(\mathcal{C}_2^{eq})T(\mathcal{C}_2^{eq}|\mathcal{C}_1^{eq}) \tag{4.4}$$

where $T(\mathcal{C}_1^{eq}|\mathcal{C}_2^{eq})$ is the transition probability from configuration $\mathcal{C}_1^{eq}$ to $\mathcal{C}_2^{eq}$. A explicit form to build a process that leads the system to (4.4) consists in a convenient choice of $T(\mathcal{C}_k|\mathcal{C}_{k+1})$ to be applied in the k-th step in the Markov chain. A choice was proposed in the seminal paper ref. [54]: the famous *Metropolis algorithm*. The procedure is the following: let $T(\mathcal{C}_k|\mathcal{C}_{k+1})$ be decomposed as

$$T(\mathcal{C}_k|\mathcal{C}_{k+1}) = g(\mathcal{C}_k|\mathcal{C}_{k+1})A(\mathcal{C}_k|\mathcal{C}_{k+1}) \ , \tag{4.5}$$

where $g(\mathcal{X}|\mathcal{Y})$ is the probability of proposing configuration $\mathcal{Y}$ given that the system was in $\mathcal{X}$ previously and $A(\mathcal{X}|\mathcal{Y})$ is the probability of accepting $\mathcal{Y}$ given that the system was in $\mathcal{X}$. Then one proceeds with the following:

(i) Consider a trial configuration, $\mathcal{C}_{try}$, chosen randomly according to the above mentioned distribution, $g(\mathcal{C}_k|\mathcal{C}_{try})$. In the present context of an XY-model, this is equivalent to change a bit the configuration of the θ angles. In general one changes a single θ at a time.

(ii) If the configuration $\mathcal{C}_{try}$ has action (energy) $S[\mathcal{C}_{try}]$ smaller than that of $\mathcal{C}_k$, then $\mathcal{C}_{try}$ is immediately accepted as a new configuration of the system, thus $\mathcal{C}_{k+1} \leftarrow \mathcal{C}_{try}$ and one returns to item (i);

(iii) Else, if the configuration has an value of action (energy) bigger than $\mathcal{C}_k$, then the trial configuration $\mathcal{C}_{try}$ is accepted with a probability

$$q(\mathcal{C}_{try}, \mathcal{C}_k) = \frac{g(\mathcal{C}_k|\mathcal{C}_{try})}{g(\mathcal{C}_{try}|\mathcal{C}_k)} \frac{p(\mathcal{C}_{try})}{p(\mathcal{C}_k)}. \tag{4.6}$$

In general one chooses $g(\mathcal{C}_{try}|\mathcal{C}_k) = g(\mathcal{C}_k|\mathcal{C}_{try})$, thus $q(\mathcal{C}_{try}, \mathcal{C}_k) = e^{-\Delta S}$, $\Delta S = S[\mathcal{C}_{try}] - S[\mathcal{C}_k]$. Then one goes back to item (i). This process is repeated a suitably number of times so that condition (4.4) is satisfactorily met.

In this fashion, the steps above imply that

$$T(\mathcal{C}_k|\mathcal{C}_{k+1}) \propto A(\mathcal{C}_k|\mathcal{C}_{k+1}) = \min\{1, q(\mathcal{C}_{k+1}, \mathcal{C}_k)\} \ , \tag{4.7}$$

thus suppose that one performs N_m "measuments" of $\mathcal{Q}$ and discards the first N_d states that are out of equilibrium (this will be more precisely defined latter), and using the following $N_{eq} = N_m - N_d$ states, we might have an estimate of the equilibrium average (4.1),

$$\langle \mathcal{Q} \rangle \approx \frac{1}{N_{eq}} \sum_{j=1}^{N_{eq}} \mathcal{Q}(\mathcal{C}_{N_d+j}) \ . \tag{4.8}$$

In practice, to better results it is convenient to take multiple updates between each term in the sum (4.8) instead of only one. In fig. 16 the Metropolis algorithm is summarized pictorially.

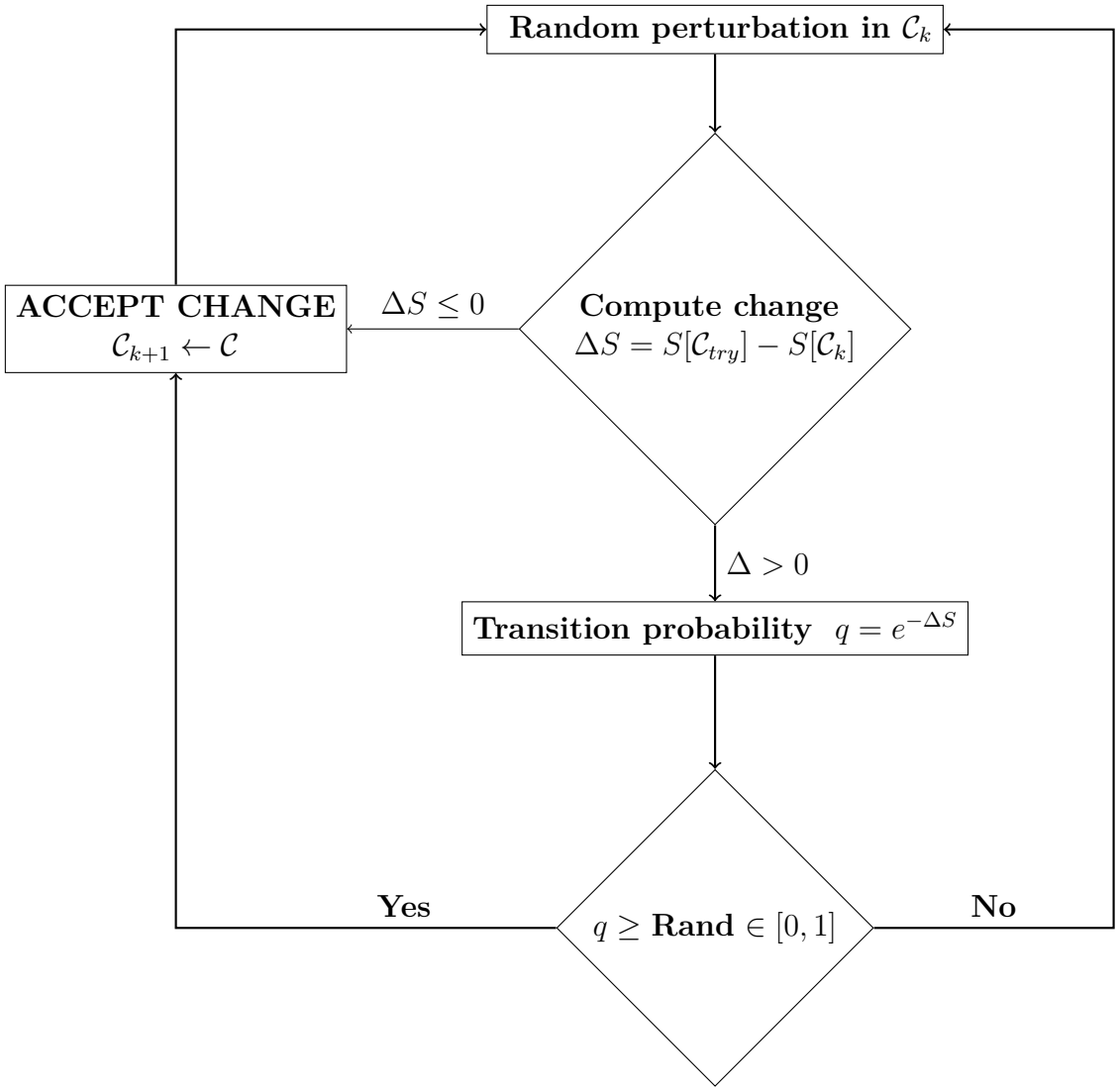

Figure 16 – Metropolis Algorithm's Pictorial Summary. Adapted from ref. [40].

4.2 The Equilibrium

Once the update algorithm is set, two questions of utmost importance remain: what states are to be considered in the averages (4.8)? How many updates one may perform between two 'measurements'? Giving cautious answers to these questions is essential to obtain good results.

In this fashion, suppose one has made N_m Monte Carlo-like observations of a quantity $\mathcal{Q}$, thus obtaining the time series $\{q_1, q_2, ..., q_{N_m}\}$. It is possible to consider that each of these observations is associated with a random variable Q_k, with the restriction that each of these variables are obtained from distributions (that can be the equilibrium one) which have the same average and the same dispersion, so that

$$\langle Q_k \rangle = \langle \mathcal{Q} \rangle \quad \text{e} \quad \sigma^2_{Q_k} = \langle (Q_k - \langle Q_k \rangle)^2 \rangle = \sigma^2_{\mathcal{Q}} \quad k = 1, ..., N_m. \tag{4.9}$$

One then is interested in estimating $\langle \mathcal{Q} \rangle$. A way to do this is to take

$$\bar{Q} = \frac{1}{N_m} \sum_{k=1}^{N_m} Q_k. \tag{4.10}$$

Hence

$$\bar{\sigma}^2 = \frac{1}{N-1} \sum_{k=1}^{N_m} (Q_k - \bar{Q})^2 \tag{4.11}$$

is an estimator of the error of $\bar{Q}$, once the latter is itself a random variable, as this changes if one reruns the algorithm with different random numbers. Then, variance of $\bar{Q}$ is

$$\begin{aligned} \sigma^2_{\bar{Q}} &= \langle (\bar{Q} - \langle \bar{Q} \rangle)^2 \rangle = \left\langle \left(\frac{1}{N_m} \sum_{k=1}^{N_m} (Q_k - \langle \bar{Q} \rangle) \right)^2 \right\rangle \\ &= \frac{1}{N_m} (\langle \mathcal{Q}^2 \rangle - \langle \mathcal{Q} \rangle^2) + \frac{2}{N_m^2} \sum_{n>k} (\langle Q_k Q_n \rangle - \langle \mathcal{Q} \rangle^2). \end{aligned} \tag{4.12}$$

For uncorrelated random variables, one has $\langle Q_k Q_n \rangle = \langle Q_k \rangle \langle Q_n \rangle = \langle \mathcal{Q} \rangle^2$. Along these lines,

$$\sigma_{\bar{Q}} = \frac{\sigma_{\mathcal{Q}}}{\sqrt{N_m}} \tag{4.13}$$

As follows, the error on the average (4.10) diminishes with the data number, which is a well-known result. Notwithstanding, in a simulation based on a Markov Chain, where each configuration depends on the anterior, there is a chance that there is correlation in the random variables $\{Q_1, Q_2, ..., Q_{N_m}\}$. This fact makes the *auto-correlation function*

$$\phi(Q_k, Q_{k+t}) = \langle Q_k Q_{k+t} \rangle - \langle Q_k \rangle \langle Q_{k+t} \rangle \tag{4.14}$$

to be nonzero. If $t = 0$ (4.14) reduces to $\sigma^2_{Q_k}$. So, to a separation t long enough, one expects that ϕ vanishes. Hence one defines the *relaxation function*

$$\Phi_Q(t) = \frac{\phi(Q_k, Q_{k+t})}{\phi(Q_k, Q_k)}. \tag{4.15}$$

For a Markov chain in equilibrium, this function should only depend on the separation t. Assuming that the evanescence of Φ occurs in timescale τ_Q much smaller than the total observation time, it is possible to estimate it through [2]

$$\tau_Q = \delta t \sum_{t=1}^{\infty} |\Phi_Q(t)| \tag{4.16}$$

Where δt is the 'time' between two successive measurements. Then the dispersion (4.12) becomes,

$$\begin{aligned} \sigma^2_{\bar{Q}} &= \frac{1}{N_m}(\langle \mathcal{Q}^2 \rangle - \langle \mathcal{Q} \rangle^2) + \frac{2}{N_m^2} \sum_{k=1}^{N_m} \sum_{t=1}^{N_m - t} (\langle Q_k Q_{k+t} \rangle - \langle \mathcal{Q} \rangle^2) \\ &= \frac{1}{N_m}(\langle \mathcal{Q}^2 \rangle - \langle \mathcal{Q} \rangle^2) \left(1 + 2 \sum_{t=1}^{N_m} \left(1 - \frac{t}{N_m} \right) \Phi_Q(t) \right). \end{aligned} \tag{4.17}$$

As $\Phi_Q(t)$ is only nonzero during a time $\tau_Q << N_m$ and N_m is a big number[3],

$$\sigma^2_{\bar{Q}} \approx \frac{1}{N_m}(\langle \mathcal{Q}^2 \rangle - \langle \mathcal{Q} \rangle^2) \left(1 + \frac{2\tau_{\bar{Q}}}{\delta t} \right). \tag{4.18}$$

In a broad sense, $\tau_{\bar{Q}}$ is significantly bigger than δt, if one further identifies that $\tau_{\text{obs}} = N_m \delta t$ is the total observation 'time' of the quantity $\mathcal{Q}$

$$\sigma_{\bar{Q}} \approx \sqrt{\frac{2\tau_{\bar{Q}}}{\tau_{\text{obs}}}} \sigma_{\mathcal{Q}}. \tag{4.19}$$

that is independent of δt, due to fact that if one redefines δt to increase the number of measurements, the relaxation time will grow by the same proportion so that the estimate is unaltered. Another thing to notice is that the ratio between $\sigma_{\bar{Q}}$ in eq. (4.19) and the one in (4.13) is $\sqrt{2\tau_{\bar{Q}}/\delta t}$, so that estimates of the error can be greatly enhanced as the relaxation time increases if these transient states are considered.

Along these lines, a notion of equilibrium is to take reasonably big multiple of τ as a interval to perform the averages, according to the precision needed and the resources available. This may be 5τ, 10τ or even $10^4\tau$ [32]. For those simulations onto which one takes averages of many quantities $\{\mathcal{Q}_k\}$, one acknowledges the highest of correlation time as being the one to define equilibrium. In general, to systems that suffer from second order phase transitions, as the XY-model does [34], the quantity to be chosen is the order parameter itself [11].

One issue with the present idea of equilibrium in terms of a relaxation time occurs near phase transitions, where the so-called *critical slowing down* takes place. This consists in the fact that time actually diverges in the thermodynamical limit. It occurs due to fact that τ apart from depending on the update algorithm, it also depends on the parameters of the system considered.

[2] It is sometimes better to perform a fit to the autocorrelation as a function of Monte Carlo time, as the equation below yields unrealsitic results.

[3] In this work, one uses $N_m \sim 10^5$

It commonly happens that $\tau \propto \xi^z$ [11], where z depends on the update scheme and ξ is the correlation length of the system, and this quantity is known to have a singular behavior near the critical temperature $\xi \propto |1 - T/T_c|^{-\nu}$. Taking finite lattice effects into account, the singularity is smoothed out and $\tau \propto L^z$, with L being the cubic lattice length. Thus the associated errors scale as $\sigma \propto L^\eta/\tau_{\text{obs}}$.

In case one wants to significantly increase the lattice size, one should also be aware that it will be necessary to increase the observation time so that the errors do not increase prohibitively. This problem is also seen in Lattice QCD simulations. Another procedure to avoid the error enhancing seen in eq. (4.19) is to simply ignore the transient states and only take averages at Monte Carlo times that are much bigger than the relaxation time of the order parameter. In this case, the traditional average root mean square (4.13) is still a good error estimator.

A possible solution to the problem of critical slowing down, for spin systems, just like the XY-model, is to use the so-called cluster or Wolff algorithm [66,71,72]. In short, in this procedure the Monte Carlo updates change chunks of the system under consideration (the clusters) all at once. For instance, in the Ising model one starts with a random point in space, which is the seed for the cluster, and then one searches in its first neighbours sites with the same sign. Those that pass the test are included in the cluster and then their first neighbours are analyzed. The procedure continues until no new points are added. Then, all sites in the cluster are updated.

4.3 Binder fourth-order Cumulant Method

As it was already cited in section 4.2, the three dimensional XY model suffers a second order phase transition at a certain critical coupling β_c or temperature $1/\beta_c$. A possible way to calculate this quantity is to perform what is called a finite scaling analysis of certain quantities. One of such quantities is the so-called fourth-order cumulant

$$U_L = 1 - \frac{1}{3}\frac{\langle s^4 \rangle_L}{\langle s^2 \rangle_L^2} \tag{4.20}$$

where $\langle s^n \rangle_L$ is the average of the n-th power of the order parameter, in our case, the magnetization

$$s = |\mathbf{M}|, \text{ where} \tag{4.21}$$

$$\mathbf{M} = \frac{1}{L^3}\sum_{\mathbf{x}} \mathbf{m}(\mathbf{x}) = \frac{1}{L^3}\sum_{\mathbf{x}} (\cos\theta(\mathbf{x}), \sin\theta(\mathbf{x})) \tag{4.22}$$

taken on a finite size cubic lattice of side L. This quantity has a peculiar behavior with respect to temperature T and correlation length ξ [10,11]:

(i) For $T > T_C$ and $L >> \xi$: $U_L \to 0$; $U_L \propto L^{-d}$

(*ii*) For $T < T_C$ and $L >> \xi$: $U_L = 2/3$ (Ising)

(*iii*) $L << \xi$: U_L barely varies with T and L; and it remains close to a universal value U^*

The method consists of plotting U_L as a function of temperature for many values of L and then finding the common intersection point between these curves, the T-axis value corresponding to the intersection is the critical temperature. This connects to item (*iii*) above, because it is expected that ξ diverges at the critical point. Below, a result obtained for the 3D-XY model without frustration

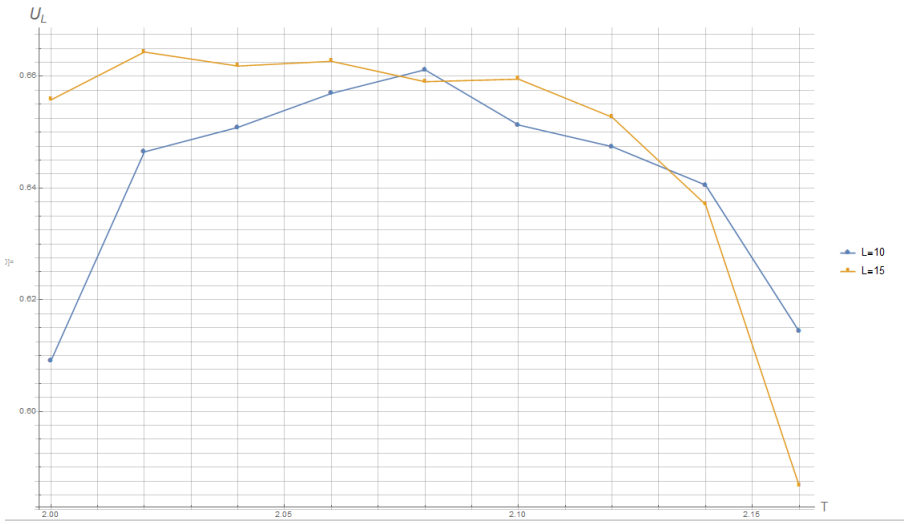

Figure 17 – Finite size scaling analysis for U_L with $L = 10$ and $L = 15$.

The intersection to be considered is the rightmost one at $T \approx 2.13 \pm 0.86$, because the other intersection does not represent a change on which function is bigger, and $U_{L=10}$ (blue curve) is bigger than $U_{L=15}$ (yellow curve) only in the neighborhood of such a point. Thus this pseudo-intersection could be accounted for when one considers the error bars as below.

The huge error bars can be explained if one analyzes the formula for U_L: it depends on the inverse of $\langle s^2 \rangle^2$ which is very small at high temperatures. Thus the obtained critical temperature is different from the most accepted value $T_c \approx 1/0.454 \approx 2.203$ by 3%.

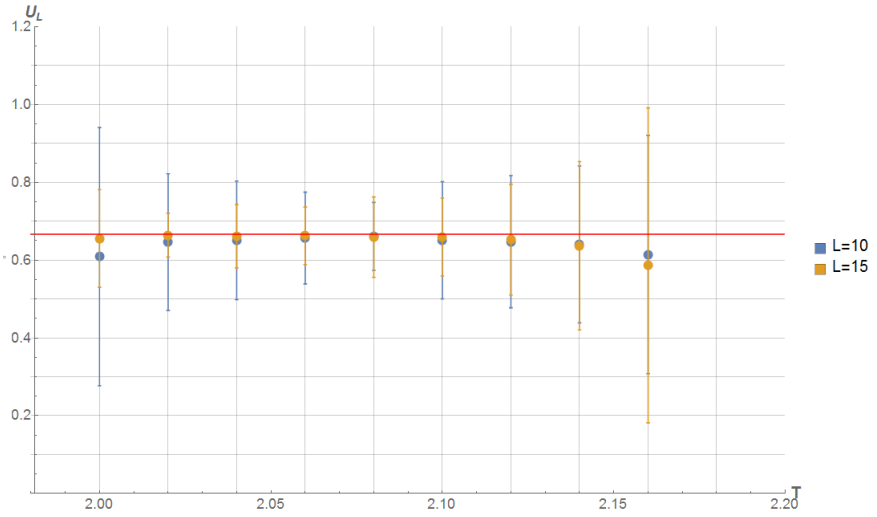

Figure 18 – Finite size scaling analysis for U_L with $L = 10$ and $L = 15$ with error bars and a bigger range of temperatures. The continuous line is the value $2/3$ which is expected for U_L at temperatures below the critical one.

4.4 The Partition Function ratio Method

From the end of section 3.2 the average of a Wilson loop $\langle \mathcal{W}(\mathcal{C}) \rangle$, in the context of the effective XY-model, becomes

$$\langle \mathcal{W}(\mathcal{C}) \rangle \approx \frac{Z_{XY}[\alpha_\mu(\mathbf{x})]}{Z_{XY}[0]} \tag{4.23}$$

where $Z_{XY}[\alpha_\mu(\mathbf{x})]$ ($Z_{XY}[0]$) is the partition function for the (un)frustrated 3D XY-Model.

One aspect of Monte-Carlo Metropolis-based simulations that becomes relevant now is that information about the exact value of the partition functions is lost, because the transition probabilities involved depend only on the ratio of ensemble probabilities, as one can see from (4.6), and, in general, it is difficult to obtain Z as its computations involve a wide range of numerical scales. The simplest things one can do is to calculate thermodynamical averages in equilibrium or to study the path towards equilibrium.

From thermodynamics, however, one knows the connection between the partition function and an extensive thermodynamical quantity known as Helmholtz free energy [65], the latter being proportional to the logaritmic measure of the former, thus

$$F = -k_B T \ln Z \tag{4.24}$$

$$F = E - TS \tag{4.25}$$

so, (4.23) reduces to

$$\langle \mathcal{W}(\mathcal{C}) \rangle \approx e^{-\beta(F_{XY}[\alpha_\mu(\mathbf{x})] - F_{XY}[0])} \tag{4.26}$$

Nevertheless, there is still a conundrum to be solved, because, as defined in (4.25) Helmholtz free energy depends on the energy, which can be rather easily measured on Monte Carlo

simulations, but it also depends on the entropy, which is not. There is a relation between energy and Helmholtz free energy, namely

$$E = -\left(\frac{\partial F}{\partial \beta}\right)_{\square,\square} \tag{4.27}$$

then

$$\ln\langle \mathcal{W}(\mathcal{C})\rangle \approx \int_0^\beta d\beta'(E_{XY}[\alpha_\mu(\mathbf{x})] - E_{XY}[0]). \tag{4.28}$$

but, as ref. [11] puts it, this is "a poor man's method" numerically, because it adds an extra difficulty: one must take an integral, which numerically means to sum over the integrand on very close points on the U vs β plan. Thus, one needs a reference temperature, $\beta \to 0$ is the most straightforward one as one expects that $Z_{XY,f}/Z_{XY,0} = 1 \Rightarrow \ln\langle \mathcal{W}(\mathcal{C})\rangle = 0$. But one might need to investigate temperatures up to $T = 2.203 \Rightarrow \beta = 0.454$ to see the behavior near the critical point which raises both the computational cost to evaluate $\langle \mathcal{W}(\mathcal{C})\rangle$ as well as systematic errors at high temperatures.

However, also in ref. [11] one finds that differences between Helmholtz free energies in two different systems with the same degrees of freedom can be calculated taking averages in only one of such systems, namely,

$$\langle \mathcal{W}(\mathcal{C})\rangle \approx e^{-\beta(F_{XY}[\alpha_\mu(\mathbf{x})]-F_{XY}[0])} = \langle e^{-\beta(E_{XY}[\alpha_\mu(\mathbf{x})]-E_{XY}[0])}\rangle_{XY,0} = \langle e^{-(S_{XY}[\alpha_\mu(\mathbf{x})]-S_{XY}[0])}\rangle_{XY,0}, \tag{4.29}$$

which is way simpler than performing integrals. In the last step, one reminded that the action plays the role of β times energy in the present context, and, from this section on, the discussions will follow the energy language.

An advantage of such method is that one can take averages on the simpler (unfrustrated) model (as denoted in the following by the $XY, 0$ subscript) and still grasp information about the more complicated (frustrated, denoted by XY, f) one. A demonstration to (4.29) is simple and it is as follows,

$$\frac{Z_{XY,f}}{Z_{XY,0}} = \frac{\int \mathcal{D}\theta(x)\ e^{-E_{XY,f}[\theta]}(1)}{\int \mathcal{D}\theta(x) e^{-E_{XY,0}[\theta]}} = \frac{\int \mathcal{D}\theta(x)\ e^{-E_{XY,f}[\theta]}(e^{E_{XY,0}[\theta]}.e^{-E_{XY,0}[\theta]})}{\int \mathcal{D}\theta(x) e^{-E_{XY,0}[\theta]}} \tag{4.30}$$

$$= \frac{\int \mathcal{D}\theta(x)\ e^{-(E_{XY,f}[\theta]-E_{XY,0}[\theta])}e^{-E_{XY,0}[\theta]}}{\int \mathcal{D}\theta(x) e^{-E_{XY,0}[\theta]}} = \langle e^{-\beta(E_{XY,f}-E_{XY,0})}\rangle_{XY,0}. \tag{4.31}$$

However, if the two systems under consideration have energies too different from one another, the average (4.29) is prohibitively small, so this method can also impractical, because it is exponentially supressed, this is called the *overlap problem*. This is not expected to happen between the XY-model and its minimal surface frustrated version, near the transition, as it is argued in ref. [58]. This might even be a problem, because in the high temperature regime, both systems have almost equal energies, so that the signal-to-noise ratio is very small.

Another perspective to the overlap problem stems from an alternative demonstration to (4.29). Namely, let A and B be two systems with two different Hamiltonians, $\mathcal{H}_A$ and $\mathcal{H}_B$, but with the same degrees of freedom; and $p_A(\Delta E)$ the probability that system A has a energy difference of $\Delta E = \mathcal{H}_B - \mathcal{H}_A$ with respect to system B, then

$$p_A(\Delta E) = \frac{1}{Z_A}\int_\Omega d\mathbf{x}\; e^{-\beta\mathcal{H}_A(\mathbf{x})}\;\delta(\mathcal{H}_B(\mathbf{x}) - \mathcal{H}_A(\mathbf{x}) - \Delta E). \tag{4.32}$$

Analogously,

$$p_B(\Delta E) = \frac{1}{Z_B}\int_\Omega d\mathbf{x}\; e^{-\beta\mathcal{H}_B(\mathbf{x})}\;\delta(\mathcal{H}_B(\mathbf{x}) - \mathcal{H}_A(\mathbf{x}) - \Delta E) \tag{4.33}$$

Using the Dirac delta in (4.33) ($\mathcal{H}_B = \mathcal{H}_A + \Delta E$)

$$\begin{aligned} p_B(\Delta E) &= \frac{1}{Z_B}e^{-\beta\Delta E}\int_\Omega d\mathbf{x}\; e^{-\beta\mathcal{H}_A(\mathbf{x})}\;\delta(\mathcal{H}_B(\mathbf{x}) - \mathcal{H}_A(\mathbf{x}) - \Delta E) \\ &= \frac{Z_A}{Z_B}p_A(\Delta E)e^{-\beta\Delta E} \\ &= e^{\beta(\Delta F - \Delta E)}p_A(\Delta E) \end{aligned} \tag{4.34}$$

Integrating in $\Delta E \in \mathbb{R}$

$$\int_{\mathbb{R}} p_B(\Delta E)\; d\Delta E = 1 = e^{\beta\Delta F}\int_{\mathbb{R}} e^{-\beta\Delta E}p_A(\Delta E)\; d\Delta E = e^{\beta\Delta F}\langle e^{-\beta\Delta E}\rangle_A \tag{4.35}$$

$$\frac{Z_B}{Z_A} = e^{-\beta\Delta F} = \langle e^{-\beta\Delta E}\rangle_A \qquad \text{Q.E.D.} \tag{4.36}$$

Substituting A by $XY, 0$ and B by XY, f one has (4.29). Hence, the overlap problem arises when the probability distributions $p_A(\Delta E)$ and $p_B(\Delta E)$ do not overlap enough [11], in this case, the method is not very useful.

If however two systems A, B under consideration are very different from each other, one method proposed in ref. [18] can work. It simply consists to take the ratio of partition functions and do a multiply-by-one trick, so that,

$$\frac{Z_B}{Z_A} = \frac{Z_1}{Z_A}\frac{Z_2}{Z_1}\cdots\frac{Z_B}{Z_{N_p}} = \langle e^{-\beta(E_1 - E_A)}\rangle_A\langle e^{-\beta(E_2 - E_1)}\rangle_1 \ldots \langle e^{-\beta(E_B - E_{N_p})}\rangle_{N_p} \tag{4.37}$$

where, $Z_1 \ldots Z_{N_p}$, are partition functions of N_p systems that are intermediate between system A and B. For example, if A and B are spin models exposed to very different values of magnetic field, these intermediate systems can be those which have intermediate values of magnetic field. This method is also used in ref. [62], in the context of section 2.2. Another possible solution to the overlap problem is to take *umbrella sampling*, this consists of a biased sampling that enhances the overlap between the above-cited probability distributions $p_A(\Delta E)$ and $p_B(\Delta E)$ [11].

5 Numerical Results

5.1 Remarks about the simulations

Before start showing the results some specific aspects of the present simulations must be said. Firstly, some of the preliminary (sec. 5.2) and the broad temperature Wilson loop simulations were made in Wofram's Mathematica Software. All of the other ones were made using the C language (`gcc` compiler), using `gnuplot` software to produce the fits to the functions needed [1].

Regarding the Monte Carlo updates, they were made by choosing one point in the lattice at random and then making $\theta \mapsto \theta + \epsilon$ `Rand`, where `Rand` $\in (-1, 1)$ is a random number [2], and ϵ was found by trial and error to be $\epsilon = 0.15$. As for the random number generator, in the simulations performed on Wolfram's Mathematica its native generator was used. In C, both the Linear Congruential Method and the Mersenne Twister were implemented. More details about these generators can be found in Appendix B. For almost all the results in this work, the latter generator was used.

For the quantities of interest, each "measure" is performed at every L^D updates, L being the lattice site, D is the number of dimensions of the lattice, $D = 3$ for this work. In other words, one Monte Carlo time is defined as the time needed to perform one update per lattice site. The lattice has periodic boundary conditions in all directions.

As the interest in this work is to take averages near the criticality, the initial configuration chosen is the one where each site has a random angle θ. This configuration is sometimes called "hot start" because in a sense this randomness is expected in the high temperature regime. A last remark to be made is that wherever the critical temperature is mentioned, the most accepted value of $T_c \approx 2.203$ should be understood.

[1] According to the documentation (available in `http://gnuplot.sourceforge.net/docs_4.2/node82.html`) it uses the Levenberg–Marquardt algorithm to solve the (non-)linear least square problem.

[2] Sometimes `Rand` $\in (0, 1)$ because it was seen to lead faster equilibrium at low temperatures.

5.2 Preliminary Results

5.2.1 Relaxation time

In section 4.2 it was seen that the relaxation time is a quantity of great importance when considering the errors in Monte Carlo simulations, hence, it is worth taking some time analyzing it in the case of the unfrustrated model which is where most of the simulations in this chapter were made. But first, in fig. 19 one can see the behavior of the magnetization with the number of Monte Carlo iterations (or Monte Carlo time).

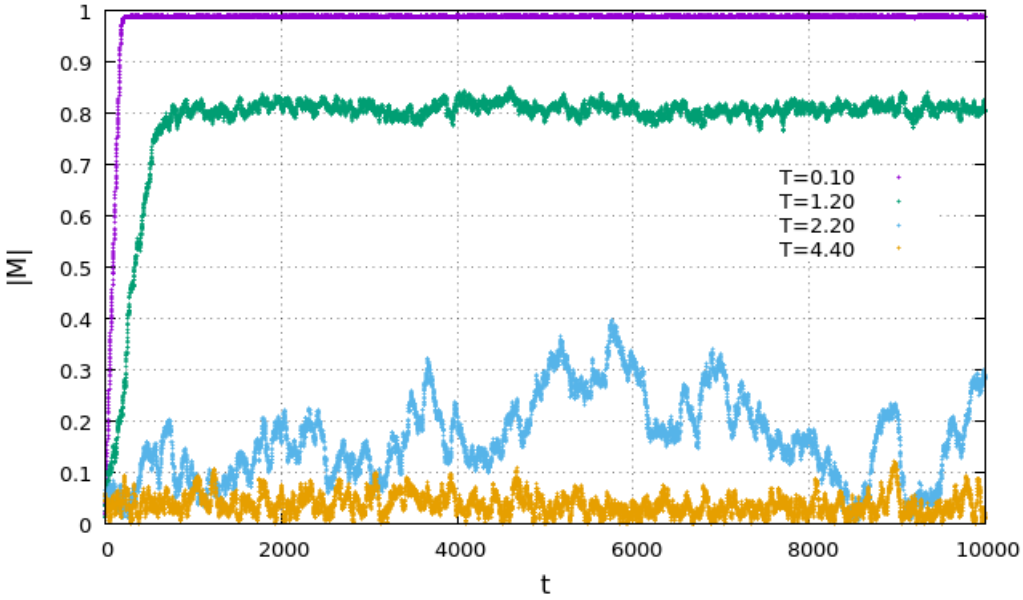

Figure 19 – Magnetization behavior with Monte Carlo time for $L = 11$.

Hence it can be seen that at low temperatures ($T = 0.10 \approx 0.045T_c$), the magnetization saturates quickly to a ~ 1 value and it does not oscilate much around it. Rising the temperature, but remaining in the broken symmetry phase ($T = 1.20 \approx 0.55T_c$), one can see that there is a value < 1 that the magnetization settles itself, but now it oscilates more and it takes more time to reach this regime. Near the critical temperature ($T = 2.20 \approx 0.998T_c$), it is not clear that $|\mathbf{M}|$ settles at all in this time window, and this quantity oscilates between a wide range of values, this pattern continues on to bigger times, thus evidencing the critical slowing down behavior. Finally, to temperatures above the critical one, the oscillations are less wild and the order parameter takes near zero values at all times.

To have a more quantitative picture on equilibrium it can be seen in fig. 20 the behavior of the autocorrelation function introduced in (4.15) with respect to the Monte Carlo time. In the present case to calculate it,

$$\phi_{|\mathbf{M}|}(t) = \sum_{t'=0}^{N_m - t} |\mathbf{M}(t+t')||\mathbf{M}(t')| - \frac{1}{N_m - t}\left(\sum_{t'=0}^{N_m - t} |\mathbf{M}(t+t')|\right)\left(\sum_{t'=0}^{N_m - t} |\mathbf{M}(t')|\right) \tag{5.1}$$

is used. Here it is defined that $\delta t = 1$, so that $t = N_m \delta t$ and $N_m >> \delta t$.

There it can be observed how the system behaves drastically different when it is exposed to temperatures near the critical. For all other temperatures, up to some fluctuations, the autocorrelation function decays from 1 (its value at zero time separation) to zero in a characteristic separation time. And for $T = 2.20 = 0.998 T_c$, it shows a oscilation in the interval $(-0.2, 0.3)$. Thus for these temperatures many other configurations are needed to reach more reliable results. A plot with a bigger range of time separations can be seen in fig. 21. For instance, regarding the results in the upcomming sections, the number of configurations ranges between 1.5 10^5 and 3.0 10^5.

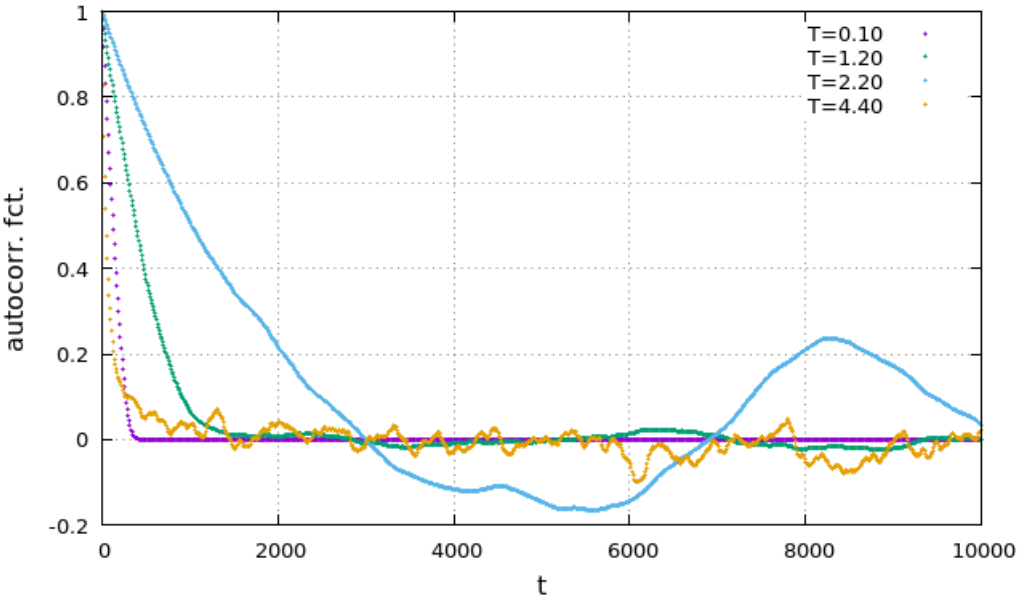

Figure 20 – The normalized autocorrelation function as a function of Monte Carlo time for $L = 11$.

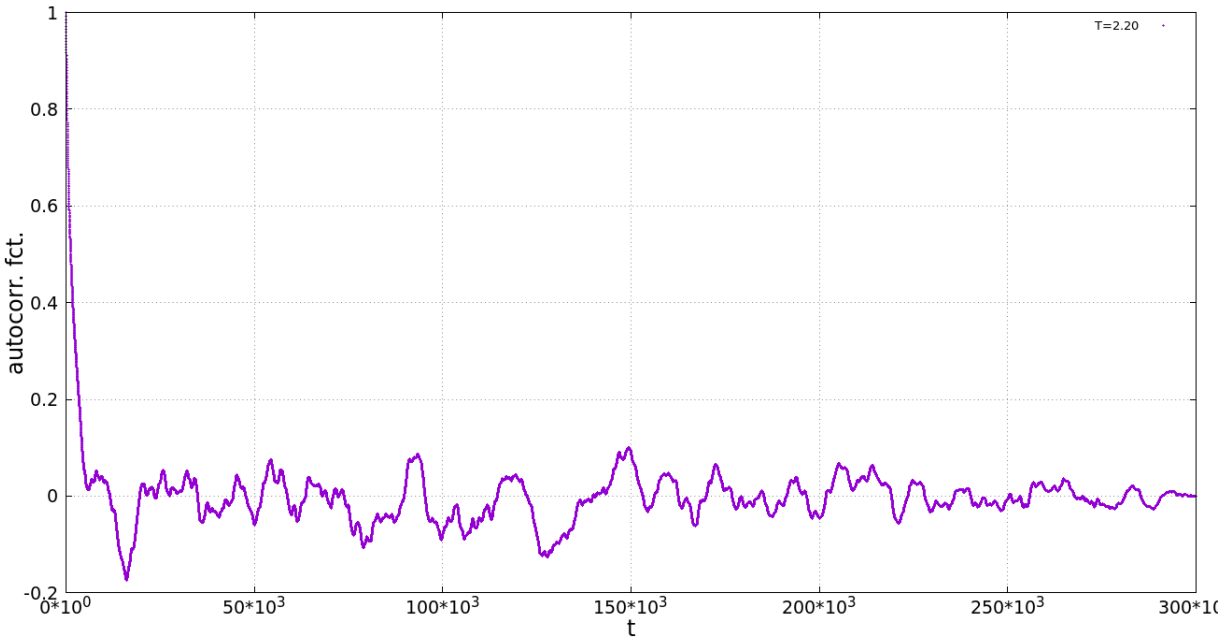

Figure 21 – Autocorrelation function dependence on the time separation for $L = 11$ and $T = 2.20 \approx 0.998 T_c$

Hence one may estimate the correlation time $\tau_{|\mathbf{M}|}$ for the magnetization $|\mathbf{M}|$ by fitting the graphs above with exponentials, as the use of (4.16) yields unrealistic results. The results are in table 1 together with the factor $\sqrt{2\tau}$ that corrects the traditional error estimate if transient states are considered. In fig. 22 the fits for a couple of temperatures can be seen.

$T/T_c(T)$	$\tau_{\lvert\mathbf{M}\rvert}$	$\sqrt{2\tau_{\lvert\mathbf{M}\rvert}}$
0.045 (0.10)	134 ± 1	16.36 ± 0.06
0.55 (1.20)	438 ± 5	29.6 ± 0.2
0.998 (2.20)	1406 ± 5	53.02 ± 0.09
2.00 (4.40)	105 ± 4	14.47 ± 0.3

Table 1 – Relaxation times for various temperatures for a 11^3 lattice.

Thus, measures near the critical temperature have its errors greatly enhanced, the region that is of interest to the present work. This enhancement is however not so drastic for temperatures way above or way below the critical. This table can be used as a guide to the number of configurations to be ignored. Typically, as the number of configuration is in the order of 10^5, and the relaxation times are at most $\sim 10^3$, the number of ignored points is $\sim 10^4$, usually taken to be 10 % of the configurations, so that a run with 1.5 10^5 measurements has its first 1.5 10^4 measurements ignored.

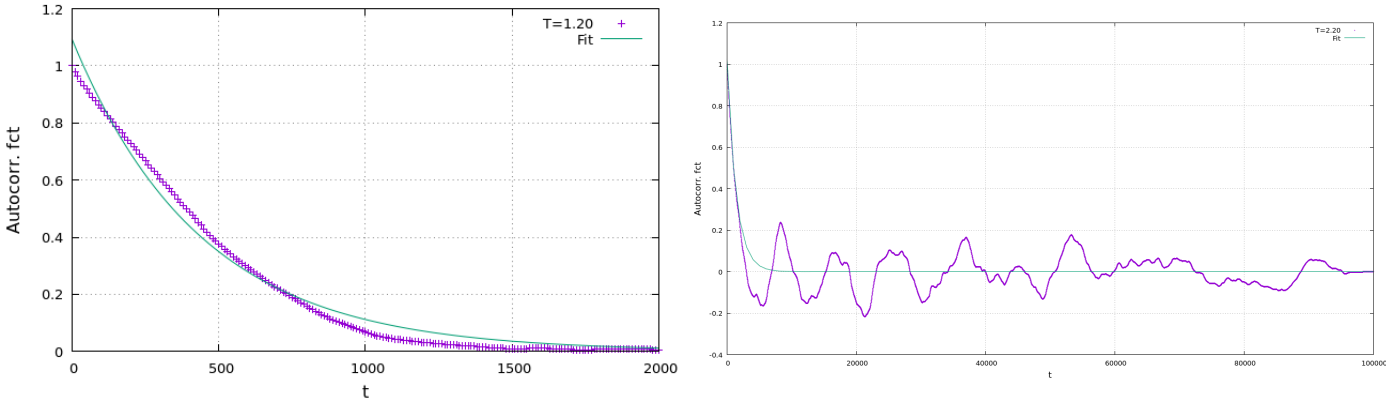

Figure 22 – Fits used to obtain the relaxation time for the magnetization for $T = 1.20 \approx 0.55T_c$ and $T = 2.20 \approx 0.998T_c$ at a 11^3 lattice.

5.2.2 The similarity between the frustrated and the unfrustrated XY models near the critical temperature

It was claimed in section 3.4 that the XY model and its frustrated counterpart, defined by (3.16), have a similar behavior near the critical temperature. That motivated the Villain expansion and the results that followed. Indeed, for the unfrustrated case, extensive tables in ref. [44] show that the Villain model can grasp really well the properties of the XY-model, even in temperatures where it seemed not to apply at first glance.

This similarity was also seen to be very important to the overlap method of section 4.4. Otherwise, the overlap problem arises and the numerical method becomes a bit more complex. To gain an extra confidence that these claims are true, some numerical calculations can be performed. The first of which is to calculate the dependence of the order parameter, the magnetization (4.21), on the temperature. This can be seen in fig. (23), in the extreme case where the frustrated region is has the maximum L^2 area.

Therefore, fig. 23 reveals that there is a big difference between the unfrustrated and the frustrated one at low temperatures. The magnetization near $T = 0$ falls down from 1.0 to approximately 0.6. This can be readily understood when one looks to the typical configuration near $T = 0$, as in the left-hand side of fig. 25. There one can see that, as energy tends to be approximately minimized, the "spins" near the frustrated region are anti-aligned (throughout this section $N = 2$ and $k = 1$, so that $\alpha_\mu = \pi$ for links that pierce the Wilson loop). In the other hand, the pairs of interacting spins whose link does not pierce $\mathcal{S}_m(\mathcal{C})$, tend to align. The compromise between these two effects yields configurations that "bend" as one gets closer to the frustrated region until the neighbooring spins in each side are anti-aligned. This hence reduces the magnetization.

These features become less significant as one goes to higher temperatures, the magnetization is near the same as one approaches the critical region. And from the left-hand side of fig. 25, it can be seen that the spins are pointing in arbitrary directions, which

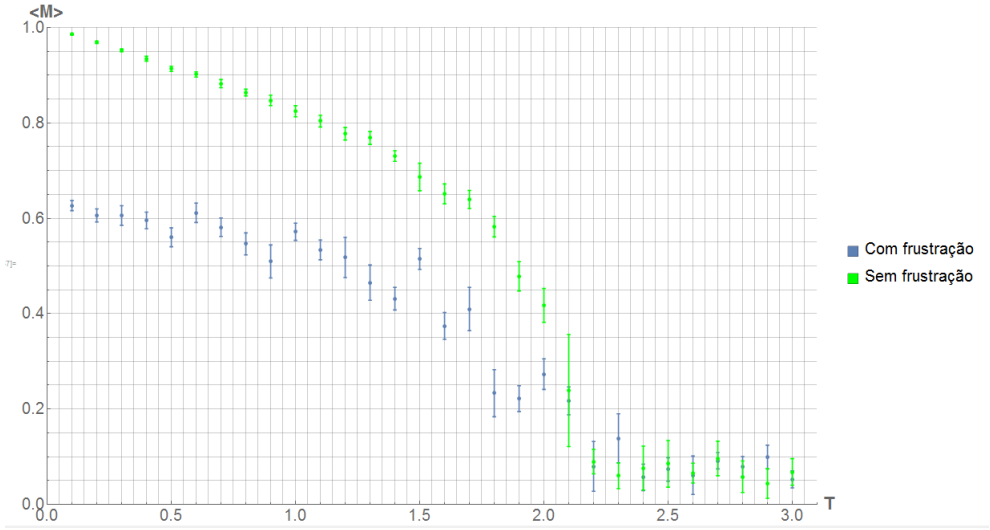

Figure 23 – Comparison between the magnetization of the unfrustrated (green) and frustrated (blue) cases as temperature varies for $L = 10$.

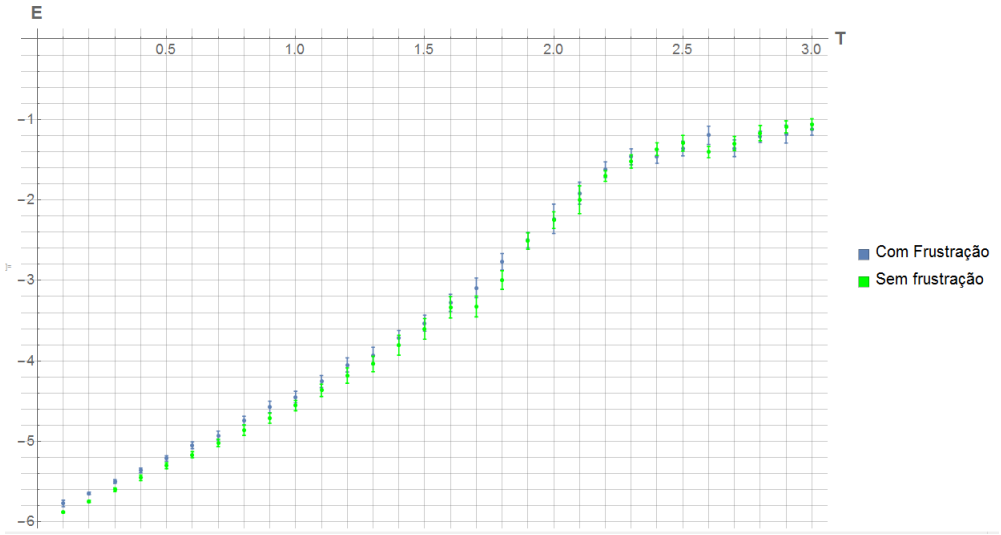

Figure 24 – Comparison between the energy of the unfrustrated (green) and frustrated (blue) cases as temperature varies for $L = 10$.

is also expected for the unfrustrated version. Hence, this is evidence that the assumption that the geometrically localized frustration does not change the critical temperature is not contradicted. One can see as well from fig. (23) that the simulations give more irregular results in the frustrated case, the error bars are not small even in the low temperature region as it is true for the unfrustrated one.

As for fig. 24, one can see that the energy surprisingly behaves almost the same in both cases for all temperatures even though, for lower temperatures the frustrated model has a slightly higher energy. It can as well be seen that this behavior for high temperatures can be an difficulting factor for the simulations near the critical temperature. Energies being near the same render the partition function ratio to be essentially 1, as one sees in

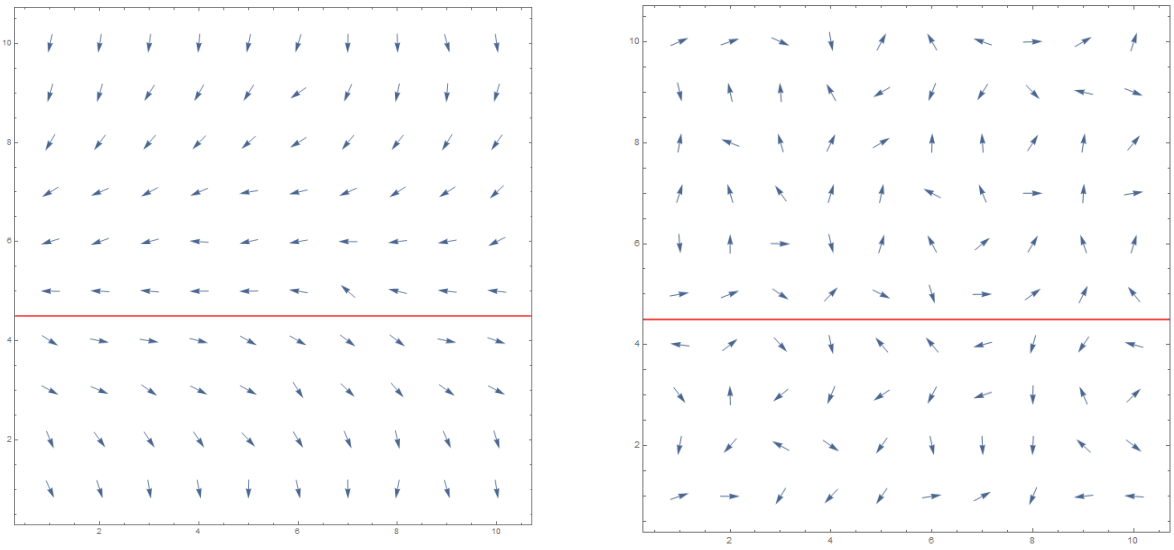

Figure 25 – Typical configurations of the frustrated 3D XY model seen in a plane transverse to the Wilson loop, which is highlighted in red, for L=10. To the left $T = 0.1 \approx 0.045T_c$, to the right, $T = 2.0 \approx 0.91T_c$

(4.29). This issue is potentially enhanced because large fluctuations in energy appear in this regime too, increasing errors.

5.3 Wilson Loop calculations in the 3D effective model

Summarizing chapter 3 and section 4.4, Wilson loop averages are translated, after a number of controlled approximations, from a effective model of center vortices to

$$\langle \mathcal{W}(\mathcal{C}) \rangle \approx \frac{Z_{XY}[\alpha_\mu(\mathbf{x})]}{Z_{XY}[0]} = \langle e^{-\beta(E_{XY,f} - E_{XY,0})} \rangle_{XY,0}, \tag{5.2}$$

where $XY, 0$ indicates that the averages are to be taken by sampling the unfrustrated XY model. The frustration, as fig. 14 indicates, lies between links that pierce the Wilson loop. For all the simulations in this section, the Wilson loop is considered to be a square whose side M is varied from M_{min} to M_{max}, so that $\mathcal{C}$ encloses M^2 frustrated links.

In this section the numerical tests for the area law predicted in section 3.4.2 will be discussed as well as the validity of (3.44) to the dependence of the area law coefficient with the N-ality of the $SU(N)$ representation. The typical Monte Carlo iteration behavior of $\mathcal{C}_{est} = e^{-\beta(E_{XY,f} - E_{XY,0})}$ can be seen in fig. 26 as well as its autocorrelation function behavior. These are taken in the case where the Wilson loop is a square of side $M = M_{min} = 2$ and for $N = 2$.

Hence, it can be seen that Wilson loop averages in general fluctuate less than magnetization at higher temperatures. As for lower temperatures, it actually fluctuates slightly more. Another difference can be seen in autocorrelation function plot. For all temperatures seen, even the near critical one, it rapidly falls to near zero values, and

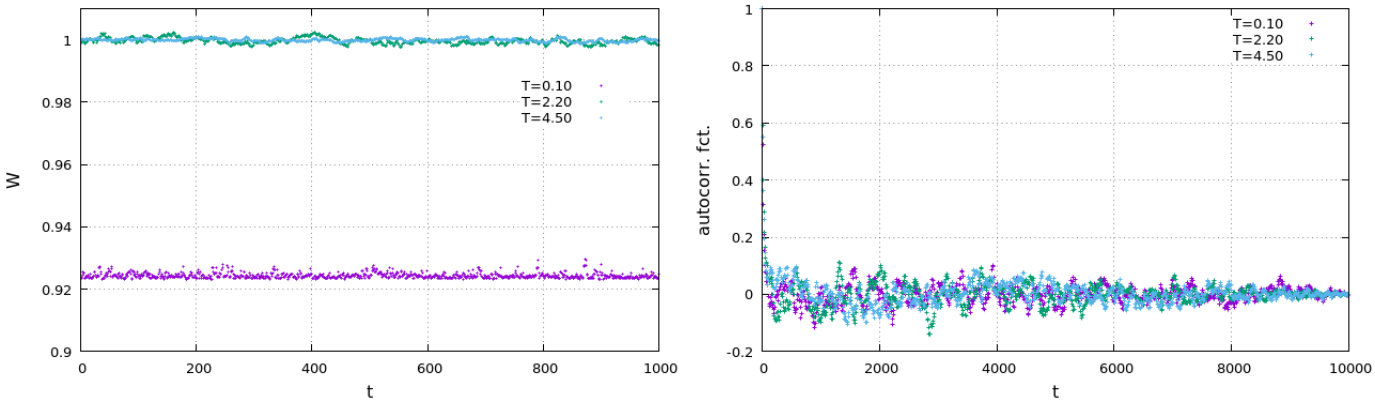

Figure 26 – (Left) Wilson loop average as a function of Monte Carlo time. (Right) Wilson loop autocorrelation function as a function of Monte Carlo time. Both graphs were obtained for $M = 2$ and $T = 0.10 \approx 0.045T_c$, $2.20 \approx 0.998T_c$ and $4.50 \approx 2.04T_c$ in a 11^3 lattice.

fluctuations around it are very similar. Thence the critical slowing down behavior is not perceivable in the averages of this quantity, this gives evidence that the notion that the order paremeter has the biggest relaxation time is correct. The relaxation times calculated for the Wilson loop are: $\tau_{\mathcal{W}}(T = 0.045T_c) = 19 \pm 1$, $\tau_{\mathcal{W}}(T = 0.998T_c) = 27 \pm 1$ and $\tau_{\mathcal{W}}(T = 2.04T_c) = 24 \pm 1$. This time, (4.16) produces realistic results.

The procedure to obtain the forthcoming results can be summarized as:

(*i*) Compute $e^{-\beta(E_{XY,f}-E_{XY,0})}$ for each Monte Carlo configuration ($N_m \sim 10^5$) of the unfrustrated XY model at fixed square size $M = 2$, and temperature $T = 1/\beta$;

(*ii*) If $M < M_{max}$ $M \mapsto M' = M + 1$, $M' \mapsto M'' = M' + 1$, etc;

(*iii*) If $M = M_{max}$, $T \mapsto T + \Delta T$, if more than one temperature is involved;

(*iv*) Take a simple average of all of the configurations generated for the different M and T, excluding the transient states.

Hence, as averages of $e^{-\beta(E_{XY,f}-E_{XY,0})}$ for bigger values of M are taken consecutively after $M = M_{min}$, at the same temperature, one is also in a sense less susceptible to critical slowing down issues.

5.3.1 The Area Law

Using a 10^3 lattice, with a range of temperatures going from 0.1 to 10.1 with a step of 1.0 unit of temperature, and $L = 10$, one obtains the general behavior for Wilson loop averages seen in fig. Wilson loop averages as a function of temperature for various sizes of frustrated region.

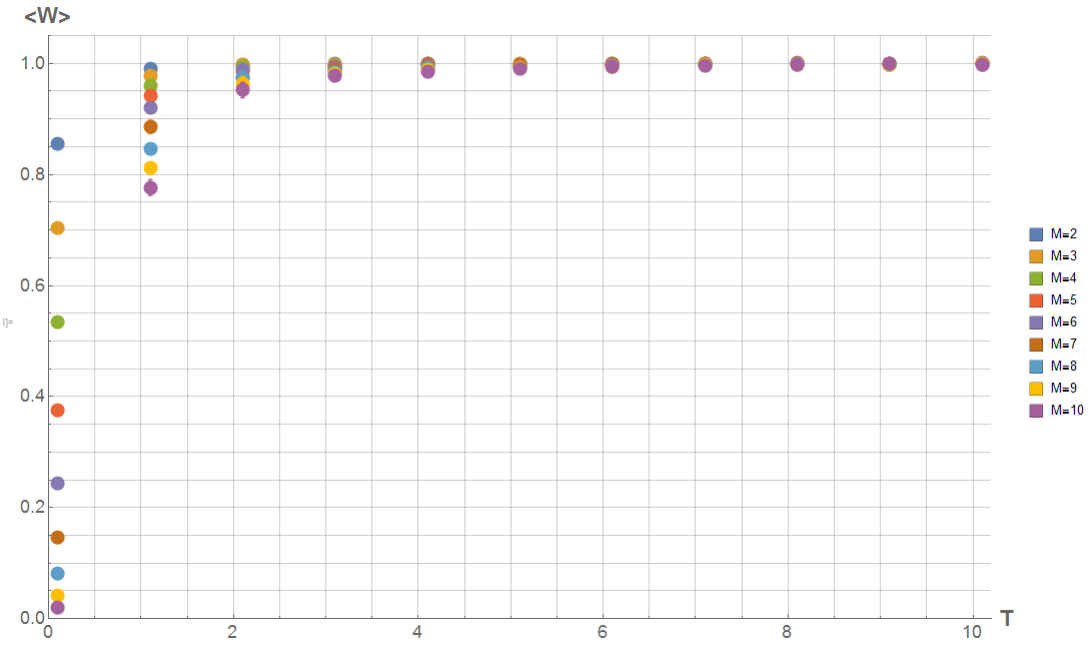

Figure 27 – Wilson loop averages as a function of temperature for various sizes of frustrated area.

Thus one can see that the general behavior for any value of loop side is that, for low temperatures, as the two systems behave so differently, the ratio between them is expected to be not so near 1, as the energies are more different in this regime, according to what was stated in the last section. Then, as temperature rises, the ratio goes to values increasingly near 1, which can be seen as if thermal fluctuations are so big in this regime and spins are so uncorrelated that even information about the frustration is lost.

Along these lines, one sees from (4.29) that the data values range between zero and one in fig. 27 because the averages are taken in the unfrustrated model which, as expected, has lower energy than its frustrated counterpart. This difference in energy grows bigger as one increases the loop length M. This also explains why the Wilson loop values for $M = 10$ (in dark purple) come from nearly zero at low temperatures and the data for $M = 2$ (in dark blue) have its low temperature values closer to 1.

One can also see that it is increasingly hard to get information from the M-dependent behavior of $\langle \mathcal{W}(\mathcal{C}) \rangle$ as the points are crammed together and the overlap between error bars grows bigger in higher temperatures. This is also true for the region near the critical temperature and one expects to more difficulties to distinguish an area

law from a perimeter law.

With this in mind fits for an perimeter-law ($\ln\langle\mathcal{W}(\mathcal{C})\rangle = -\sigma_P M + b_P$), area law ($\ln\langle\mathcal{W}(\mathcal{C})\rangle = -\sigma_A M^2 + b_A$), and polynomial ($\ln\langle\mathcal{W}(\mathcal{C})\rangle = -\sigma_\gamma M^\gamma + b$) fits were performed, the results for low ($T << T_c$), near critical ($T \approx T_c$) and high ($T >> T_c$) temperatures can be seen in tables[3] 2,3 and 4. Plots for these fits can be seen in figs. 28 -33.

T/T_c (T)	σ_P	b_P	Rms Error/d.o.f
0.045 (0.1)	0.070 ± 0.003	0.27 ± 0.03	0.03
0.14 (0.3)	0.023 ± 0.001	0.10 ± 0.01	0.009
0.23 (0.5)	0.0134 ± 0.0006	0.055 ± 0.005	0.005
0.998 (2.20)	(1.11 ± 0.05) 10^{-3}	(4.6 ± 0.4) 10^{-3}	3.6 10^{-4}
1.0032 (2.21)	(1.04 ± 0.06) 10^{-3}	(3.9 ± 0.5) 10^{-3}	5.3 10^{-4}
1.0077 (2.22)	(1.07 ± 0.05) 10^{-3}	(4.4 ± 0.5) 10^{-3}	4.1 10^{-4}
1.012 (2.23)	(9.9 ± 0.6) 10^{-4}	(3.8 ± 0.5) 10^{-3}	5.2 10^{-4}
1.017 (2.24)	(1.02 ± 0.05) 10^{-3}	(4.2 ± 0.5) 10^{-3}	3.8 10^{-4}
1.021 (2.25)	(9.5 ± 0.5) 10^{-4}	(3.6 ± 0.5) 10^{-3}	4.6 10^{-4}
1.026 (2.26)	(9.8 ± 0.4) 10^{-4}	(4.0 ± 0.4) 10^{-3}	3.4 10^{-4}
3.63 (8.0)	(5.9 ± 0.3) 10^{-5}	(2.4 ± 0.3) 10^{-4}	2.3 10^{-5}
4.08 (9.0)	(4.6 ± 0.3) 10^{-5}	(1.9 ± 0.2) 10^{-4}	2.0 10^{-5}
4.54 (10.0)	(3.7 ± 0.2) 10^{-5}	(1.5 ± 0.2) 10^{-4}	1.4 10^{-5}

Table 2 – Fit coefficients for a perimeter law for various temperatures for a $L = 17$ cubic lattice.

T/T_c (T)	σ_A	b_A	Rms Error/d.o.f
0.045 (0.1)	(4.00244 ± 0.00002) 10^{-3}	(-1 ± 3) 10^{-6}	3.7 10^{-6}
0.14 (0.3)	(1.28729 ± 0.00008) 10^{-3}	(6 ± 8) 10^{-6}	1.1 10^{-5}
0.23 (0.5)	(7.4299 ± 0.0003) 10^{-4}	(-4 ± 3) 10^{-6}	4.6 10^{-6}
0.998 (2.20)	(6.19 ± 0.04) 10^{-5}	(5 ± 4) 10^{-5}	5.9 10^{-5}
1.0032 (2.21)	(6.15 ± 0.03) 10^{-5}	(2 ± 3) 10^{-5}	5.3 10^{-5}
1.0077 (2.22)	(5.96 ± 0.02) 10^{-5}	(9 ± 20) 10^{-6}	2.8 10^{-5}
1.012 (2.23)	(5.86 ± 0.04) 10^{-5}	(3 ± 4) 10^{-5}	6.7 10^{-5}
1.017 (2.24)	(5.68 ± 0.05) 10^{-5}	(2 ± 5) 10^{-5}	6.6 10^{-5}
1.021 (2.25)	(5.57 ± 0.02) 10^{-5}	(6 ± 20) 10^{-6}	3.0 10^{-5}
1.026 (2.26)	(5.46 ± 0.03) 10^{-5}	(-2 ± 3) 10^{-5}	4.3 10^{-5}
3.63 (8.0)	(3.28 ± 0.04) 10^{-6}	(4 ± 4) 10^{-6}	5.8 10^{-6}
4.08 (9.0)	(2.57 ± 0.03) 10^{-6}	(3 ± 3) 10^{-6}	4.2 10^{-6}
4.54 (10.0)	(2.04 ± 0.03) 10^{-6}	(-1 ± 3) 10^{-6}	3.7 10^{-6}

Table 3 – Fit coefficients for a area law for various temperatures for a $L = 17$ cubic lattice.

[3] In these tables, the square of "Rms Error/d.o.f" is the sum of squares of the deviations divided by the number of the degrees of freedom of the plot, i.e. the number of points minus the number of fitting parameters.

T/T_c (T)	γ	σ_γ	b_γ	Rms Error/d.o.f
0.045 (0.1)	2.00000 ± 0.00006	(4.00276 ± 0.0006) 10^{-3}	(4 ± 8) 10^{-6}	4.0 10^{-6}
0.14 (0.3)	2.00032 ± 0.0004	(1.286 ± 0.001) 10^{-3}	(-1 ± 2) 10^{-5}	1.1 10^{-5}
0.23 (0.5)	1.9998 ± 0.0004	(7.434 ± 0.008) 10^{-3}	(1 ± 10) 10^{-5}	4.8 10^{-6}
0.998 (2.20)	1.87 ± 0.03	(8.8 ± 0.8) 10^{-5}	(2.6 ± 0.9) 10^{-4}	3.3 10^{-5}
1.0032 (2.21)	2.07 ± 0.03	(5.1 ± 0.5) 10^{-5}	(1.2 ± 0.7) 10^{-5}	4.4 10^{-5}
1.0077 (2.22)	2.02 ± 0.02	(5.5 ± 0.4) 10^{-5}	(-5 ± 6) 10^{-5}	2.8 10^{-5}
1.012 (2.23)	2.09 ± 0.04	(4.6 ± 0.5) 10^{-5}	(1.4 ± 0.8) 10^{-4}	5.6 10^{-5}
1.017 (2.24)	1.98 ± 0.07	(6 ± 1) 10^{-5}	(6 ± 168) 10^{-6}	7.1 10^{-5}
1.021 (2.25)	2.00 ± 0.03	(5.5 ± 0.4) 10^{-5}	(8 ± 51) 10^{-5}	3.2 10^{-5}
1.026 (2.26)	1.93 ± 0.04	(6.5 ± 0.8) 10^{-5}	(1.1 ± 0.9) 10^{-4}	4.0 10^{-5}
3.63 (8.0)	2.0 ± 0.1	(2.9 ± 0.9) 10^{-6}	(-1 ± 10) 10^{-6}	6.2 10^{-6}
4.08 (9.0)	2.22 ± 0.06	(1.4 ± 0.2) 10^{-6}	(-1.5 ± 0.5) 10^{-6}	2.5 10^{-6}
4.54 (10.0)	1.9 ± 0.1	(2.1 ± 0.7) 10^{-6}	(5 ± 90) 10^{-6}	4.0 10^{-6}

Table 4 – Fit coefficients for a polynomial law for various temperatures for a $L = 17$ cubic lattice.

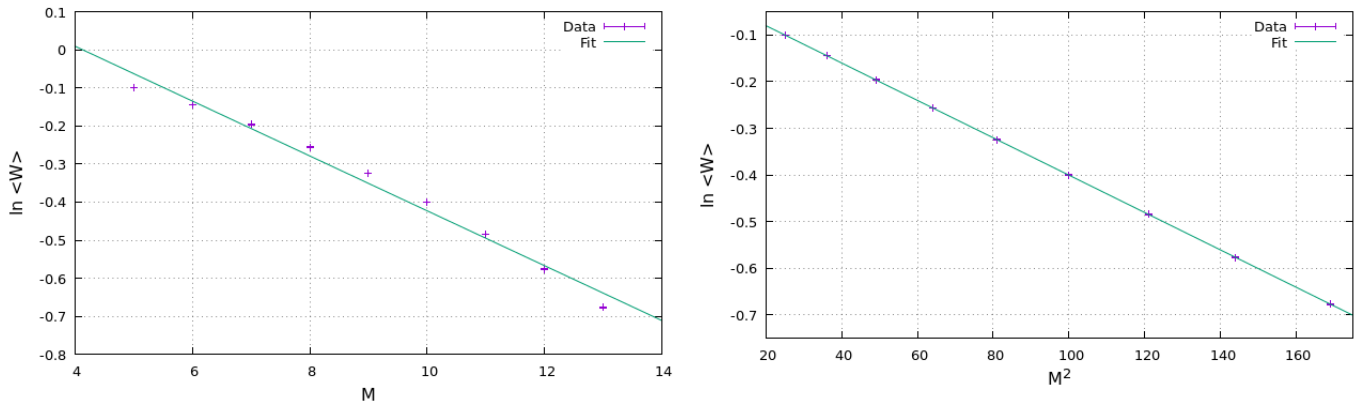

Figure 28 – Perimeter (left) and area (right) fits for Wilson loop averages. $L = 17$ and $T = 0.10 \approx 0.045T_c$

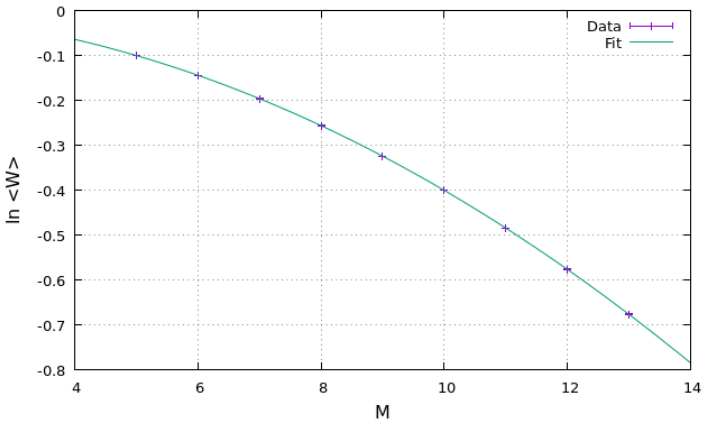

Figure 29 – Polynomial fit for Wilson loop averages. $L = 17$ and $T = 0.1 \approx 0.045T_c$

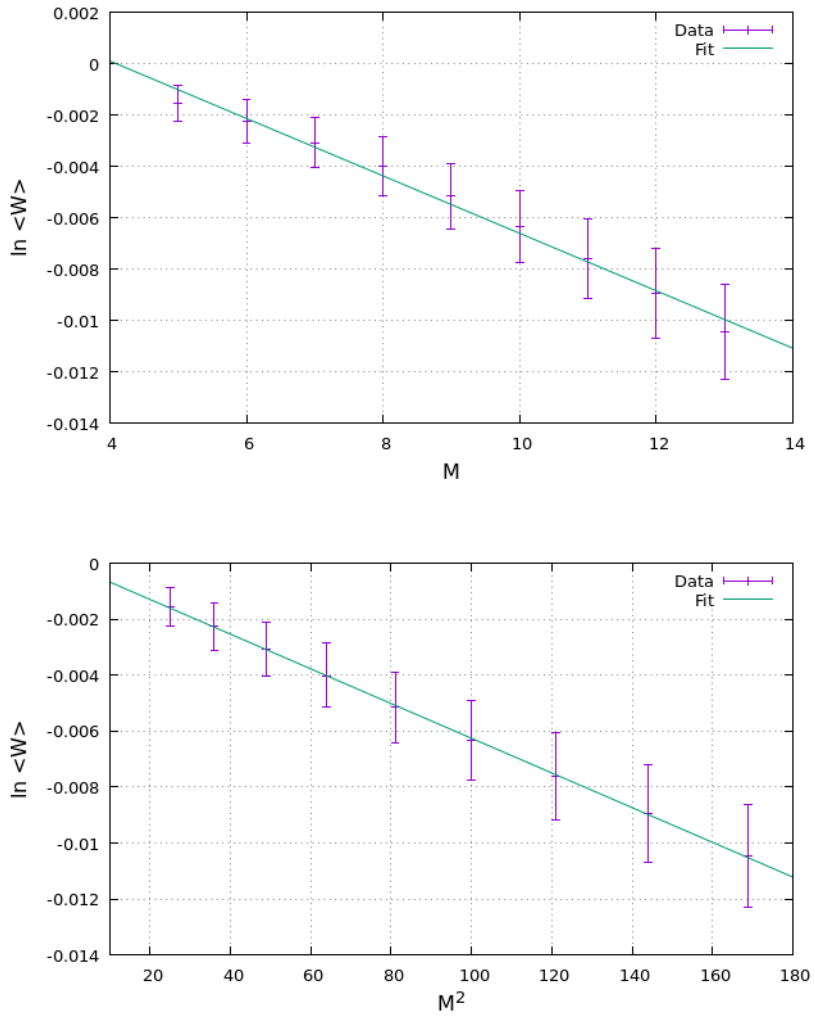

Figure 30 – Polynomial fit for Wilson loop averages. $L = 17$ and $T = 2.20 \approx 0.998 T_c$

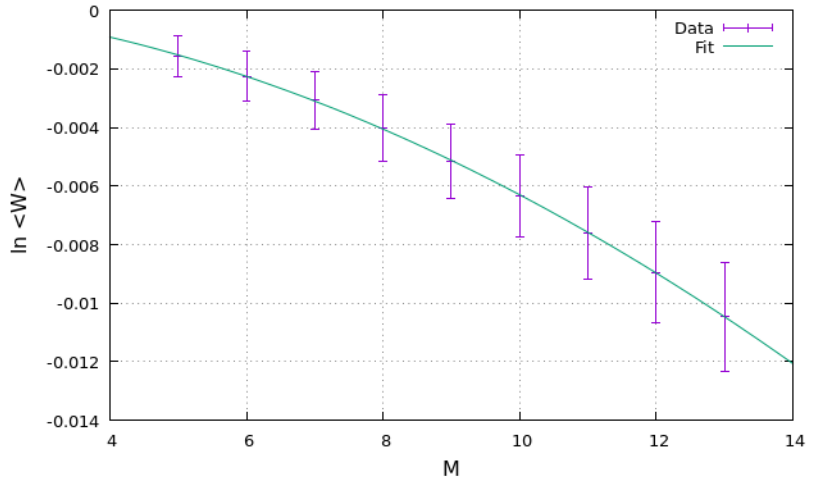

Figure 31 – Polynomial fit for Wilson loop averages. $L = 17$ and $T = 2.20 \approx 0.998 T_c$

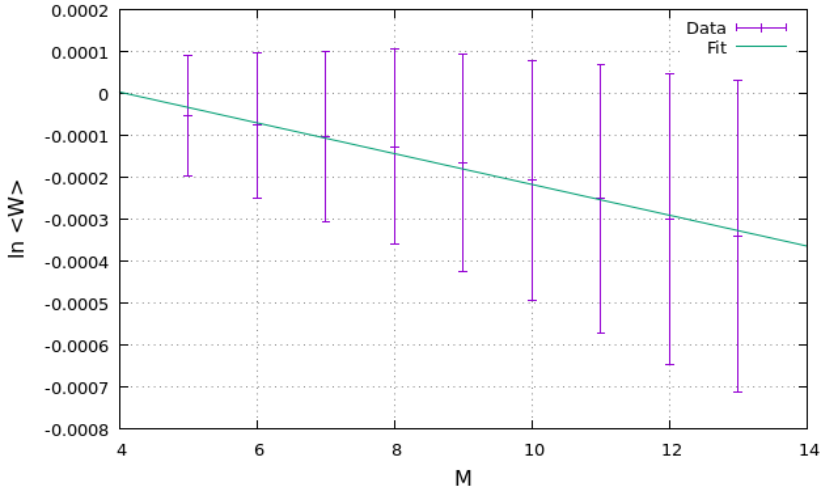

Figure 32 – Polynomial fit for Wilson loop averages. $L = 17$ and $T = 10.0 \approx 4.54T_c$

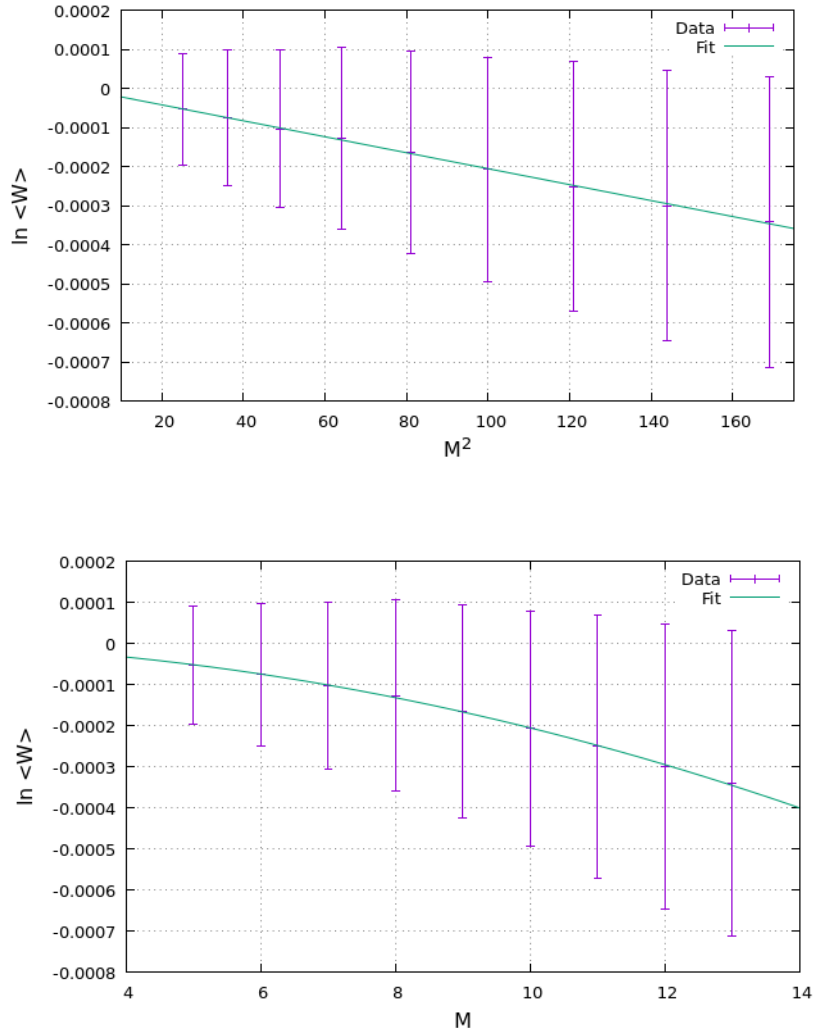

Figure 33 – Polynomial fit for Wilson loop averages. $L = 11$ and $T = 10.0 \approx 4.54T_c$

It is then evident that, for low temperatures, the area law is the best fit for the behavior of the Wilson loop. There is a 0.04 % disagreement between the data and $\gamma_{area} = 2$ for the polynomial fit. This behavior persists in the near critical region, where one expects to recover the properties of the continuum. This however with a lower degree of agreement due to the huge fluctuations involved. Surprisingly, this area-behavior persists even at higher temperatures, where a perimeter law was expected.

One can also see that σ_A, σ_P and σ_γ get smaller as the temperature increases. This can be readily explained by the fact that the small energy difference seen in this regime in fig. 24 is greatly enhanced by the $1/T$ factor. Plus, the values of b_A and b_γ, which correspond to the best fits for the behavior, are almost all consistent with zero within the error bars, that means that $\langle \mathcal{W}(\mathcal{C}) \rangle \approx 1\ e^{-\sigma A}$.

From a frustrated XY model-level argument, an area law is expected because of the simple fact that drastic information about the area is given when it is imposed that the only links that have a frustrated interaction are those that pierce the minimal surface whose boundary is the Wilson loop. This motivates the solid angle picture, which will be approached later. In the following, tests will be performed for non-minimal areas.

5.3.2 Representation dependence

With numerical evidence that the area law is the correct behavior near the critical temperature, we now turn our attention to the dependence of the area law coefficient σ_A on the N-ality of the $SU(N)$ representation. It was seen in the end of section 3.4.2 that, in the context of the effective 3D XY model, this dependence is expected to be a sine-square law. To this end, now one performs fits of the form $\ln\langle \mathcal{W}(\mathcal{C}) \rangle = -\sigma_A M^2 + b_A$ for the different k and N.

For each $N = 6 - 10$ fits of the form $\sigma_A^N(k)/\sigma_A^N(1) = a \sin^2\left(b\frac{2k}{N}\right)$ for fitting parameters a and b were performed in order to confirm or not eq. (3.44). These values of N were chosen because they have more that two data points, which is the number of fit parameters. The data is presented in Table 5, with the respective expected results, $a_{xpc} = (\sin(\pi/N))^{-2}$, $b_{xpc} = \pm\pi/2$. The plot of the fit for $N = 9, 10$ are in fig. 34. In fig. 35, all the area-law coefficients from $N = 2$ to $N = 10$ are plotted together.

N	a	a_{xpc}	b	b_{xpc}	Rms error/d.o.f.
6	3.918 ± 0.001	4	1.5896 ± 0.0006	± 1.570796327	0.0011
7	5.24 ± 0.02	5.31194111	1.580 ± 0.004	±1.570796327	0.0045
8	6.667 ± 0.005	6.828427125	-1.590 ± 0.002	±1.570796327	0.0090
9	8.48 ± 0.03	8.54863217	1.576 ± 0.004	± 1.570796327	0.013
10	10.51 ± 0.04	10.47213596	1.581 ± 0.006	± 1.570796327	0.033

Table 5 – Sine-square law fit coeficients for L=11 and $T = 2.20 \approx 0.998 T_c$.

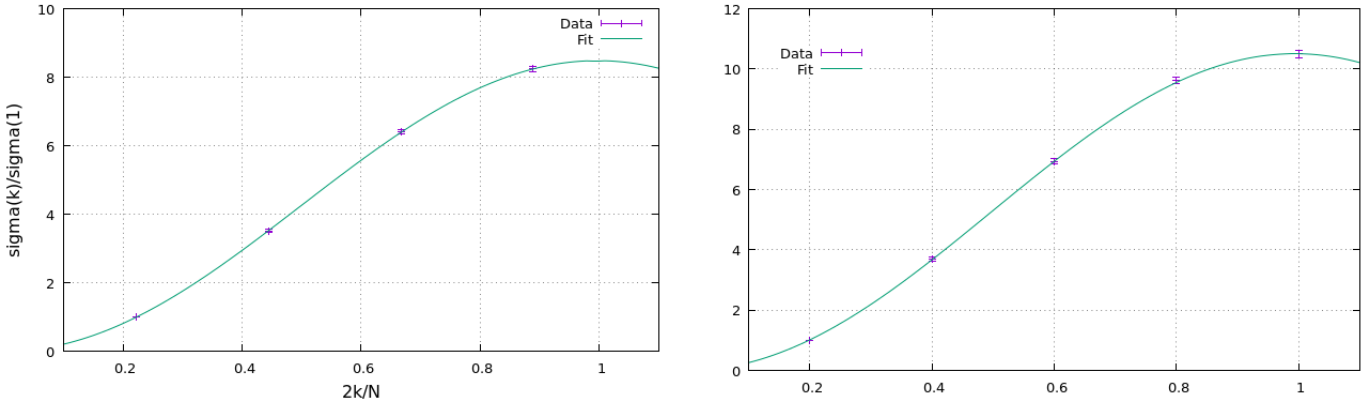

Figure 34 – Sine-square law fit for $N = 9$ (left) and $N = 10$ (right) for L=11 and $T = 2.20 \approx 0.998 T_c$.

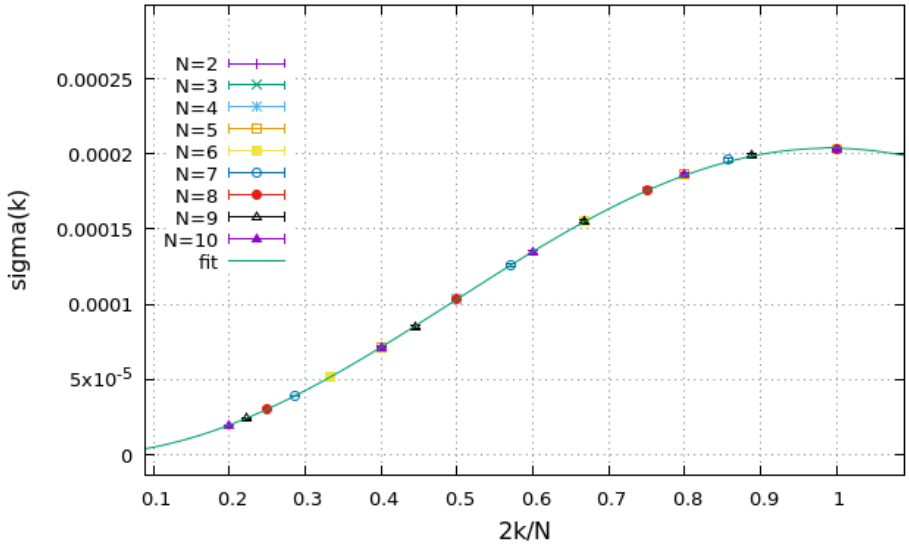

Figure 35 – Plot of all k-string tensions from $N = 2$ to $N = 10$

Thus it can be seen that there is a quite good agreement between eq. (3.44) and the results obtained from the simulations near the critical temperature. The points fall within the fit consistently with their error bars. The disagreement between the values of a and b are at most of 2 % and 1% respectively both for $N = 6$. However, it is important to notice that not all values of a and b agree with their expected value within the errors. This can be seen as being a finite volume effect, and better results are expected for larger lattices. It can also be seen that the fits get worse as N increases, as evidenced by the rms errors, but this does not hamper much the analysis.

A sine-square fit ($\sigma_A^N(k) = a \sin^2(b\frac{2k}{N})$) was then done to all the $\sigma_A^N(k)$ from $N = 2$ to $N = 10$ and that resulted in $a = (2.038 \pm 0.002)\ 10^{-4}$, $b = 1.586 \pm 0.002$, with an rms error of $4.1\ 10^{-7}$. Hence, b disagrees with $\pi/2$ by just 0.96 %, and implying that $\sigma_A^N(1)/\sin^2\frac{\pi}{N} \approx 2.038\ 10^{-4}$. From, fig. 35, it can as well be seen that the fit has indeed a good agreement with the data.

5.4 The Non-Minimal Surface

In the paragraph just above eq. (3.18) the minimal surface $\mathcal{S}_m(\mathcal{C})$ chosen to be the one where the frustration is localized, but, as it is known from Stokes' theorem any other surface whose boundary is the Wilson loop is equally good to compute the flux integral (3.4) in the beginning of the discussion of the effective model.

So, to show that this property is still obeyed with XY-model-level arguments, we will exploit the fact that the partition function (3.17) can be rewritten as [4]

$$\begin{aligned} Z[\alpha_\mu(\mathbf{x})] &= \int \mathcal{D}\theta \ \exp\beta \sum_{\mathbf{x},\mu} \cos(\theta(\mathbf{x}+\hat{\mu}) - \theta(\mathbf{x}) - \alpha_\mu^{\mathcal{S}_m(\mathcal{C})}(\mathbf{x})) \\ &= \int \mathcal{D}\tilde{\theta} \ \exp\beta \sum_{\mathbf{x},\mu} \cos(\tilde{\theta}(\mathbf{x}+\hat{\mu}) + \Theta(\mathbf{x}+\hat{\mu}) - \tilde{\theta}(\mathbf{x}) - \Theta(\mathbf{x}) - \alpha_\mu^{\mathcal{S}_m(\mathcal{C})}(\mathbf{x})). \end{aligned} \tag{5.3}$$

where each θ variables were shifted by the following lattice Heaviside function

$$\Theta(\mathbf{x}) := \begin{cases} \frac{2\pi}{N} & \text{if } \mathbf{x} \text{ lies outside } \mathcal{S}_{clo}(\mathcal{C}) \\ 0 & \text{if } \mathbf{x} \text{ lies inside } \mathcal{S}_{clo}(\mathcal{C}) \end{cases}. \tag{5.4}$$

Where $\mathcal{S}_{clo}$ is the closed surface formed by joining $\mathcal{S}_m(\mathcal{C})$ with any other surface whose boundary is $\mathcal{C}$. Let us call this non-minimal surface $\mathcal{S}_{Nm}(\mathcal{C})$. One example of such surface can be seen in fig. 36. One can readily see that $\Theta(x+\hat{\mu}) - \Theta(x)$ implements a frustration in those links that pierce $\mathcal{S}_{clo}$. This is so because the subtraction vanishes if both $x+\hat{\mu}$ and x lie inside or outside $\mathcal{S}_{clo}$ and it gives $2\pi/N$ if they lie in opposite sides of $\mathcal{S}_{clo}$.

Thus, the sum $\Theta(x+\hat{\mu}) - \Theta(x) - \alpha_\mu^{\mathcal{S}_m(\mathcal{C})}(\mathbf{x})$ results in zero if one considers links that pierce $\mathcal{S}_m(\mathcal{C})$ and then the frustration is now placed in those links that pierce $\mathcal{S}_{Nm}(\mathcal{C})$,

$$Z[\alpha_\mu(x)] = \int \mathcal{D}\theta \ \exp\beta J \sum_{\mathbf{x},\mu} \cos(\theta(\mathbf{x}+\hat{\mu}) - \theta(\mathbf{x}) - \alpha_\mu^{\mathcal{S}_{Nm}(\mathcal{C})}(\mathbf{x})), \tag{5.5}$$

and what we first wanted to demonstrate is confirmed. It can also be concluded by a similar argument that, if one has a closed surface, the two partition functions are equal. Then there can be no area law for the Wilson loop.

However, when the simulations on this case are run, the results do not support this idea. A ratio between the area law coefficient obtained with minimal area frustration simulations and the one obtained in closed surface area can be seen in fig. 37. This ratio should be zero if there was no surface dependence, as a closed surface has no boundary. However, the observed ratio is nearly 6 in all temperatures near the critical one.

[4] In this section, we will show explicitly the surface where the frustration is located. Thus $\alpha_\mu(\mathbf{x})$ in the action (3.16) is now $\alpha_\mu^{\mathcal{S}_m(\mathcal{C})}(\mathbf{x})$

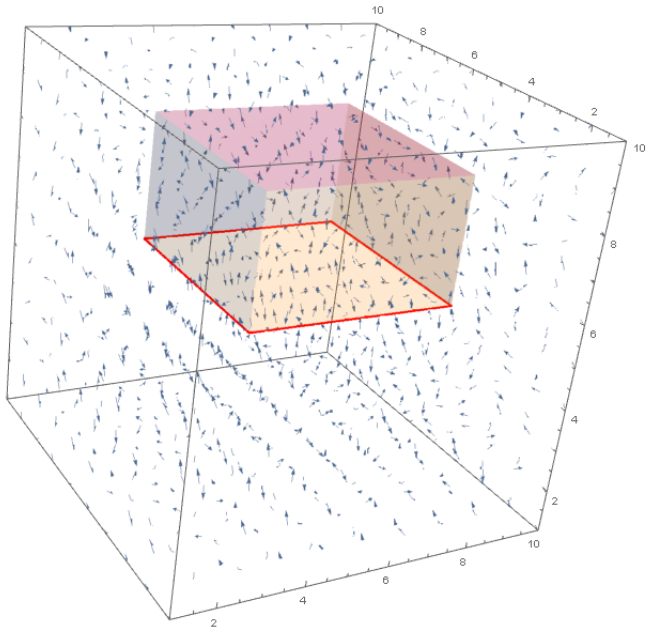

Figure 36 – Pictorial representation of a non-minimal surface $\mathcal{S}_{Nm}(\mathcal{C})$. Here $\mathcal{C}$ is highlighted in red.

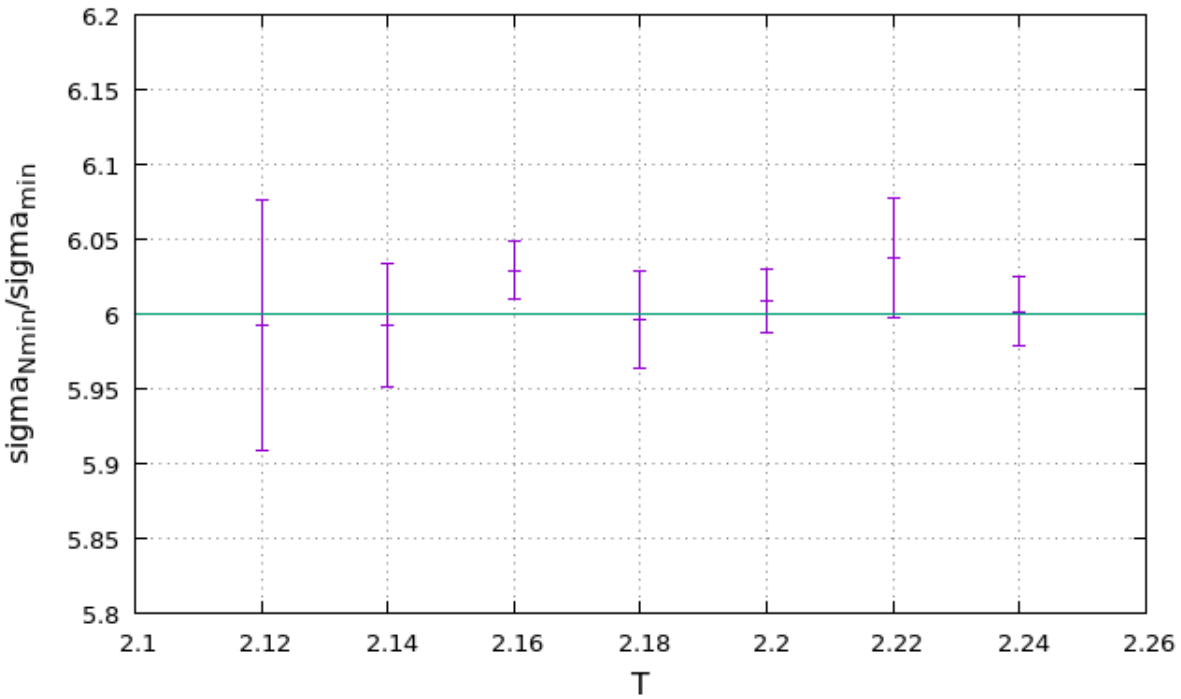

Figure 37 – Area-law fit coefficient ratio between the case when the frustration is localize in a closed surface and the one localized in the minimal surface near the critical temperature.

As the unfrustrated system and the closed-surface-localized frustration are so different from each other, one may think that these computations are not in the range of validity of eq. (4.29). Thus, in an attempt to solve the inconsistencies presented above, one may try to use the method described in the end of section 4.4, in eq. (4.37). It consists of

dividing the computation of the ratio between partition functions in steps, so that in each step the couple of systems are in a sense "more similar" to each other. In the present case, the procedure adopted was to take these intermediate as being systems with an increasing number of frustrated faces, so that the original ratio becomes

$$\frac{Z_{clo}[\alpha_\mu(\mathbf{x})]}{Z[0]} = \frac{Z_1}{Z[0]}\frac{Z_2}{Z_1}\cdots\frac{Z_{clo}[\alpha_\mu(\mathbf{x})]}{Z_5} = \\ \langle e^{-\beta(E_{XY,1}-E_{XY,0})}\rangle_{XY,0}\langle e^{-\beta(E_{XY,2}-E_{XY,1})}\rangle_{XY,1}\cdots\langle e^{-\beta(E_{clo}-E_{XY,5})}\rangle_{XY,5} \tag{5.6}$$

where $XY,1$ denotes that the system has only one frustrated face (just like the minimal surface case) $XY,2$ has two frustrated faces and so on, until one has six frustrated faces. The result found for $L = 15$ and $T = 2.20$ however is 5.37 ± 0.03 times bigger than the corresponding minimal surface, which still evidences a surface dependence. One sees however that this value is near the value 5.61 ± 0.03 found by the "direct" approach.

5.5 The Solid Angle Picture

It was previously argued (cf. section 3.5) that the essential properties of the effective model near the critical temperature can be captured by a frustration that has an equivalent circulation around the Wilson loop. In this context, the solid angle picture arose. The explicit formulation for the solid angle subtended by a square can be seen in Appendix C. As in the case of the surface-concentrated frustration, the Wilson loop is thought to lie between the lattice planes.

The solid angle defined in Appendix C (eqs. (C.13)-(C.16)) ranges between $[0, 2\pi]$. Simulation results with this "raw" definition can be seen in table 6. However, this definition of the solid angle obeys

$$\sum_{\square} \alpha_\mu(\mathbf{x}) = 0 \tag{5.7}$$

instead of eq. (3.51) when $\square$ links the Wilson loop. Thus, if the solid angle is to be implemented in a way that its multivaluedness appears, it should range $[0, 4\pi]$, and the solid angle measured below the loop should be $4\pi - \chi$ instead of χ, for $\chi \in [0, 2\pi]$. This, however, if naively implemented, makes the finite differences between some links to be huge, and that also does not enforce the multivaluedness of the solid angle as one winds around the Wilson loop. Moreover, a *growth* area law for Wilson loop averages is this yielded.

Namely, this big $\Delta_\mu\chi$ problem happens for links: (i) that pierce the plane that contain the Wilson loop from outside of it; (ii) that are near the lower boundary of the lattice. This happens due to the periodic boundary conditions[5]. That makes points under

[5] The computations of χ also take into account the periodic boundary conditions. This does not have a big effect in the simlations, because the biggest values of M are not so close to the size of the lattice. Furthermore, the center of the square is always taken to be in the center of the lattice plane.

the Wilson loop interact with points above it. These 'singular' links must be corrected, and this is done directly in the energy computations. It was seen for links in group (i) that $\Delta_\mu\chi \sim -4\pi$, group (ii) has two subgroups: $(ii-a)$ of points that pierce strictly on the outside, for which $\Delta_\mu\chi \sim 4\pi$; and $(ii-b)$ that pierce the loop right on its border, which happens more drastically for odd values of the loop side, for these, $\Delta_\mu\chi \sim 2\pi$.

The correction is done through a conditional that diminishes the module of these abnormal differences of solid angles. For instance, if $\Delta_\mu\chi \leq -9.0$, $\Delta_\mu\chi \mapsto \Delta_\mu\chi + 4\pi$, else, if $\Delta_\mu\chi \geq 9.0$, $\Delta_\mu\chi \mapsto \Delta_\mu\chi - 4\pi$, else, if $-9.0 \leq \Delta_\mu\chi \leq -4.0$, $\Delta_\mu\chi \mapsto \Delta_\mu\chi + 2\pi$, if $4.0 \leq \Delta_\mu\chi \leq 9.0$, $\Delta_\mu\chi \mapsto \Delta_\mu\chi - 2\pi$. The cutoff values 4.0 and 9.0 were found by inspection on what was the range of the $\Delta_\mu\chi$ values in the various cases. In the following, results for polynomial fits for Wilson loop averages can be seen in table 7 below. Some of the corresponding plots can be seen in figs. 38, 40 and 42.

$T/T_c(T)$	γ	σ_γ	b_γ	Rms Error/d.o.f.
0.998 (2.20)	1.2 ± 0.2	(1.2 ± 0.8) 10^{-4}	(2 ± 3) 10^{-4}	0.11
1.007 (2.22)	0.9 ± 0.2	(3 ± 2) 10^{-4}	(7 ± 5) 10^{-4}	0.069
1.017 (2.24)	0.8 ± 0.3	(4 ± 4) 10^{-4}	(9 ± 7) 10^{-4}	0.087
1.026 (2.26)	1.0 ± 0.3	(2 ± 2) 10^{-4}	(6 ± 5) 10^{-4}	0.082
1.035 (2.28)	0.9 ± 0.3	(3 ± 3) 10^{-4}	(7 ± 7) 10^{-4}	0.11
1.044 (2.30)	0.9 ± 0.3	(3 ± 3) 10^{-4}	(6 ± 5) 10^{-4}	0.084
1.053 (2.32)	0.9 ± 0.3	(2 ± 2) 10^{-4}	(6 ± 6) 10^{-4}	0.10

Table 6 – Polynomial fit parameters found for simulations with a "raw" definition of the solid angle for a L=17 lattice.

$T/T_c(T)$	γ	σ_γ	b_γ	Rms Error/d.o.f.
0.045 (0.10)	1.7 ± 0.2	(3.7 ± 2.0) 10^{-3}	(-0.03 ± 1) 10^{-2}	7.3 10^{-3}
0.14 (0.30)	1.7 ± 0.2	(1.2 ± 0.6) 10^{-3}	(-0.05 ± 5) 10^{-3}	2.4 10^{-3}
0.23 (0.50)	1.7 ± 0.2	(7 ± 4) 10^{-4}	(-0.09 ± 3) 10^{-4}	1.4 10^{-3}
0.998 (2.20)	1.7 ± 0.2	(5 ± 3) 10^{-5}	(-0.4 ± 2) 10^{-4}	1.1 10^{-4}
1.0032 (2.21)	1.8 ± 0.2	(4 ± 3) 10^{-5}	(-0.9 ± 2) 10^{-4}	1.2 10^{-4}
1.0077 (2.22)	1.7 ± 0.2	(5 ± 3) 10^{-5}	(-0.2 ± 3) 10^{-4}	1.5 10^{-4}
1.012 (2.23)	1.8 ± 0.2	(4 ± 2)10^{-5}	(-0.8 ± 2) 10^{-4}	9.5 10^{-5}
1.017 (2.24)	1.8 ± 0.2	(5 ± 3) 10^{-5}	(-0.3 ± 2) 10^{-4}	1.5 10^{-4}
1.021 (2.25)	1.7 ± 0.2	(6 ± 3)10^{-5}	(0.2 ± 3) 10^{-4}	1.2 10^{-4}
1.026 (2.26)	1.7 ± 0.2	(5 ± 3)10^{-5}	(0.02 ± 2) 10^{-4}	9.8 10^{-5}
3.63 (8.00)	1.6 ± 0.2	(4 ± 3) 10^{-6}	(0.9 ± 2) 10^{-5}	7.7 10^{-6}
4.08 (9.00)	1.8 ± 0.3	(2 ± 1) 10^{-6}	(0.06 ± 1) 10^{-5}	6.8 10^{-6}
4.54 (10.00)	1.7 ± 0.2	(2 ± 2) 10^{-6}	(0.2 ± 1) 10^{-5}	4.9 10^{-6}

Table 7 – Polynomial fit parameters found for simulations with singularity-removed definition of the solid angle for a L=17 lattice.

$T/T_c(T)$	γ	σ_γ	b_γ	Rms Error/d.o.f.
0.045 (0.10)	1.77 ± 0.02	(3.2 ± 0.2) 10^{-3}	(-4 ± 1) 10^{-3}	4.6 10^{-4}
0.14 (0.30)	1.77 ± 0.01	(1.06 ± 0.04) 10^{-3}	(-1.4 ± 0.3) 10^{-3}	1.2 10^{-4}
0.23 (0.50)	1.77 ± 0.02	(5.9 ± 0.2) 10^{-4}	(-9 ± 2) 10^{-4}	7.2 10^{-5}
0.998 (2.20)	1.67 ± 0.09	(7 ± 2) 10^{-5}	(0.05 ± 1) 10^{-4}	3.7 10^{-5}
1.0032 (2.21)	1.79 ± 0.07	(4.7 ± 0.8) 10^{-5}	(-1.1 ± 0.7) 10^{-4}	2.6 10^{-5}
1.0077 (2.22)	1.66 ± 0.05	(5.9 ± 0.7) 10^{-5}	(3 ± 5) 10^{-4}	1.6 10^{-5}
1.012 (2.23)	1.77 ± 0.09	(5 ± 1) 10^{-5}	(-7 ± 8) 10^{-5}	3.2 10^{-5}
1.017 (2.24)	1.92 ± 0.05	(3.1 ± 0.4) 10^{-5}	(-1.5 ± 0.4) 10^{-4}	1.8 10^{-5}
1.021 (2.25)	1.72 ± 0.05	(5 ± 8) 10^{-5}	(-1 ± 5) 10^{-5}	2.0 10^{-5}
1.026 (2.26)	1.75 ± 0.07	(5 ± 1) 10^{-5}	(-7 ± 8) 10^{-4}	2.8 10^{-5}
3.63 (8.00)	1.78 ± 0.05	(2.7 ± 0.4) 10^{-6}	(-0.2 ± 3) 10^{-6}	1.15 10^{-6}
4.08 (9.00)	2.1 ± 0.2	(1 ± 0.5) 10^{-6}	(-7 ± 7) 10^{-6}	3.5 10^{-6}
4.54 (10.00)	1.75 ± 0.08	(1.7 ± 0.4) 10^{-6}	(-3 ± 3) 10^{-6}	1.1 10^{-6}

Table 8 – Polynomial fit parameters found for simulations with singularity-removed definition of the solid angle for a L=17 lattice using only even values of M.

$T/T_c(T)$	γ	σ_γ	b_γ	Rms Error/d.o.f.
0.045 (0.10)	1.80 ± 0.01	(2.85 ± 0.08) 10^{-3}	(-3.2 ± 0.8) 10^{-3}	2.5 10^{-4}
0.14 (0.30)	1.80 ± 0.01	(9.2 ± 0.3) 10^{-4}	(-1.0 ± 0.3) 10^{-3}	8.1 10^{-5}
0.23 (0.50)	1.80 ± 0.01	(5.3 ± 0.2) 10^{-4}	(-6 ± 2) 10^{-4}	5.6 10^{-5}
0.998 (2.20)	1.87 ± 0.09	(4 ± 1) 10^{-5}	(-1 ± 1) 10^{-4}	3.4 10^{-5}
1.0032 (2.21)	1.92 ± 0.07	(3.1 ± 0.6) 10^{-5}	(-1.7 ± 0.7) 10^{-4}	2.4 10^{-5}
1.0077 (2.22)	1.86 ± 0.03	(3.2 ± 0.3) 10^{-5}	(-1.2 ± 0.3) 10^{-4}	9.7 10^{-6}
1.012 (2.23)	1.94 ± 0.06	(2.8 ± 0.5) 10^{-5}	(-2.0 ± 0.6) 10^{-4}	2.1 10^{-5}
1.017 (2.24)	1.83 ± 0.05	(3.7 ± 0.5) 10^{-5}	(-9 ± 5) 10^{-4}	1.5 10^{-4}
1.021 (2.25)	1.82 ± 0.03	(3.6 ± 0.4) 10^{-5}	(-9 ± 4) 10^{-5}	1.1 10^{-5}
1.026 (2.26)	1.82 ± 0.05	(3.9 ± 0.6)10^{-5}	(0.02 ± 2) 10^{-4}	9.8 10^{-5}
3.63 (8.00)	1.63 ± 0.08	(3.6 ± 0.8) 10^{-6}	(9 ± 6) 10^{-6}	1.6 10^{-6}
4.08 (9.00)	1.8 ± 0.2	(2 ± 1) 10^{-6}	(-0.2 ± 1) 10^{-5}	3.6 10^{-6}
4.54 (10.00)	1.6 ± 0.2	(3 ± 1) 10^{-6}	(9 ± 9) 10^{-6}	2.2 10^{-6}

Table 9 – Polynomial fit parameters found for simulations with singularity-removed definition of the solid angle for a L=17 lattice using only odd values of M.

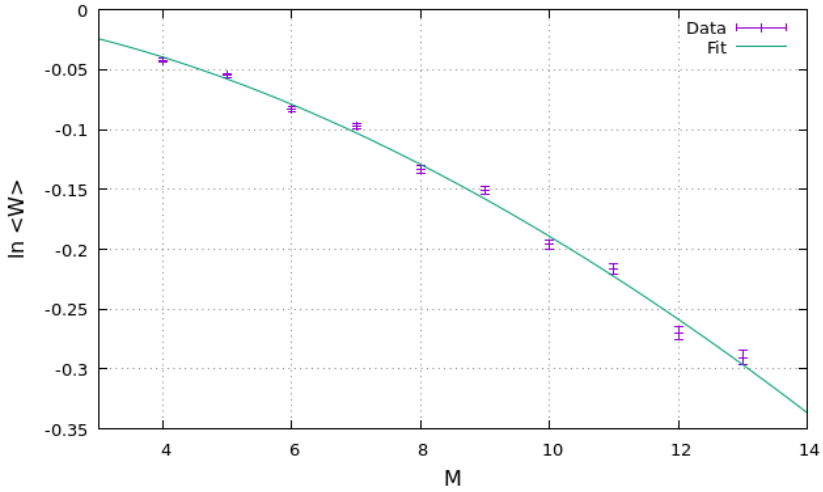

Figure 38 – Polynomial fit for Wilson loop averages in the solid angle picture. $L = 17$ and $T = 0.10 \approx 0.045T_c$

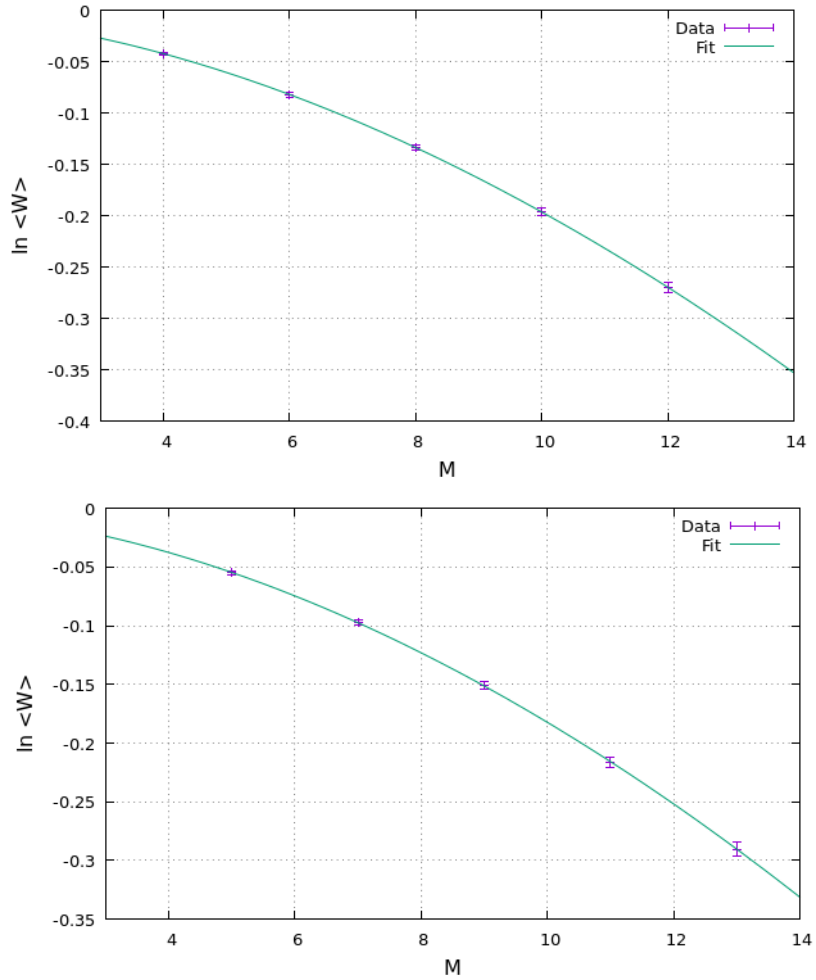

Figure 39 – Polynomial fit for Wilson loop averages in the solid angle picture using only even (above) and odd (below) values of M. $L = 17$ and $T = 0.10 \approx 0.045T_c$

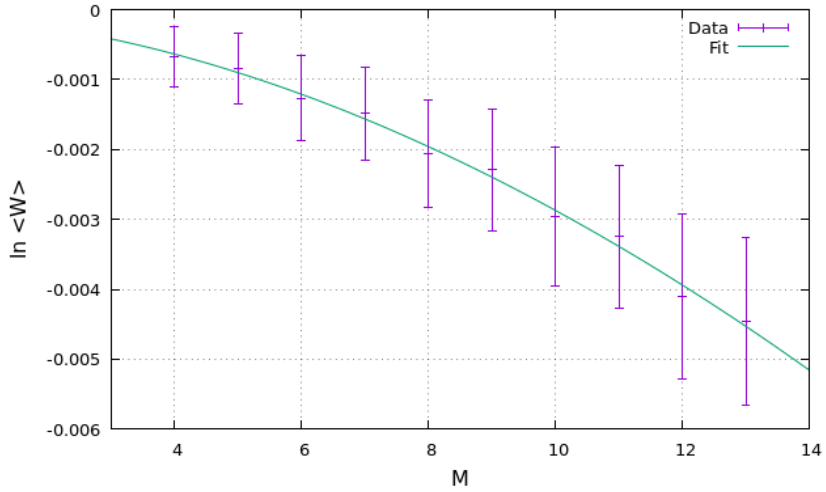

Figure 40 – Polynomial fit for Wilson loop averages in the solid angle picture. $L = 17$ and $T = 2.21 \approx 1.0032T_c$

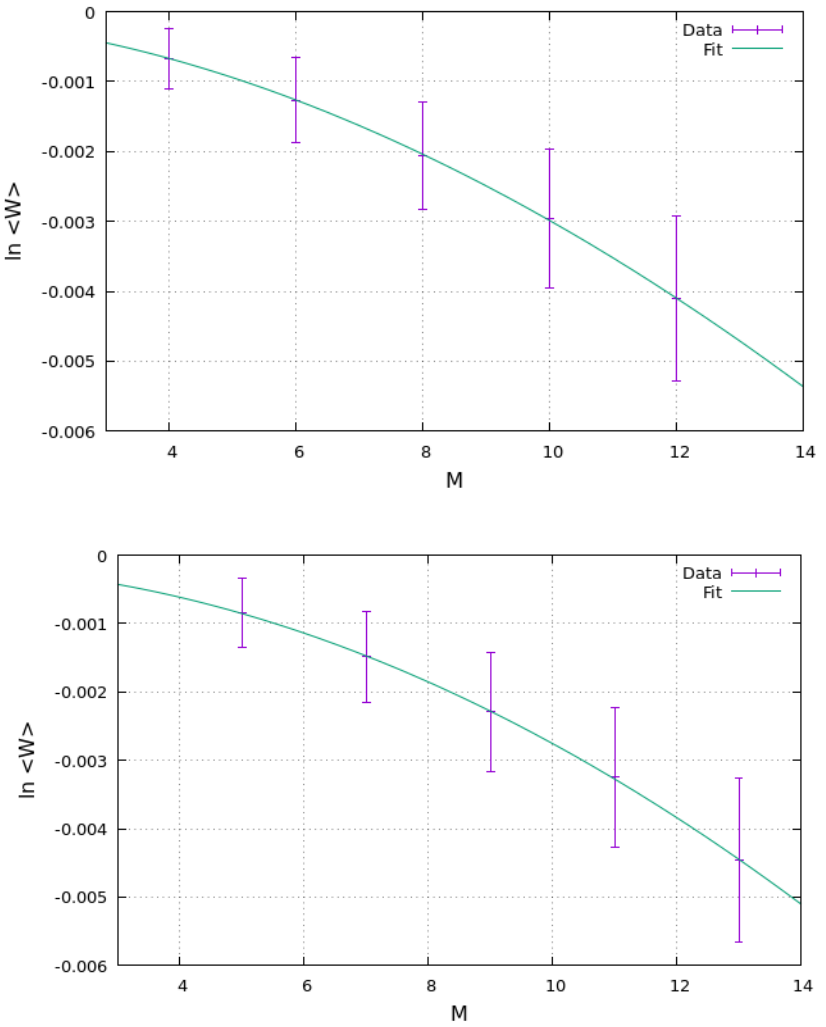

Figure 41 – Polynomial fit for Wilson loop averages in the solid angle picture using only even (above) and odd (below) values of M. $L = 17$ and $T = 2.21 \approx 1.0032T_c$

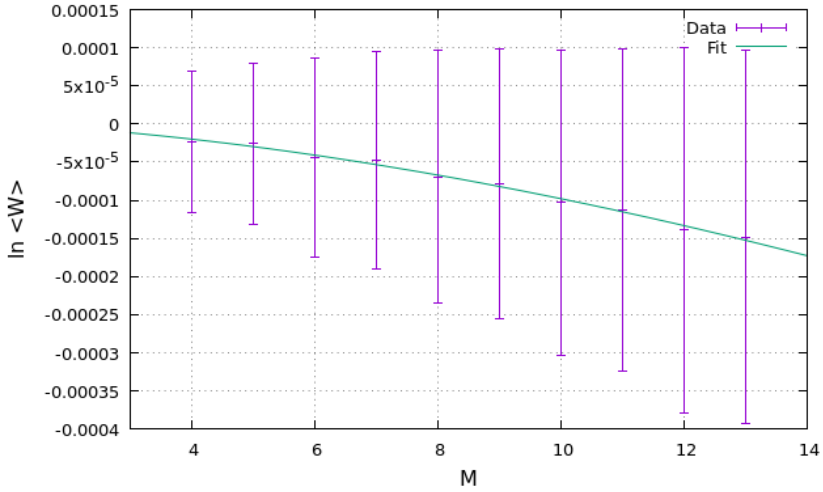

Figure 42 – Polynomial fit for Wilson loop averages in the solid angle picture. $L = 17$ and $T = 10.0 \approx 4.54T_c$

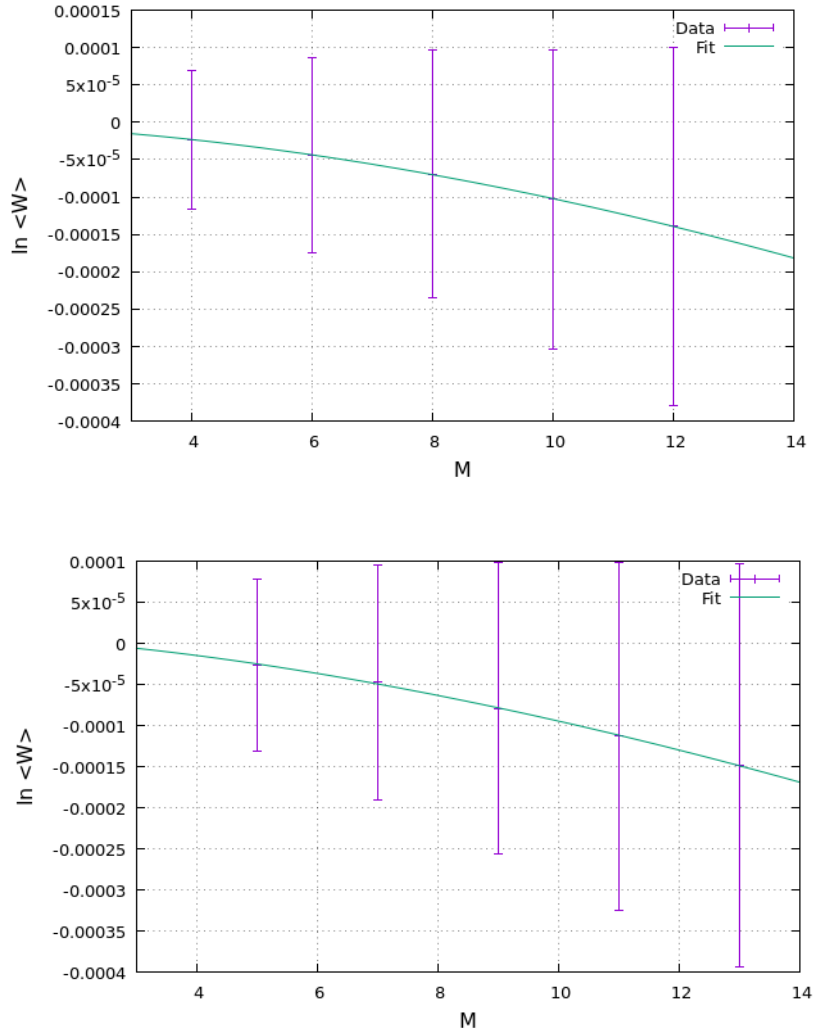

Figure 43 – Polynomial fit for Wilson loop averages in the solid angle picture using only even (above) and odd (below) values of M. $L = 17$ and $T = 10.0 \approx 4.54T_c$

The first conclusion that can be drawn from table 6 is that a perimeter law seems to be the correct behavior for the zero circulation frustration. There it can also be seen that the simulation results are hampered by errors, so that almost all of the σ_γ coefficients are consistent with zero. The fits of the data produced also have big rms errors. This stems from the fact that this implementation does not have the multivaluedness property, thus the linking number averages in the ensemble are not well represented.

As for the case of the multivalued frustration, one can perceive similarities between table 7 and tables 3 and 4. The first one of them is that an area-law appears to be the correct behavior for Wilson loop averages for all temperatures. Another similarity is that the b_γ coefficients are all consistent with zero within the errors. In the present case, for some temperatures, the errors are two orders of magnitude bigger that the value of b_γ itself. Another similarity comes from the fits: the error bars increase with temperature, they almost bury the data for $T = 10.0$, as seen in figs. 42 and 43. It is also seen that the γ values are practically constant. Moreover, one can see that the values found for σ_γ in the present case are consistent to the ones found in the last section within the errors. However, these are too big in the latter case to inequivocally state an equality.

These errors in the fits can be explained by the fact the 'singularity' removal procedure works differently depending on M being even or odd. This is evidenced more clearly in fig. 38, where the data points for odd M are always above the fit curve and the ones for even M are always below it. Such effect is also present in figs. 40 and 42 more subtly. This motivates one to perform fits for these two sets separately. The data is found in tables 8 and 9 and some of the corresponding plots are in figs. 39, 41 and 43.

Thus one can perceive that fits that stem from even values of M have an almost constant γ for all temperatures, except for the anomalous case of $T = 9.00 \approx 4.08 T_c$. In general, the γ values are close to the ones in table 7, but with smaller error. The fit rms error is found to decrease, the σ_γ are a bit altered, but most of the values of σ_γ remain consistent with the surface-concentrated case and less b_γ's are consistent with zero.

In the case of odd values of M, the rms errors also diminish in comparison with the data in table 7, so that the plots are as good as the ones in 8. However, the γ values are much closer to an area-law, specially near the critical temperature, which is the region of interest. For high temperatures it also happens that γ's are smaller than the corresponding values in tables 7 and 8. In this case, one also finds that most of the b_γ values are not consistent with zero.

In contrast to the non minimal surface-concentrated frustration, these results give hope that the essential topological aspects of the ensemble of closed line-like objects are being well captured by the Monte Carlo methods used. They are also very non-trivial, because, also in contrast with the previous analysis, even though there is no drastic surface area information contained in the solid angle frustration, an area law still appears.

6 Final Remarks

Using a numerical approach, effective models of center vortices were analyzed. There is number of evidence stemming from lattice QCD that these degrees of freedom are responsible for the confinement property, which is probed by Wilson loop averages. In general, if this quantity has an area law, confinement arises, if not, there is a perimeter law. In four dimensions, these field configurations are concentrated in closed surfaces and are defined by the fact that they give a center element of the gauge group if they link the Wilson loop. Using the maximal center gauge and the center projection procedure, one is able to deduce that these vortices give a significant contribution to the string tension, even giving almost the full contribution in the case of $SU(2)$.

This *center dominance* motivated further investigations by the Tübingen group, which used a gradient expansion of Yang-Mills action to derive an effective action in which terms that depend on the vortex area and curvature. Using this effective model, they were able to produce a confined and a deconfined region in parameter space reproducing the accepted value for zero temperature string tension. Plus, they built a confinement transition picture in terms of the percolation of the center vortices, gaining intuition about the properties of the random vortex model.

Some other numerical evidence state that there is a certain range in which vortices are correlated, thus leading to interactions. There are also investigations that scrutinize the dependence of the string tension on the representation of the gauge group. These conclude that Casimir scaling is the right dependence at intermediate distances. Also in this context, at larger separations, where it is energetically favorable for gluons to screen the source to produce a gluelump state, there is still some debate on whether the correct behavior for the asymptotic string tension is the Casimir or the Sine Law.

With these thoughts in mind, the authors of ref. [58] built an effective model of center vortices in three dimensions considering an ensemble of line-like objects that obey an action that has both length, curvature and contact interaction costs. In this context, they translate Wilson loop averages into a ratio of partition functions. Afterwards, a controlled set of highly nontrivial approximations were performed. That includes some path integral identities to e.g. linearize the interaction term, and polymer techniques that enable the derivation of a diffusion-like equation, which is latter solved. Hence they were led to a complex field theory with $U(1)$ gauge symmetry breaking.

Analyzing vacuum fluctuations in this model and making use of a lattice formulation, they obtained that the partition function corresponds to an XY model with geometrically-localized frustration. This frustration is chosen to lie between those links that pierce the

minimal area of the Wilson loop $\mathcal{S}_m(\mathcal{C})$. The Wilson loop average is then obtained from the ratio between this partition function and its unfrustrated counterpart.

The continuum limit of this model is expected to be obtained close to the critical coupling of the unfrustrated XY-model, whose most accepted value is $\beta_c \approx 0.454 \approx 1/2.203$. A perimeter and an area law were then found for the high temperature and near-critical regimes, respectively. This is done with the aid of the Villain approximation, which consists to approximate $e^{\beta \cos\theta}$ by a sum of infinite Gaussians centered in its maxima. Following these steps, the authors were led to a sine square dependence on the representation. However, this might change in future works, after the consideration of the important property of center vortex branching.

In this dissertation, as an alternative to grasp information from the effective model the solid angle picture was defined. It exploits the fact that the solid angle subtended by the loop is multivalued when one winds around it and that, near the critical temperature, the relevant information about the effective model is only enconded in the circulation of the frustration.

Then, the Metropolis Algorithm was described as a way to produce a stochastic process that leads the system to the equilibrium distribution, where one can take thermal averages. In short, it makes local updates to the system, always accepting the ones that lower the energy. in addition, configurations that raise the energy are accepted with a probability that is given by the ratio of the equilibrium distribution.

In the path to equilibrium, however, the system passes through intermediate, or transient states. If these are taken in consideration, the error gets greatly enhanced by a factor proportional to the squared root of the relaxation time. This problem is particularly severe when one has second order phase transitions, where the latter quantity is found to diverge in the continuum limit for the order parameter. This characterizes the so-called critical slowing down. Hence, when taking averages, these transient states should be discarded. A solution to this problem is expected to be given by the Wolff algorithm, which performs non-local updates to the system.

Then a method to obtain the critical temperature was described. It relies in the behavior of the fourth-order cumulant, that remains practically constant when the correlation length of the system diverges. Following these lines, a value of 2.13 ± 0.86 was obtained for the critical temperature, which is within the most accepted value by 3%.

Next, we discussed the method used to calculate the partition function ratios. It makes use of the fact that the Helmholtz free energy is a logarithmic measure of the partition function. Then, if the two systems have the same degrees of freedom, the partition function ratio can be measured as the average between Boltzmann weights taken in one of the systems. In the present context, the latter system is the unfrustrated one. This is

only valid when both systems are "similar", thus avoiding the overlap problem, where the averages are exponentially suppressed. To mitigate this, one may take the averages in steps, so that the partition function ratio becomes the product of intermediate systems' partition function ratios, the intermediate systems being chosen so that they interpolate between the two original systems.

Following this numerical procedures, the correlation time was analyzed. In particular, we found that the highest ones, as expected, those near the critical temperature, are in the order of $\sim 10^3$ for a $L = 11$ lattice. The frustrated and unfrustrated models indeed behave similarly in this region. This is in contrast to low temperature regime, where the two systems behave differently in terms of magnetization, although they are not that different in terms of energy.

The obtained Wilson loop has a much smaller correlation time than the magnetization, which is expected as the latter is the order parameter. The computation showed that it is incresingly difficult to grasp information from the partition function ratios as the temperature rises. This happens due to the fact that the Wilson loop values with growing loop size at a constant temperature get squeezed together in values ~ 1 in that case. Then, as foreseen, the area law is shown to be the correct behavior of the Wilson loop averages with the size of the loop. But this area law seems to persist even at temperatures where a perimeter law should appear.

Then, the representation dependence of the area law coefficient was analyzed, and the result of eq. (3.44) was confirmed with maximum 2% discrepancy in comparison with the sine-square law fit parameters. Moreover, for the N-ality 1 representations we obtained a constant ratio $\sigma_A^N(1)/\sin^2\frac{\pi}{N} \approx 2.038\ 10^{-4}$, for $L = 11$.

Next, it is argued in a XY-model-level that Wilson loop averages should not depend on the surface on which the frustration is placed, which is in consonance with the effective model, that has only linking number information. Nevertheless, the numerical results found reflect a surface-dependence behavior, which persists even when one uses the intermediate step method described in the end of section 4.4. A possible solution to this issue might be to use a numerical method that takes topology into account.

The results concerning the solid angle picture give evidence that an area law can also arise in this context. This comes after a cautious implementation, which is made so that the multivaluedness of the solid angle is preserved without the appearance of big solid angle differences that produce a growth area law. This is done by diminishing the module of $|\Delta_\mu \chi|$ for points that either pierce the Wilson loop outside of it, in its borders (for odd values of M) or that are near the boundary of the lattice.

Nevertheless, this "singularity" removal procedure works differently for odd and even values of M. If taken together, the fits are consistent with an area law within the

errors near the critical temperature. Furthermore the σ_γ values agree with the ones in the concentrated frustration picture within the error bars but these are so big in the solid angle analysis that calling it a equality is misleading. This can be explained by the fact that the points associated with odd (even) values of M are always above (below) the fitting curve. This implies that two behaviors compete. For even M values, the polynomial fit parameter γ is almost constant with temperature within the errors, with values that are almost the same as the ones with both types of values. As for odd M values, it is seen that the area law is more evident. This is even more noticeable near the critical temperature.

These results enhance our confidence in the partition function ratio method as a tool to probe the topological aspects of the frustrated XY-model and thus of the center vortex effective model. This is because an area law appears in a case where the frustration is diluted in space and not concentrated in a privileged surface. Furthermore, a perimeter law arises if one performs simulations with a circulationless frustration.

To improve the results in future works, the Wolff algorithm should be used, because it solves the critical slowing down problem. A more thorough analysis of the non-minimal surface is also needed, maybe with the use of another sampling method, one that takes topology into account so that the surface independence arises. The representation dependence of the string tension in the context of the surface-concentrated frustration should be complemented to see what is the behavior of the ratio $\sigma_A^N(1)/\sin^2\frac{\pi}{N}$ for other lattice sizes. Moreover, this representation dependence should also be analyzed in the solid angle picture. Finally, the methods developed in this dissertation might also be used in the effective model that arises when the branching property of center vortices is taken into account.

,

Appendix

APPENDIX A – Lattice QCD

A.1 The Wilson Action

As many of the results presented in the introduction depend on the Lattice QCD formalism, it is worth making a brief incursion in the subject. Firstly one is reminded that the continuum QCD action is

$$S[\psi,\bar{\psi},A] = S_F[\psi,\bar{\psi},A] + S_C[A] \text{ with} \tag{A.1}$$

$$S_F[\psi,\bar{\psi},A] = \sum_{s=1}^{N_s}\int d^4x\ \bar{\psi}^{(s)}(x)(i\not{D}+m^{(s)})\psi^{(s)}(x). \tag{A.2}$$

$$S_C[A] = \frac{1}{2g^2}\int d^4x\ \mathrm{tr}[F_{\mu\nu}(x)F_{\mu\nu}(x)]\ ^{1} \tag{A.3}$$

where the $\psi^{(s)}(x)$ is the s flavor fermion field; $\not{D} = \gamma_\mu D_\mu\ ^{2} = \gamma_\mu(\partial_\mu + iA_\mu)$; A_μ is the gauge field; $F_{\mu\nu} = -i[D_\mu, D_\nu] = \partial_\mu A_\nu - \partial_\nu A_\mu + i[A_\mu, A_\nu]$; and the γ_μ's obey the Euclidean anticomutators

$$\{\gamma_\mu,\gamma_\nu\} = 2\delta_{\mu\nu}\mathbb{1}. \tag{A.4}$$

Explicitly, the euclidean Weyl representation of the γ's is

$$\gamma_0 = \begin{pmatrix}\mathbf{0} & \mathbb{1}\\ \mathbb{1} & \mathbf{0}\end{pmatrix}, \gamma_i = \begin{pmatrix}\mathbf{0} & -i\sigma_i\\ i\sigma_i & \mathbf{0}\end{pmatrix}\ . \tag{A.5}$$

The action (A.1) is invariant under the gauge transformation

$$\begin{aligned}\psi(x)\mapsto\psi'(x) = \Omega(x)\psi(x)\ ,\bar{\psi}(x)\mapsto\bar{\psi}'(x) = \bar{\psi}(x)\Omega^\dagger(x),\\ A(x)\mapsto A'(x) = \Omega(x)A_\mu(x)\Omega^\dagger(x) + i(\partial_\mu\Omega(x))\Omega^\dagger(x).\end{aligned} \tag{A.6}$$

One way to motivate the Wilson action, the pioneer and most celebrated in this context, follows almost the same principles of the continuum: it is imposed that the naive discretization of free fermion action becomes invariant under local gauge transformations, namely

$$S_F^0 = a^4\sum_x\bar{\psi}(x)\left(\sum_{\mu=0}^{3}\gamma_\mu\frac{\psi(x+\hat{\mu})-\psi(x-\bar{\mu})}{2a} + m\psi(x)\right). \tag{A.7}$$

where $\psi(x)$ is now the lattice fermion field ; and a is the lattice spacing.

[1] The extra factor is a convenient form to introduce the coupling constant. To recover a form which is more QED relatable one might take the prescription $(1/g)A_\mu \mapsto A_\mu$

[2] Euclidean signature is implied

One way to introduce the gauge fields, even in the continuum is to ask that (A.7) is invariant by the gauge transformations

$$\psi(x) \mapsto \psi'(x) = \Omega(x)\psi(x)\ , \bar{\psi}(x) \mapsto \bar{\psi}'(x) = \bar{\psi}(x)\Omega^{\dagger}(x), \tag{A.8}$$

where the $\Omega(x) \in SU(N)$, in general. From that it is already possible to see that the $\bar{\psi}(x)\psi(x+\hat{\mu})$ term, that appears because of the discretization of the derivative, is not invariant. Thus, what one may fix it is, instead of introducing a covariant derivative as in the continuum, is to introduce a operator $U_{\mu}(x)$ such that

$$\bar{\psi}(x)U_{\mu}(x)\psi(x+\hat{\mu}) \mapsto \bar{\psi}(x)\Omega^{\dagger}(x)U'_{\mu}(x)\Omega(x+\hat{\mu})\psi(x+\hat{\mu}) \tag{A.9}$$

These are the so-called *link variables*. Hence one asks that $U_{\mu}(x)$ transforms as

$$U'_{\mu}(x) \mapsto U'_{\mu}(x) = \Omega(x)U'_{\mu}(x)\Omega^{\dagger}(x+\hat{\mu}) \tag{A.10}$$

Besides that, one also imposes that $U_{\mu}(x) \in SU(3)$. Notice that the matrices obey

$$U_{-\mu}(x) = U^{\dagger}_{\mu}(x-\hat{\mu}) \tag{A.11}$$

$$U_{-\mu}(x) \mapsto U'_{-\mu}(x) = \Omega(x)U'_{-\mu}(x)\Omega^{\dagger}(x-\hat{\mu}). \tag{A.12}$$

then the naïve discretization of the fermonic action is

$$S_F = a^4 \sum_n \bar{\psi}(x) \left(\sum_{\mu=1}^{3} \gamma_{\mu} \frac{U_{\mu}(x)\psi(x+\hat{\mu}) - U_{-\mu}(x)\psi(x-\hat{\mu})}{2a} + m\psi(x) \right) . \tag{A.13}$$

Even with this connection, (A.13) is not the final word for the description of fermions in Lattice Gauge Theory, as this suffers with the presence of the infamous *doublers* in the lattice propagators. However we will not approach this in the present text, and the reader is referred to ref. [32].

The continuum quantity related to $U'_{\mu}(x)$ is the gauge transporter

$$G(x,y) = P \exp\left(i \int_{\mathcal{C}_{xy}} A_{\mu} ds_{\mu} \right) \tag{A.14}$$

where P denotes the path-ordering prescription that puts to the left the operators associated which appear latter when one follows the trajectory $\mathcal{C}_{xy}$ [60]. It transforms as

$$G(x,y) \mapsto G'(x,y) = \Omega(x)G(x,y)\Omega^{\dagger}(y) \tag{A.15}$$

Following these lines, the continuum action can be recovered by taking a first-order expansion of (A.13) on the lattice spacing. In fact, writting

$$U_{\mu}(x) = e^{iaA\mu(x)} + \mathcal{O}(a^2) = \mathbb{1} + iaA_{\mu}(x) + \mathcal{O}(a^2) \tag{A.16}$$

$$U_{-\mu}(x) = e^{-iaA\mu(x-\hat{\mu})} + \mathcal{O}(a^2) = \mathbb{1} - iaA_{\mu}(x-\hat{\mu}) + \mathcal{O}(a^2), \tag{A.17}$$

$$\begin{aligned}\frac{U_\mu(x)\psi(x+\hat{\mu})-U_{-\mu}(x)\psi(x-\hat{\mu})}{2a} &\mapsto \frac{\psi(x+\hat{\mu})-\psi(x-\hat{\mu})}{2a}\\ &+\frac{iA_\mu(x)\psi(x+\hat{\mu})+iA_\mu(x-\hat{\mu})\psi(x-\hat{\mu})}{2}\\ &=\partial_\mu\psi(x)+iA_\mu(x)+\mathcal{O}(a)\end{aligned} \tag{A.18}$$

Now, to construct the pure-gauge part of the action, one must exclusively use the link variables to define a gauge invariant quantity that reduces to (A.3) in the naïve continuum limit. Hence, let $\mathcal{C}$ a path joining the points n_0 and n_1, defining

$$P[U] \equiv \prod_{(x,\mu)\in\mathcal{C}} U_\mu(x)\ , \tag{A.19}$$

it is readily seen from (A.10) that only the Ω associated with the extreme points do not cancel. Thus a way to build a gauge invariant quantity is to take $\mathcal{C}$ in (A.19) as a closed loop, hereafter denoted by $\mathcal{F}$, and to take the trace of the resulting operator, namely,

$$L[U] \equiv \mathrm{tr}\left[\prod_{(x,\mu)\in\mathcal{F}} U_\mu(x)\right]\ . \tag{A.20}$$

A particular form of (A.20) is when $\mathcal{F}$ is the elementary square formed by the points $\{n, n+\mu, n+\mu+\nu, n+\nu\}$, the *plaquette*. In this case,

$$\mathbb{U}_{\mu\nu} \equiv U_\mu(x)U_\nu(x+\mu)U_{-\mu}(x+\mu+\nu)U_{-\nu}(x+\nu) = U_\mu(x)U_\nu(x+\mu)U_\mu^\dagger(x+\nu)U_\nu^\dagger(x)\ . \tag{A.21}$$

With (A.21) in mind it is possible to infer that

$$S_C[U] = \frac{2}{g^2}\sum_{n,\mu<\nu}\mathrm{Re}\ \ \mathrm{tr}\left(\mathbb{1}-\mathbb{U}_{\mu\nu}(x)\right)\ . \tag{A.22}$$

As a matter of fact, taking the naïve limit $a\to 0$ again,

$$\mathbb{U}_{\mu\nu}(x) \approx e^{iaA_\mu(x)}e^{iaA_\nu(x+\mu)}e^{-iaA_\mu(x+\nu)}e^{-iaA_\nu(x)} \tag{A.23}$$

Using Haussdorf-Baker-Campbell equation,

$$e^Ae^B = e^{A+B+\frac{1}{2}[A,B]+\ldots}, \tag{A.24}$$

and that $A_\nu(x+\mu)\approx A_\nu(x)+a\ \partial_\nu A_\mu(x)$,

$$U_{\mu\nu} \approx \exp\left[ia^2\left(\partial_\mu A_\nu(x)-\partial_\nu A_\mu(x)+i[A_\mu(x),A_\nu(x)]\right)\right] = e^{ia^2F_{\mu\nu}(x)} \tag{A.25}$$

and expanding in a in lowest order [3]

$$S_C[U] \approx \frac{a^4}{2g^2}\sum_{n,\mu<\nu}\mathrm{tr}[F_{\mu\nu}^2(x)] \tag{A.26}$$

[3] which is $\mathcal{O}(a^4)$, given that $\mathcal{O}(a^2)$ terms cancel each other when one takes the real part of the trace.

and as $a^4 \sum \mapsto \int d^4x$ the classical pure gauge action is recovered.

It must be emphasized that this is absolutely not the only possible discretization of QCD action, even without fermions. Throughout the years, many other possible actions have emerged. A common motivation to these developments is the reduction of finite lattice artifacts so that the continuum properties of observables can be calculated with bigger lattice spacings. One example of such actions is the 1-loop-improved action, which follows a general program to arbitrary lattice field theories, which were proposed in refs. [67, 68].

A.2 Euclidean Correlators

The objective in this section is to show a result that is very important to the interpretation of Lattice Field Theory computations. This is done exploiting the relation between periodic Euclidean time and thermal averages [17]. Thus, consider the correlation function between two operators in euclidean time

$$\langle \hat{O}_2(t_0)\hat{O}_1(0)\rangle_t = \frac{1}{Z_t}\mathrm{tr}\left[e^{-(t-t_0)\hat{H}}\hat{O}_2 e^{-t_0\hat{H}}\hat{O}_1\right] . \tag{A.27}$$

One thing to be noted in the equation above: this is an average of a product of operators, one of them evolving in euclidean Heisenberg picture and with an thermal factor e^{-Ht} whose "inverse temperature" t will be taken to be infinite. Furthermore,

$$Z_t = \mathrm{tr}[e^{-Ht}] , \tag{A.28}$$

Performing the averages in the eigenvectors of the Hamiltonian,

$$H|n\rangle = E_n|n\rangle \ , n = 0, 1, 2... \tag{A.29}$$

$$E_i < E_j \text{ se } i < j , \tag{A.30}$$

$$Z_t = \sum_n \langle n|e^{-\hat{H}t}|n\rangle = \sum_n e^{-E_n t} \ , \text{ and} \tag{A.31}$$

$$\langle \hat{O}_2(t_0)\hat{O}_1(0)\rangle_t = \frac{1}{Z_t}\sum_{m,n} e^{-E_m(t-\tau_0)}\langle m|\hat{O}_2|n\rangle e^{-E_n t_0}\langle n|\hat{O}_1|m\rangle . \tag{A.32}$$

Multiplying (A.32) both in the numerator and the denominator by $e^{E_0 t}$,

$$\langle \hat{O}_2(t_0)\hat{O}_1(0)\rangle_t = \frac{\sum_{m,n} e^{-\delta E_m(t-\tau_0)}\langle m|\hat{O}_2|n\rangle e^{-\delta E_n t_0}\langle n|\hat{O}_1|m\rangle}{1+\sum_{n>0} e^{-\delta E_n t}} \tag{A.33}$$

$$\delta E_i = E_i - E_0 .$$

Now one may take $t \to \infty$. From (A.30), it is readily seen that only the $m = 0$ term survives. Defining the reference of energy such that $E_0 = 0$,

$$\lim_{t\to\infty}\langle \hat{O}_2(t_0)\hat{O}_1(0)\rangle_t = \sum_n \langle 0|\hat{O}_2|n\rangle\langle n|\hat{O}_1|0\rangle e^{-E_n t_0} . \tag{A.34}$$

Let us now consider, for instance, that $\hat{O}_2 = \hat{\psi}_p$ and $\hat{O}_1 = \hat{\psi}_p^\dagger$ are respectively the anihilation and creation operator for a proton. Hence,

$$\lim_{t\to\infty} \langle \hat{\psi}_p(t_0)\hat{\psi}_p^\dagger(0)\rangle_t = \sum_n |\langle 0|\hat{\psi}_p^\dagger|n\rangle|^2 e^{-E_n t_0} \ , \tag{A.35}$$

where the "surviving" states $|n\rangle$ are those that have the quantum numbers of one proton. For a sufficiently big t_0 the first term of (A.35) dominates. It is thus possible to extract the lowest energy state of one proton by studying the assymptotic behavior of the correlation function. It is also possible to obtain the information contained in $|\langle 0|\hat{\psi}_p^\dagger|n\rangle|^2$

To complete the connexion, in lattice simulations one computes (A.27) by calculating the functional integral

$$\langle \hat{O}_2(t_0)\hat{O}_1(0)\rangle_t = \frac{1}{Z_E^{\text{rede}}} \int [\mathcal{D}U]\ e^{-S_E[U]}\ O_2[U(t_0,\mathbf{x})]O_1[U(0,\mathbf{x})] \ . \tag{A.36}$$

using Monte Carlo techniques. To this end, it is necessary to define a group invariant integration measure $[\mathcal{D}U]$.

A.3 The Haar measure and examples of integrals in SU(3)

With a gauge invariant lattice action $S_C[U]$ defined, if one is to make some sense out of the quantum field theory with these degrees of freedom, it is also reasonable to ask the same for the partition function,

$$Z_C = \int [\mathcal{D}U]\ e^{-S_C[U]} \tag{A.37}$$

To this end one needs to define a integral measure that is invariant under the gauge group, so

$$[\mathcal{D}U'] = [\mathcal{D}U] \Rightarrow \prod_{n,\mu} dU'_\mu(x) = \prod_{n,\mu} dU_\mu(x). \tag{A.38}$$

from which one deduces

$$dU'_\mu(x) = dU_\mu(x) \Rightarrow d(\Omega(x)U_\mu(x)\Omega^\dagger(x+\hat{\mu})) = dU_\mu(x) \ . \tag{A.39}$$

As it is possible to choose $\Omega(x)$ and $\Omega(x+\hat{\mu}) \in SU(N)$ independently, the measure to be defined must be invariant both by left and right multiplication by an element of $SU(N)$,

$$dU = d(UV) = d(VU). \tag{A.40}$$

Together with the normalization condition,

$$\int dU = 1 \tag{A.41}$$

it constitutes one of the defining properties of the *Haar measure*.

Similar conditions can be defined to any *compact Lie group*. To such sets, it is convenient to write a generic element as

$$U(\omega) = \exp\left(i\sum_{k=1}^{M}\omega_k T_k\right) . \tag{A.42}$$

Where the ω_k are real parameters belonging to a limited and closed set; the T_k are called the generators of the Lie group, and for $SU(N)$, these are $N\times N$ hermitian, null trace matrices. They also obey $\mathrm{tr}[T_jT_k] = (1/2)\delta_{jk}$ and the comutation relations $[T_i, T_j] = if_{ijk}T_k$. The f_{ijk} are called the *structure constants*. It is possible then to show that linear combinations of the generators form a Lie algebra. For $SU(N)$, this is a N^2-1 dimensional vector space denoted by $su(N)$.

One way to explictly construct a Haar measure is to first realize that

$$M_k(\omega) = i\frac{\partial U(\omega)}{\partial\omega_k}U^{-1}(\omega) \tag{A.43}$$

belongs to the associated Lie algebra for all ω. To this end, M must be hermitian and have a null trace. The hermiticity follows from the fact that $U(\omega)$ is unitary,

$$U(\omega)U^\dagger(\omega) = \mathbb{1} \Rightarrow \frac{\partial U(\omega)}{\partial\omega_k}U^\dagger(\omega) + U(\omega)\frac{\partial U^\dagger(\omega)}{\partial\omega_k} = 0, \tag{A.44}$$

from which one deduces

$$M_k^\dagger(\omega) = -iU(\omega)\frac{\partial U^\dagger(\omega)}{\partial\omega_k} = i\frac{\partial U(\omega)}{\partial\omega_k}U^\dagger(\omega) = M_k^\dagger(\omega). \tag{A.45}$$

As for the trace nullity, this follows from the fact that $\det U(\omega) = 1$

$$\begin{aligned}\det U(\omega) = 1 \Rightarrow 0 &= \frac{\partial\det U(\omega)}{\partial\omega_k} = \frac{\partial\det U(\omega)}{\partial U_{ab}}\frac{\partial U_{ab}(\omega)}{\partial\omega_k}\\ &= \det U(\omega)\ U^{-1}_{ba}(\omega)\frac{\partial U_{ab}(\omega)}{\partial\omega_k} = \mathrm{tr}\left(U^{-1}(\omega)\frac{\partial U(\omega)}{\partial\omega_k}\right),\end{aligned} \tag{A.46}$$

hence, $M_k(\omega)\in su(N)$.

One defines the group metric from $M_k(\omega)$ as being

$$\begin{aligned}ds^2 &\equiv g(\omega)_{mn}d\omega_m d\omega_n\\ g(\omega)_{mn} &\equiv \mathrm{tr}[M_m(\omega)M_n^\dagger(\omega)] = \mathrm{tr}\left[i\frac{\partial U(\omega)}{\partial\omega_m}U^{-1}(\omega)\left(i\frac{\partial U(\omega)}{\partial\omega_n}U^{-1}(\omega)\right)^\dagger\right] = \mathrm{tr}\left[\frac{\partial U(\omega)}{\partial\omega_m}\frac{\partial U^\dagger(\omega)}{\partial\omega_n}\right],\end{aligned} \tag{A.47}$$

where in the last equality it is used that $U^\dagger U = U^{-1}(U^{-1})^\dagger = \mathbb{1}$. Then the integral measure is defined as

$$dU = \nu\sqrt{\det[g(\omega)]}\prod_k d\omega_k . \tag{A.48}$$

where ν is a normalization constant that can be obtained from the normalization condition (A.41). For instance for $N = 2$, where

$$U(\theta) = e^{i(\sigma\cdot\hat{n})\theta} = \cos\theta\mathbb{1} + i(\sigma\cdot\hat{n})\sin\theta, \tag{A.49}$$

σ_i $i = 1, 2, 3$ being the Pauli matrices, and $\hat{n}\cdot\hat{n} = 1$,

$$dU = \sin^2\theta \frac{d\theta}{\pi}\frac{d^2\hat{n}}{4\pi} \ . \tag{A.50}$$

To check that (A.40) is obeyed by (A.48), let $W(\eta)$ be the matrix obtained from $U(\omega)$ by taking the product of a arbitrary member of the group,

$$W(\eta) = VU(\omega) \ . \tag{A.51}$$

Thence, the paremeters $\eta = \{\eta_1, \eta_2, ..., \eta_M\}$ and $\omega = \{\omega_1, \omega_2, ..., \omega_M\}$ are related to each other by some function, so that $\eta = \eta(\omega)$. From multi-variable calculus it is known that

$$\begin{aligned} \prod_k d\eta_k &= \det[J]\prod_k d\omega_k \\ J_{kl} = \frac{\partial\eta_k}{\partial\omega_l} \ \text{e} \ (J^{-1})_{kl} &= \frac{\partial\omega_k}{\partial\eta_l} \end{aligned} \tag{A.52}$$

thus the metric (A.47) becomes

$$\begin{aligned} \tilde{g}(\eta)_{mn} &= \text{tr}\left[\frac{\partial W(\eta)}{\partial\eta_m}\frac{\partial W^\dagger(\eta)}{\partial\eta_n}\right] = \text{tr}\left[\frac{\partial W(\omega)}{\partial\omega_i}\frac{\partial W^\dagger(\omega)}{\partial\omega_j}\right]\frac{\partial\omega_i}{\partial\eta_m}\frac{\partial\omega_j}{\partial\eta_n} \\ &= \text{tr}\left[V\frac{\partial U(\omega)}{\partial\omega_i}\frac{\partial U^\dagger(\omega)}{\partial\omega_j}V^\dagger\right](J^{-1})_{im}(J^{-1})_{jn} = \text{tr}\left[\frac{\partial U(\omega)}{\partial\omega_i}\frac{\partial U^\dagger(\omega)}{\partial\omega_j}\right](J^{-1})_{im}(J^{-1})_{jn} \ . \end{aligned} \tag{A.53}$$

From the penultimate to the last expression it was used the cyclic property of the trace as well as $V^\dagger V = \mathbb{1}$. From that,

$$\tilde{g}(\eta) = (J^{-1})^T g(\omega) J^{-1}, \tag{A.54}$$

which finally results in

$$\begin{aligned} dW(\eta) &= \nu\sqrt{\det[g(\omega)]}\ \det[J^{-1}]\prod_k d\eta_k = \nu\sqrt{\det[g(\omega)]}\ \det[J^{-1}]\det[J]\prod_k d\omega_k \\ &= \nu\sqrt{\det[g(\eta)]}\prod_k d\omega_k = dU(\omega), \end{aligned} \tag{A.55}$$

that is exactly what one wanted to demonstrate.

A.4 Examples of integrals in SU(3)

In the previous section a integral measure that gives a more precise sense to "sum over all group degrees of freedom". Now it is worth giving some examples of such integrals in $SU(3)$ which are useful to strong coupling expansion average of the Wilson loop seen in section 1.2. All the examples below refer to fundamental representation entries U_{ab}, namely,

$$\int dU\ U_{ab} = 0, \tag{A.56}$$

$$\int dU\ U_{ab}U_{cd} = 0, \tag{A.57}$$

$$\int dU\ U_{ab}U^{\dagger}_{cd} = \frac{1}{3}\delta_{ad}\delta_{bc}, \tag{A.58}$$

$$\int dU\ U_{ab}U_{cd}U_{ef} = \frac{1}{6}\epsilon_{ace}\epsilon_{bdf}. \tag{A.59}$$

One way to obtain such equations is to consider a corollary of the metric invariance (A.40), besides the defining properties of $SU(3)$. Such corollary is that

$$\int dU f(U) = \int dU f(UV) = \int dU f(WU) \tag{A.60}$$

for arbitrary $U, W \in SU(3)$. Using this in the left side of (A.56), one gets

$$\int dU\ U_{ab} = V_{ac}\int dU\ U_{cb}, \tag{A.61}$$

however as V is arbitrary, the integral itself must be zero. In particular, one can choose V to be diagonal, and all its elements being different of 1, e.g. $V = e^{i\frac{2\pi}{3}}\mathbb{1}$. So

$$(1 - e^{i\frac{2\pi}{3}})\int dU\ U_{ab} = 0 \Rightarrow \int dU\ U_{ab} = 0. \tag{A.62}$$

A similar argument can be made for (A.57).

Things are more subtle for eqs. (A.58) e (A.59), as there are some constraints whose origin is in the definition of $SU(3)$: unitary matrices whose determinant is 1. Hence, taking $b = c$ in (A.58) and summing in c,

$$\int dU\ U_{ac}U^{\dagger}_{cd} = \int dU\ \delta_{ad} = \delta_{ad}. \tag{A.63}$$

An analogous equation is obtained taking $a = d$ and summing in a. The sum in the left side of (A.63) goes from 1 to 3, and each term of this sum can be obtained from another term by changing columns and rows. This change can be implemented up to a sign by a multiplication by a matrix $C \in SU(3)$, e.g. to change columns 1 and 2, one multiplies the initial matrix by

$$M_3 = -\begin{pmatrix} 0 & 1 & 0 \\ 1 & 0 & 0 \\ 0 & 0 & 1 \end{pmatrix}. \tag{A.64}$$

from the right, to change rows 1 and 2, one uses the above matrix multiplied from the right, thus,

$$\int dU\ U_{a2}U^{\dagger}_{2d} = \int dU\ (UM)_{a1}(MU^{\dagger})_{1a} \tag{A.65}$$

So using (A.60) other matrices analogous to M_3, each term results in the same value, thus implying that $\int dU\ U_{ac}U^{\dagger}_{cd} = (1/3)\delta_{ad}$ (no sum in c implied). Something similar can be shown in the case $a = d$. If $b \neq c$, (A.60) is used again as in the case of (A.56) show that the integral vanishes regardless of either $a = b$ or $a \neq b$.

As for (A.59), one is reminded of the fact that $\det(U) = \epsilon_{abc}U_{a1}U_{b2}U_{c3} = 1$, here such symmetry arguments get very complicated so it is preferable to perform the integrals in a more systematic and general way such as in ref. [16], where diagrams are used to obtain them. In general, what the Haar measure does is to project out the contribution of the integrand to the singlet (or trivial) representation of the group, as the only non-zero results come when the integrand adds up to 1.

APPENDIX B – Random numbers

One might define a Monte Carlo method as any numerical process that uses random number to obtain its results [45]. These numbers might generated by nature, using atmospherical data, electrical noise or even measuring the reflection of individual photons. This type of generation is however not reproducible, sometimes too slow, and one might not assure the promissed probability density is obeyed, and their use is more convenient in cryptography.

Usually in Monte Carlo simulations what one uses is computer algorithms that generate numerical sequences that *appear* to be indistinguishable from random sequences. Thus they are called pseudorandom numbers. The main property to be imitated is the unpredictability: if one is given n true random numbers, he must not be able to predict the $(n+1)$-th from any combination of the previous ones. As the implementations are based on sequences of a limited set of integers, usually defined by the available computer memory, they are periodical. The minimum number of iterations one performs so that the sequence starts to repeat itself is called the *period* of the random number generator.

B.1 The Linear Congruential Method

One of the most simple methods to obtain such sequences is the linear congruential method or LCG [49]. It consists of starting with the choice of a *seed*, the initial number of the sequence, and then one performs iterations of the form

$$r_{i+1} = (ar_i + b) \mod m. \tag{B.1}$$

In table 10, one can see the iterations for some values of a and m

$a = 85$ $m = 256$		$a = 899$ $m = 32768$		$a = 16807$ $m = 4294967295$		$a = 16807$ $m = 2147483647$	
i	r_i	i	r_i	i	r_i	i	r_i
1	27	1	27	1	27	1	27
2	247	2	24273	2	453789	2	453789
3	3	3	30707	3	3331864428	3	1184380782
...	...	...	...	...	...	...	...
63	243	8191	14595	65535	614062173	2147483644	1186718670
64	175	8192	13705	65536	4031499021	2147483645	1500057001
65	27	8193	27	65537	27	2147483646	27
period = 65		period = 8193		period = 65537		period = 2147483646	

Table 10 – Some values obtained through the iteration of (B.1) that defines the LCG

Thus, within the options in this table, the generator $a = 16807$ and $m = 2147483647 = 2^{31} - 1$ is the best option. It leads to a period of length $\tau = 2^{31} - 1$, which is a large number, but becomes really tiny when one considers simulations with a increasing number of lattice sites.

B.2 The Mersenne Twister

As the above mentioned method produces a periodicity that is small for Monte-Carlo applications[1], one needs another procedure to produce the integer sequences. One of the standard recent methods [45, 46] to do so is to refer to the Mersenne Twisters (MT), originally proposed in ref. [53] [2]. The 'Mersenne' part of the name comes from the fact that the periodicity of such method is a Mersenne prime, namely $\tau = 2^{19937} - 1$, which is a number that is even difficult to compare with any astrophysical scale. Thence it has become one of standard generators of pseudorandom numbers when cryptography problems are not involved.

The procedure itself is very intricate, but it can be outlined in a simpler way [73]. As with many other generators, even the LCG itself, MT can be described in terms of states. The random numbers are then extracted from these states, by a 'translation' operation g. The seed of the generator can either be the first state, as it is with the LCG, or it can be used to generate the first state, in the case of MT. Then, one applies a certain transformation T to this first state and then obtains the next one, and so on and so forth, for the desired number of times.

In the case of the MT, each state is a 624-long list of 32-bit integers, whereas in the previous LCG each state was a single 32-bit integer. The actual procedure starts with

[1] In the simulations of the present work, this was reached for 18^3 lattices and 10^5 updates

[2] The algorithm is actually available online as a C code in http://www.math.sci.hiroshima-u.ac.jp/~m-mat/MT/MT2002/CODES/mt19937ar.c.

the recurrence equation [45, 53]

$$x_n = x_{n-q} \oplus x_{n-p+1} \begin{pmatrix} 0 & 0 \\ 0 & \mathbb{1}_m \end{pmatrix} T \oplus x_{n-p} \begin{pmatrix} \mathbb{1}_{w-m} & 0 \\ 0 & 0 \end{pmatrix} T, \qquad . \tag{B.2}$$

Here, each state x_k is a w-bit integer which are to be thought as a row vector, $\mathbb{1}_p$ is the $p \times p$ identity matrix,

$$T = \left(\begin{array}{cc|c} 0 & & \\ \vdots & \mathbb{1}_{w-1} & \\ 0 & & \\ \hline & a & \end{array}\right) \tag{B.3}$$

is the matrix that "twists" the states, and $\oplus$ is the modulo 2 sum. To obtain the random numbers, one further multiplies x_n by the *tempering matrix*,

$$z_n = x_n g \tag{B.4}$$

and z_n is the n-th random number. g is built considering right R and left L shift matrices and a third matrix $D(y) = \text{diag}(y^1, ..., y^w)$, which is obtained from the w-bit number y, remembering that

$$R = \begin{pmatrix} 0 & & \\ \vdots & \mathbb{1}_{w-1} & \\ 0 & & \\ 0 & \dots & 0 \end{pmatrix}, \quad L = \begin{pmatrix} 0 & & \\ \vdots & \mathbb{1}_{w-1} & \\ 0 & & \\ 0 & \dots & 0 \end{pmatrix}, \tag{B.5}$$

g is thus defined as

$$g = (R^u D(d) \oplus \mathbb{1})(L^s D(b) \oplus \mathbb{1})(L^t D(c) \oplus \mathbb{1})(R^l \oplus \mathbb{1}). \tag{B.6}$$

where d, b, u, s, t and l are carefully chosen integers. All parameters for the generator can be seen in Table 11.

Parameter	$\#_{10}$	$\#_2$
w	32	
p	624	
q	227	
m	31	
a	2567483615	10011001000010001011000011011111
u	11	
d	4294967295	11111111111111111111111111111111
s	7	
b	2636928640	10011101001011000101011010000000
t	15	
c	4022730752	11101111110001100000000000000000
l	18	

Table 11 – Mersenne Twister parameters. In the second column, the numbers in base 10, in the third, in base 2, but only for those which are used in this form in the algorithm.

Nowadays there are many other options of generators and each one them might be suitable for each use. A comprehensive list of them, with tests for randomness for some algorithms can be found in ref. [46].

APPENDIX C – The Solid Angle subtended by a square

Due to the cubic geometry of the lattice, it is convenient to calculate (3.54) when $\mathcal{C}$ is a square. To this end one needs to know what is the solid angle subtended by a square from a arbitrary point $\mathbf{x}$ is space . Hence, one refers to the definition

$$\chi(\mathbf{x}) = \int_{\mathcal{S}_m(\mathcal{C})} d\theta d\phi \ \sin\theta \tag{C.1}$$

where (θ, ϕ) are the usual spherical coordinates. The following calculations follow the reasoning in ref. [52] For the sake of simplicity let us take the reference case where the projection of the point $\mathbf{x} = \mathbf{x}_c$ in the plane that contains $\mathcal{C}$ coincides with the center of a rectangle. If this rectangle has sides a and b, and the distance from the point to its projection is d, using the inverse spherical transformation $\theta = \arctan(z/\sqrt{x^2+y^2})$ and $\phi = \arctan(y/x)$, and taking into account the symmetry of the problem,

$$\chi(\mathbf{x}_c) = 4\left[\int_0^{\arctan\left(\frac{b}{a}\right)} d\phi \int_1^{\cos I_+(\theta;a)} d(\cos\theta) + \int_{\arctan\left(\frac{b}{a}\right)}^{\pi/2} d\phi \int_1^{\cos I_-(\theta;b)} d(\cos\theta)\right], \tag{C.2}$$

$$\text{where } \cos I_\pm(\theta; z) = \left(\frac{d}{\sqrt{d^2 + \frac{z^2}{4}(1+\tan^{\pm 2}\phi)}}\right). \tag{C.3}$$

The integral was separated in two terms that correspond respectively to the regions $\mathcal{A}_1$ and $\mathcal{A}_1$ in fig. 44.

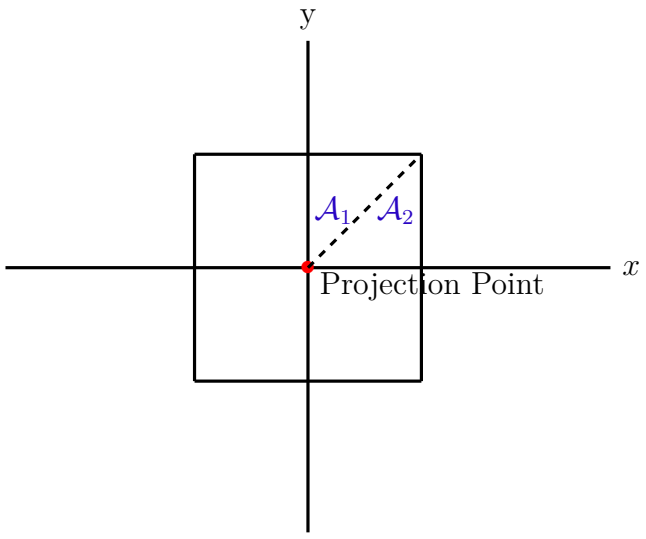

Figure 44 – Division of the solid angle subtended by a square when the projection point coincides with the center of the square.

After performing the cosine integral and substituting $\phi \mapsto \pi/2 - \phi$,

$$\chi(\mathbf{x}_c) = 4\left[\frac{\pi}{2} - \int_0^{\arctan\left(\frac{b}{a}\right)} J\left(\frac{a}{2d}\right) - \int_0^{\arctan\left(\frac{a}{b}\right)} J\left(\frac{b}{2d}\right)\right] \tag{C.4}$$

$$J(\phi; z) = \frac{\cos\phi}{\sqrt{\cos^2\phi + z^2}}. \tag{C.5}$$

Furthermore, after using the identity $\sin^2\phi + \cos^2\phi = 1$ to perform the integral, one has

$$\chi(\mathbf{x}_c) = 4\left[\frac{\pi}{2} - K\left(\frac{b}{a}; \frac{a}{2d}\right) - K\left(\frac{a}{b}; \frac{b}{2d}\right)\right] \tag{C.6}$$

$$K(y; z) = \arcsin\left[\frac{\sin(\arctan y)}{\sqrt{1+z^2}}\right]. \tag{C.7}$$

This equation can be manipulated into a more palatable form by using the identities [1].

$$\sin(\arctan y) = \sqrt{\frac{y^2}{1+y^2}} \tag{C.8}$$

$$\arcsin y + \arcsin z = \arcsin(y\sqrt{1-z^2} + z\sqrt{1-y^2}) \tag{C.9}$$

$$\arccos y = \frac{\pi}{2} - \arcsin y. \tag{C.10}$$

So that,

$$\chi(\mathbf{x}_c) = \chi(a, b, d) = \arccos\left[\sqrt{\frac{1+\alpha^2+\beta^2}{(1+\alpha^2)(1+\beta^2)}}\right], \tag{C.11}$$

$$\alpha = \frac{a}{2d}, \qquad \beta = \frac{b}{2d}. \tag{C.12}$$

Now (C.11), is used as a reference to calculate the solid angle for a arbitrary point. This is done by separating the points into four classes depending on where the point projects into the plane that contains the square as seen in fig. 45. Then one reduces the solid angle in each one of them as a sum of solid angles of centered points. The procedure will be explicitly carried out for one of the classes, the other three follow similarly.

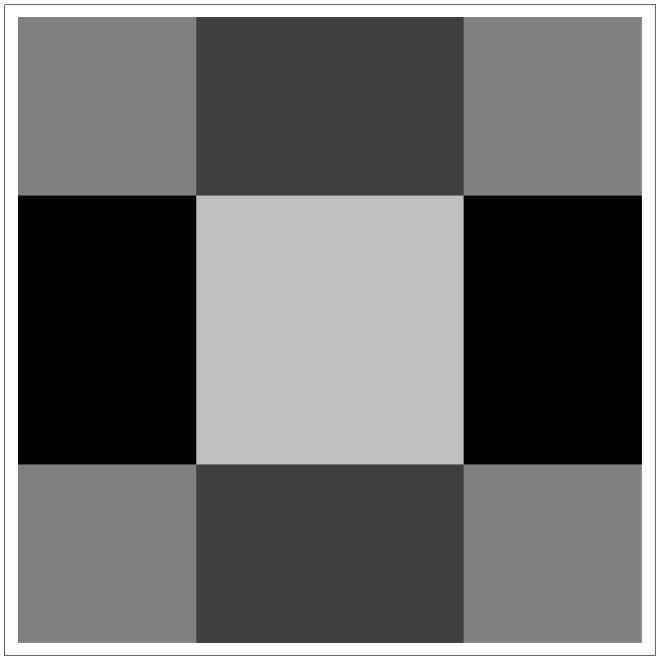

Figure 45 – Classes of regions depending on where the projection points lies (see main text). The square $\mathcal{C}$ itself is the one with the lightest shade of grey.

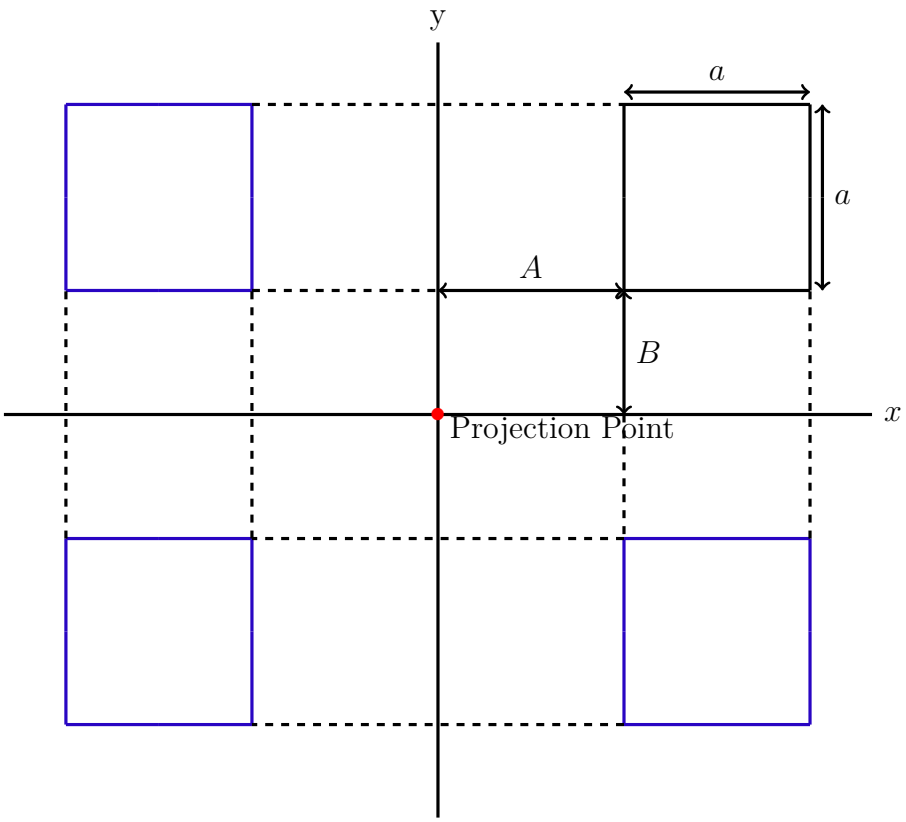

Figure 46 – Illustration of the method to obtain the solid angle subtended by the square where the reference point belongs to Class I. The original square, in black, is mirrored threefold and its images are used to write the solid angle as a sum of four terms. Adapted from ref. [52].

It will be considered that the square has side a and that the point projects at the origin of a xy-plane relative distances A and B from the closest square corner.

Class I

The projection point is "diagonally outside" the square. From fig. 46 above one realizes that it is possible to obtain (four times) the desired square by summing contributions from various centered rectangles, for which one has (C.11). They are obtained by reflecting the square with respect to both coordinate axis and $y = -x$ line.

The procedure is to take the large $2(A+a) \times 2(B+a)$ rectangle and (i) subtract the horizontal $2(a+A) \times 2B$ strip, then subtract the vertical $2A \times 2(a+B)$ strip. As we have over-subtracted the intersection of the two previous strips, which is $2A \times 2B$, it is summed back again. Mathematically,

$$\begin{aligned}\chi(\mathbf{x}_I) = \quad \chi_I(a,A,b,B,d) = \frac{1}{4}\,[&\chi(2(a+A),2(a+B),d) - \chi(2A,2(a+B),d) \\ &-\chi(2(a+A),2B,d) + \chi(2A,2B,d)]\,.\end{aligned} \tag{C.13}$$

Class II

Now the point lies "horizontally outside" the square. Now the big rectangle is $2(a-A) \times 2(a+B)$, the vertical $2A \times 2(a+B)$ strip is removed, and after it the horizontal $2(a-A) \times 2B$ one is added. As this one overlaps with the central $2A \times 2B$ plate it needs to be removed. Thence,

$$\begin{aligned}\chi(\mathbf{x}_{II}) = \quad \chi_{II}(a,A,b,B,d) = \frac{1}{4}\,[&\chi(2(a+A),2(b-B),d) - \chi(2A,2(b-B),d) \\ &+\chi(2(a+A),2B,d) - \chi(2A,2B,d)]\,.\end{aligned} \tag{C.14}$$

Class III

In this class, the point lies "vertically outside" the square. This case is analogous to Class II, one only needs to change $(a+A)$ to $(a-A)$ and $(a-B)$ to $(a+B)$. Consequently,

$$\begin{aligned}\chi(\mathbf{x}_{III}) = \quad \chi_{III}(a,A,b,B,d) = \frac{1}{4}\,[&\chi(2(a-A),2(b+B),d) - \chi(2(a-A),2B,d) \\ &+\chi(2A,2(b+B),d) - \chi(2A,2B,d)]\,.\end{aligned} \tag{C.15}$$

Class IV

Finally, for points inside the square, there are many overlaps. The big square is now $(a-A) \times (a-B)$, and because both the horizontal $2A \times 2(b-B)$, the vertical

$2(a-A)\times 2B$ and the central $2A\times 2B$ plate are overlaps, they must be added to each other in order to get the total area desired. Hence,

$$\chi(\mathbf{x}_{IV}) = \quad \chi_{IV}(a,A,b,B,d) = \frac{1}{4}\left[\chi(2(a-A),2(b-B),d) + \chi(2A,2(b-B),d) \right. \\ \left. +\chi(2(a-A),2B,d) + \chi(2A,2B,d)\right]. \tag{C.16}$$

With these results in mind, one is able to compute the solid angle from a arbitrary point of the lattice in space. In fig. 47 a 10×10 (arbitrary units) square is place parallel to the xz plane and the solid angle subtended by it is plotted for points in a plane parallel to the square at a distance of 1 from it.

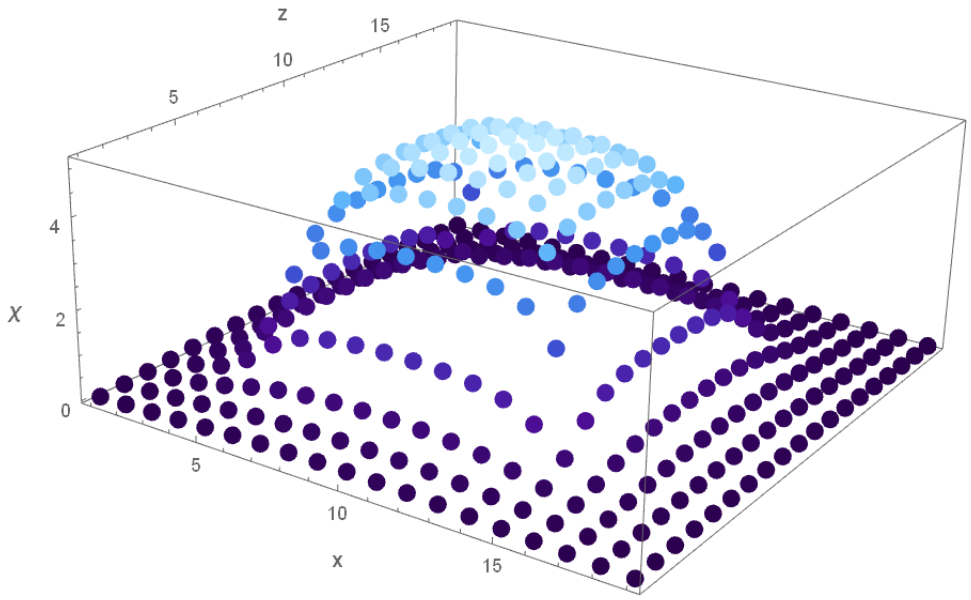

Figure 47 – Solid angle subtended by a 10×10 square from points in a plane parallel to the square at a distance of 1 from it

Another important plot that we are in position to show now is the spatial dependence of the gradient of the solid angle. As one can see in fig. 48, it can be seen that this vector field indeed swirls around the Wilson loop, thus giving a pictorial counterpart of property (3.52).

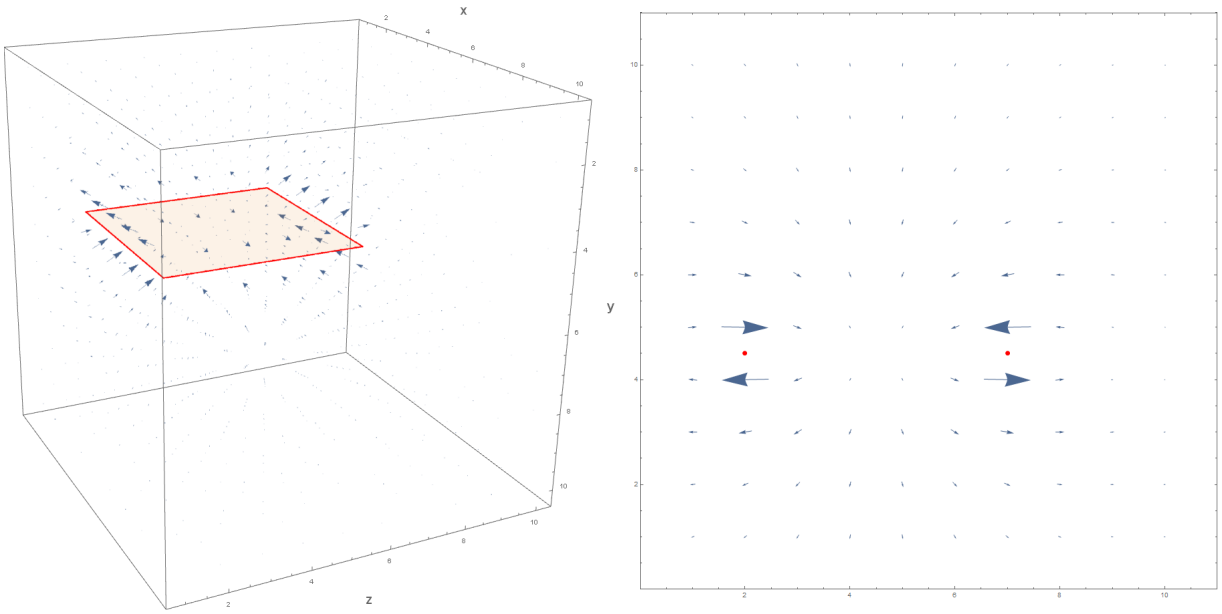

Figure 48 – The gradient of the solid angle subtended by a square. On the left-hand side the 3D vector field configuration. In the right-hand side, the gradient is plotted in a plane perpendicular to the loop $\mathcal{C}$

One final and important remark to be done is that: as equation (C.11) depends only on the distance of the observation point to the plane that contains the square, the singularity discussed in section 5.5 does not appear. Furthermore, as the arco-cosine funtion takes values in the interval $[0, \pi/2]$, $\chi \in [0, 2\pi]$, what is actually done is to take $\chi \mapsto 4\pi - \chi$ when the observation point is under the square.

Bibliography

[1] M. Abramowitz and I. A. Stegun. *Handbook of Mathematical Functions*. Dover Publications, 9th edition, 1972. Cited on page 112

[2] A. A. Abrikosov. The magnetic properties of superconducting alloys. *Journal of Physics and Chemistry of Solids*, 2:199–208, 1957. doi:10.1016/0022-3697(57)90083-5. Cited on page 22

[3] N.A. Alves, B.A. Berg, and S. Sanielevici. Spectral density study of the SU(3) deconfining phase transition. *Nuclear Physics B*, 376:218, 1992. doi:10.1016/0550-3213(92)90075-M. Cited on page 39

[4] J. Ambjørn, J. Giedt, and J. Greensite. Vortex structure versus monopole dominance in abelian projected gauge theory. *Journal of High Energy Physics*, 02:1–39, 2000. doi:10.1088/1126-6708/2000/02/033. Cited 2 times on pages 13 and 34.

[5] J. Ambjørn, P. Olesen, and C. Peterson. Stochastic confinement and dimensional reduction (I): four-dimensional SU(2) lattice gauge theory. *Nuclear Physics B*, 240:189–212, 533–542, 1984. doi:10.1016/0550-3213(84)90242-6. Cited on page 35

[6] N. W. Ashcroft and N.D. Mermin. *Solid State Physics*. •. New York : Holt, Rinehart and Winston, first edition, 1976. Cited on page 22

[7] M. Baker et al. The nonperturbative color field in the SU(3) flux tube. 2018. arXiv:1810.07133. Cited 4 times on pages 13, 21, 22, and 23.

[8] G. Bali. Casimir scaling of SU(3) static potentials. *Physical Review D*, 62, 2000. doi:10.1103/PhysRevD.62.114503. Cited 3 times on pages 13, 35, and 36.

[9] G. S. Bali. QCD forces and heavy quark bound states. *Physics Reports*, 343(177):1–136, 2001. doi:10.1016/S0370-1573(00)00079-X. Cited 2 times on pages 21 and 23.

[10] K. Binder. Critical Properties from Monte Carlo Coarse Graining and Renormalization. *Physical Review Letters*, 47(9):693–695, 1981. doi:10.1103/PhysRevLett.47.693. Cited on page 62

[11] K. Binder and D. W. Heermann. *Monte Carlo Simulation in Statistical Physics: An Introduction*. Graduate Texts in Physics. Springer, fifth edition, 2010. Cited 6 times on pages 25, 58, 61, 62, 65, and 66.

[12] G. Boyd et al. Thermodynamics of SU(3) Lattice Gauge Theory. *Nuclear Physics B*, 469:419–444, 1996. doi:10.1016/0550-3213(96)00170-8. Cited on page 39

[13] J. M. Cornwall. Quark confinement and vortices in massive gauge-invariant QCD. *Nuclear Physics B*, 157(3):392–412, 1979. doi:10.1016/0550-3213(79)90111-1. Cited 2 times on pages 21 and 24.

[14] J. M. Cornwall. Entropy in Quantum Chromodynamics. *Modern Physics Letters A*, 27(09), 2012. doi:10.1142/S021773231230011X. Cited on page 24

[15] M. Creutz. Monte Carlo study of quantized SU(2) gauge theory. *Physical Review D*, 21(8):2308, 1980. doi:10.1103/physrevd.21.2308. Cited on page 21

[16] M. Creutz. *Quarks, Gluons and Lattices*. Cambridge Monographs in Mathematical Physics. Cambridge University Press, 1983. Cited 2 times on pages 31 and 105.

[17] F. David. Quantum field theory ii, 2014. Lecture Notes for Perimeter Scholars International https://physique.cuso.ch/fileadmin/physique/document/2014_David_Quantum_1.pdf. Cited on page 100

[18] P. de Forcrand, M. D'Elia, and M. Pepe. 't hooft loop in SU(2) Yang-Mills theory. *Physical review letters*, 86(8):1438, 2001. doi:10.1103/PhysRevLett.86.1438. Cited on page 66

[19] P. de Forcrand and S. Kratochvila. Observing string breaking with Wilson loops. *Nuclear Physics B*, 671:103–132, 2003. doi:10.1016/j.nuclphysb.2003.08.014. Cited 2 times on pages 13 and 37.

[20] L. del Debbio, M. Faber, J. Greensite, and Š. Olejník. Casimir scaling versus abelian dominance in qcd string formation. *Physical Review D*, 53(10):5891, 1996. doi:10.1103/PhysRevD.53.5891. Cited 2 times on pages 21 and 36.

[21] L. del Debbio, M. Faber, J. Greensite, and Š. Olejník. Some cautionary remarks on abelian projection and abelian dominance. *Nuclear Physics B - Proceedings Supplements*, 53:141–147, 1996. doi:10.1016/S0920-5632(96)00608-1. Cited on page 36

[22] G. di Cecio, A. di Giacomo, G. Paffuti, and M. Trigiante. Condensation of vortices in the XY model in 3d: a disorder parameter. *Nuclear Physics B - Proceedings Supplements*, 53. Cited on page 49

[23] M. Douglas and S. Shenker. Dynamics of SU(N) Supersymmetric Gauge Theory. *Nuclear Physics B*, 447:271–296, 1995. doi:10.1016/0550-3213(95)00258-T. Cited 2 times on pages 21 and 37.

[24] S. Elitzur. Impossibility of spontaneously breaking local symmetries. *Physical Review D*, 12, 1975. doi:10.1103/PhysRevD.12.3978. Cited on page 27

[25] M. Engelhardt et al. Interaction of confining vortices in SU(2) lattice gauge theory. *Physical Letters B*, (431):141–146, 1998. doi:10.1016/S0370-2693(98)00583-8. Cited 2 times on pages 25 and 42.

[26] M. Engelhardt, K. Langfeld, H. Reinhardt, and O. Tennert. Deconfinement in SU(2) Yang-Mills theory as a center vortex percolation transition. *Physical Review D*, 61(5), 2000. doi:10.1103/PhysRevD.61.054504. Cited 3 times on pages 14, 39, and 41.

[27] M. Engelhardt, M. Quandt, and H. Reinhardt. Center vortex model for the infrared sector of SU(3) Yang–Mills theory—confinement and deconfinement. *Nuclear Physics B*, 685:227–248, 2004. doi:10.1016/j.nuclphysb.2004.02.036. Cited 7 times on pages 13, 14, 25, 38, 39, 40, and 43.

[28] M. Engelhardt and H. Reinhardt. Center projection vortices in continuum Yang–Mills theory. *Nuclear Physics B*, 567:249–292, 2000. doi:10.1016/S0550-3213(99)00727-0. Cited 2 times on pages 25 and 38.

[29] M. Engelhardt and H. Reinhardt. Center vortex model for the infrared sector of Yang-Mills theory - topological susceptibility. *Nuclear Physics B*, 585:614–633, 2000. doi:10.1016/s0550-3213(00)00350-3. Cited on page 38

[30] M. Engelhardt and H. Reinhardt. Center vortex model for the infrared sector of Yang–Mills theory — confinement and deconfinement. *Nuclear Physics B*, 585:591–613, 2000. doi:10.1016/S0550-3213(00)00445-4. Cited 2 times on pages 38 and 39.

[31] C. Gattringer. Coherent center domains in su (3) gluodynamics and their percolation at tc. *Physics Letters B*, 690(2):179–182, 2010. doi:10.1016/j.physletb.2010.05.013. Cited on page 32

[32] C. Gattringer and C. B. Lang. *Quantum Chromodynamics on the Lattice: An introductory presentation*. Lecture Notes in Physics 788. Springer, 2011. Cited 7 times on pages 13, 24, 25, 28, 30, 61, and 98.

[33] C. Gattringer and A. Schmidt. Center clusters in the yang-mills vacuum. *Journal of High Energy Physics*, 2011(1):51, 2011. doi:10.1007/JHEP01(2011)051. Cited on page 32

[34] A. P. Gottlob and Hasenbusch M. Critical Behaviour of the 3D XY-model: A Monte Carlo Study. *Physica A*, 201, 1993. doi:10.1016/0378-4371(93)90131-M. Cited 3 times on pages 47, 49, and 61.

[35] J. Greensite. Calculation of the Yang–Mills vacuum wave functional. *Nuclear Physics B*, 158:469–496, 1979. doi:10.1016/0550-3213(79)90178-0. Cited on page 35

[36] J. Greensite. The Confinement Problem in Lattice Gauge Theory. *Progress in Particle and Nuclear Physics*, 51:1–83, 2003. doi:10.1016/S0146-6410(03)90012-3. Cited 2 times on pages 21 and 28.

[37] J. Greensite. *Introduction to the Confinement Problem*. Lecture Notes in Physics 821. Springer, 2011. Cited 7 times on pages 13, 23, 24, 28, 30, 31, and 53.

[38] L.S. Grigorio, M.S. Guimarães, R. Rougemont, and C. Wotzasek. Dual approaches for defects condensation. *Physics Letters B*, 690(3):316–321, 2010. doi:10.1016/j.physletb.2010.05.044. Cited on page 46

[39] M. Göpfert and G. Mack. Proof of confinement of static quarks in 3-dimensional U(1) lattice gauge theory for all values of the coupling constant. *Communications in Mathematical Physics*, 82:545–606, 1982. doi:10.1007/BF01961240. Cited on page 23

[40] M. Hale, O. Schwindt, and T. Weidig. Simulated annealing for topological solitons. *Physical Review E*, 62(3):4333, 2000. doi:https://doi.org/10.1103/PhysRevE.62.4333. Cited 2 times on pages 14 and 59.

[41] B. Hall. *Lie Groups, Lie Algebras and Representations: An elementary introduction*. Graduate Texts In Mathematics 222. Springer, second edition, 2015. Cited on page 35

[42] A. Hanany, M. Strassler, and A. Zaffaroni. Confinement and strings in MQCD. *Nuclear Physics B*, 513:87–118, 1998. doi:10.1016/S0550-3213(97)00651-2. Cited on page 37

[43] A. Jaffe and E. Witten. Quantum Yang-Mills theory, 2016. Yang-Mills Mass Gap official problem description at Clay Mathematics Institute http://www.claymath.org/sites/default/files/yangmills.pdf. Cited on page 21

[44] H. Kleinert. *Gauge Fields in Condensed Matter*, volume II. World Scientific, 1989. Cited 6 times on pages 47, 48, 49, 51, 52, and 71.

[45] R. Kleiss. Monte Carlo: Techniques and Theory, 2019. Lecture Notes for the 4th Dutch-Brazil School in Theoretical Physics. 2019. http://www.ictp-saifr.org/wp-content/uploads/2019/02/newmc.pdf. Cited 5 times on pages 26, 57, 107, 108, and 109.

[46] R. T. Kneusel. *Random Numbers and Computers*. Springer International Publishing, 2018. Cited 3 times on pages 26, 108, and 110.

[47] K. Langfeld. Vortex structures in pure SU(3) lattice gauge theory. *Physical Review D*, (69), 2004. doi:10.1103/PhysRevD.69.014503. Cited 3 times on pages 13, 33, and 34.

[48] K. Langfeld, H. Reinhardt, and O. Tennert. Confinement and scaling of the vortex vacuum of SU(2) lattice gauge theory. *Physics Letters B*, 419:317–321, 1998. doi:10.1016/S0370-2693(97)01435-4. Cited on page 42

[49] D. H. Lehmer. Mathematical methods in large scale computing units. *Proceedings of the Second Symposium on Large-Scale Digital Computing Machinery*, pages 141–146, 1951. Harvard University Press. Cited on page 107

[50] M. Lüscher and P. Weisz. Quark confinement and the bosonic string. *Journal of High Energy Physics*, 2002(049):19, 2002. doi:10.1088/1126-6708/2002/07/049. Cited on page 21

[51] K. Symanzik M. Lüscher and P. Weisz. Anomalies of the free loop wave equation in the WKB approximation. *Nuclear Physics B*, 173:365–396, 1980. doi:10.1016/0550-3213(80)90009-7. Cited on page 22

[52] R.J. Mathar. Solid angle of a rectangular plate, 2019. Lecture Notes. Max-Planck Institute of Astronomy. http://www.mpia.de/~mathar/public/mathar20051002.pdf. Cited 4 times on pages 15, 26, 111, and 113.

[53] M. Matsumoto and T. Nishimura. Mersenne twister: a 623-dimensionally equidistributed uniform pseudo-random number generator. *ACM Transactions on Modeling and Computer Simulation (TOMACS)*, 8.1:3–30, 1998. doi:1049-3301/98/0100âĂŞ0003. Cited 3 times on pages 26, 108, and 109.

[54] N. Metropolis et al. Equation of State Calculations by Fast Computing Machines. *Journal of Chemical Physics*, 21(1087), 1953. doi:10.1063/1.1699114. Cited on page 58

[55] C. Michael and M. Teper. The glueball spectrum in SU(3). *Nuclear Physics B*, 314(2):347–362, 1989. doi:10.1016/0550-3213(89)90156-9. Cited on page 42

[56] Y. Nambu. Strings, monopoles, and gauge fields. *Physical Review D*, 4262, 1974. doi:10.1103/PhysRevD.10.4262. Cited on page 22

[57] P. Olesen. Confinement and random fluxes. *Nuclear Physics B*, 200:381–390, 1982. doi:10.1016/0550-3213(82)90094-3. Cited on page 35

[58] L. E. Oxman and H. Reinhardt. Effective theory of the D = 3 center vortex ensemble. *European Physical Journal C*, 78(177), 2018. doi:10.1140/epjc/s10052-018-5663-x. Cited 7 times on pages 11, 25, 45, 46, 49, 65, and 91.

[59] L. E. Oxman and G.C. Santos-Rosa. Detecting topological sectors in continuum Yang-Mills theory and the fate of BRST symmetry. *Physical Review D*, 92(125025), 2015. doi:10.1103/PhysRevD.92.125025. Cited on page 34

[60] M. E. Peskin and D. V. Schroeder. *An introduction to Quantum Field Theory*. •. Westview Press, 1995. Cited 2 times on pages 21 and 98.

[61] A. M. Polyakov. Quark confinement and topology of gauge theories. *Nuclear Physics B*, 120:429–458, 1977. doi:10.1016/0550-3213(77)90086-4. Cited on page 23

[62] M. Quandt, H. Reinhardt, and M. Engelhardt. Center vortex model for the infrared sector of SU(3) Yang-Mills theory: Vortex free energy. *Physical Review D*, 685:227–248, 2004. doi:10.1016/j.nuclphysb.2004.02.036. Cited 2 times on pages 38 and 66.

[63] H. Reinhardt. Effective Approaches to QCD. 2017. Lecture Notes to 53rd Karpacz Winter School of Theoretical Physics. arXiv:1804.03875. Cited 5 times on pages 13, 22, 24, 32, and 33.

[64] H .J. Rothe. *Lattice Gauge Theories: An Introduction*, volume 74 of *World Scientific Lecture Notes in Physics*. World Scientific, third edition, 2005. Cited on page 49

[65] D. V. Schroeder. *An Introduction to Thermal Physics*. Addison-Wesley Professional, first edition, 1999. Cited on page 64

[66] R.H. Swendsen and J.S. Wang. Nonuniversal critical dynamics in Monte Carlo simulations. *Physics Review Letters*, 58, 1987. doi:10.1103/PhysRevLett.58.86. Cited on page 62

[67] K. Symanzik. Continuum limit and improved action in lattice theories:(i). principles and $\varphi 4$ theory. *Nuclear Physics B*, 226(1):187–204, 1983. doi:10.1016/0550-3213(83)90468-6. Cited on page 100

[68] K. Symanzik. Continuum limit and improved action in lattice theories:(ii). O(N) non-linear sigma model in perturbation theory. *Nuclear Physics B*, 226(1):205–227, 1983. doi:10.1016/0550-3213(83)90469-8. Cited on page 100

[69] D. Tong. Lectures on Gauge Theory. Department of Applied Mathematics and Theoretical Physics. 2018. http://www.damtp.cam.ac.uk/user/tong/gaugetheory.html. Cited on page 28

[70] K. G. Wilson. Confinement of quarks. *Physical Review D*, 10, 1974. doi:10.1103/PhysRevD.10.2445. Cited 3 times on pages 21, 27, and 29.

[71] U. Wolff. Collective Monte Carlo Updating for Spin Systems. *Physics Review Letters*. Cited on page 62

[72] U. Wolff. Collective Monte Carlo updating in a high precision study of the xy model. *Nuclear Physics B*. Cited on page 62

[73] D. Wong. How does the Mersenne's Twister work?, 2016. https://www.cryptologie.net/article/331/how-does-the-mersennes-twister-work/. Cited on page 108

[74] C. N. Yang and R. L. Mills. Conservation of Isotopic Spin and Isotopic Gauge Invariance. *Physics Review*, 96:191, 1954. doi:10.1103/PhysRev.96.191. Cited on page 21